Bridging the gap between stability and performance of next-generation light-converting materials

Yunping Huang

A dissertation

submitted in partial fulfillment of the

requirements for the degree of

Doctor of Philosophy

University of Washington

2022

Reading Committee:

Christine Luscombe, Chair

Guozhong Cao

Ting Cao

Program Authorized to Offer Degree:

Materials Science and Engineering

University of Washington

Abstract

Bridging the gap between stability and performance of next-generation light-converting materials

Yunping Huang

Chair of the Supervisory Committee:
Christine Luscombe
Materials Science and Engineering

Optical engineering plays a crucial role in optoelectronic and communication devices, regarding efficiency, quality, and applications of the final devices. It consists of two components: design and manufacture of devices and development of materials. The former emphasizes the architecture of a device and the precision in its fabrication, while the latter focuses on tailoring materials' optoelectronic properties to enable a specific application. In this contribution, we focus on the optimization of light converting materials, organic phosphors and quantum dots, bridging the gap between performance and stability at low costs and thus accelerating their commercial adoptions. On the other hand, these two types of materials enable solution processing of devices, which simplifies device manufacture and meanwhile empowers the development of novel device architectures.

TABLE OF CONTENTS

LIST OF FIGURES

LIST OF TABLES

ACKNOWLEDGEMENTS

I would like to thank Prof. Christine Luscombe for being super supportive of all my research projects, allowing me to start the theobromine-derived organic dye project and providing advice and resources to expand my research into the inorganic nanomaterial domain. As organic chemistry by training, the experience researching inorganic nanomaterials was horizon-opening, Moreover, this hybrid research experiences endowed me with an interdisciplinary background and set up the foundation for my future interdisciplinary research projects – hybridizing inorganic and organic chemistry to develop novel materials possessing the advantages of both inorganic and organic materials.

I also would like to thank UW MEMC and CEI for their collaborative research environment, which makes my interdisciplinary projects possible. I have had a wonderful time collaborating with Prof. David Ginger, Prof. Daniel Gamelin, Prof. Brandi Cossairt, Prof. Kai-Mei Fu and Prof. Ting Cao on various projects on inorganic nanomaterials and such collaborations have led to fruitful outcomes. Of course big thanks to my fellow PhD students – we all know they are the ones who are doing the experiments🤣 – Ted Cohen in the lead halide perovskite nanocrystal projects, Yangwei Shi in the perovskite solar cell project, Demi Liu in the organic laser project, Christian Pederson in the NV center project, Jimin Qian for Raman simulation. I thank my fellow lab mates for the stimulating discussions on different projects, and extra credits to Parker Sommerville for helping with DFT simulation of dye molecules and holding a plastic sword on my neck to make me write the former sentence. Last but not least, I would like to thank Prof. Dave Beck for setting up the DIRECT program where I learn to use python, and his python instructions along with Prof. Ting Cao. Coding is another stepping-out-of-comfort-zone adventure

of mine, in addition to going into researching inorganic nanomaterials. Afterward in my mind formed my opinion regarding the whole “stepping out of your comfort zone” thing – it is like a swimming pool, and there are places where you can tip-toe and there are places where you drown. And I refer the former to inorganic nanomaterials research and the latter to coding. At the end of the first quarter on the DIRECT program, I was coding for a team project, of course, strenuously – strenuously is the perfect word here, highlighting the effort without mentioning the outcome. On the other hand, it was March 2020, the beginning of the COVID pandemic. And one day Christine sent me a note asking if I was well after she saw a 😭 on my slack status. I replied, “Oh it is just me coding for my DIRECT project 😭😭😭”. Dave is very likely reading this – yep, the GSR🤣 – and I would say that was likely a Feng-Shui problem considering the classroom was right next to the RTT lab where I made solar cells with zero efficiencies. That area is bad luck for me. Something is wrong with the magnetic field there. 🤷

I would also like to thank to help from UW CoMotion and UW CEI Testbed for their assistance in technology transfer, especially to Dr. Forest Bohrer and Dr. Mike Pomfret. I often sent them emails, most of which can be categorized as I-need-help emails. Nevertheless, I still think I am an awesome vintage college boy, becoming more and more articulate in presenting my idea to people of different scientific backgrounds through this technology transfer practice, and also winning awards and business competitions and securing technology transfer grants. I do think these activities through these 3 years did give a decent amount of extra workload to Christine, helping me refine the proposals. Sometimes she joked about me biting too much than I could chew.🤣

Despite finishing my PhD, I feel bad about being away from my parents for such a long time – since I moved here in 2017, I was only able to come back to see them once in 2019. It was planned as a one-month visit, but I ended up being stranded in China for two months due to the lengthy bureaucratic visa application process. They knew it is a five-year PhD program, and they only give me a one-year visa, which is also true for most of the PhD students in the STEM fields, for which we need to spend 2 months worrying about whether the visa will be approved instead of working when we go home – Oh I forget to mention they may reject your visa for reentering. What the hell is even that? I clearly remember the way my mom hugged me when she picked me up at the airport after being two years away from home in 2019 – she ran to me and gave me tight hug for nearly ten seconds. Such hugs are very rare in the Chinese culture, where people are generally refrained from showing affection. That hug vividly felt like I had been sent back home from the frontline after two years. My dad was just standing aside and said nothing. I know they must have been heart-broken while I am in the US in the past 4 years.

Chapter 1. INTRODUCTION

1.1 LIGHT AROUND US

Humans are surrounded by light and interact with it every day. Light does not only promote human vision, but also plays critical roles in our physical and mental health. For example, ultraviolet B (UVB) rays interact with skin and stimulate vitamin D3 secretion, while on the other hand, excessive exposure to ultraviolet lights increases the risk of skin cancer.[1] Light is also mood-altering: a workspace with adequate bright lighting gives rise to working efficiency, while a home space with dimmed lighting is associated with depression.[2]

In addition to natural sunlight, in modern times we are also subjected to different types of artificial lights, such as incandescent lights, halogen lights, fluorescent lights and LED lights. They have substantial impacts on us, which are varied from that of natural sunlight because of their difference in their light spectrum as shown in Figure 1.1. Though they are categorized as "white light," they have distinctly different spectrum profiles. Spectrum deviation from one of the sunlight leads to lowered color quality, which is often measured by color rendering index (CRI).[3] The usage of fluorescent lights, which have the lowest color rendering index (CRI) of all the light sources listed in Figure 1.1, results in significant color distortion of the lighted subject, which is detrimental for demonstration purposes.[4] In Figure 1.1e, one can note there is an intense peak of blue light in the cool white LED spectrum. This intense blue light is accountable for the negative health impacts of LEDs, such as alteration of circadian rhythm, accelerated aging and retina damage.[5] Artificial lighting isn't necessarily bad: lights with different spectral features are now being tested for the treatment of depression.[6] Therefore, optical engineering is a topic of attention and necessity. In

this work, I will be talking about different techniques that we use to manipulate the spectrum of light.

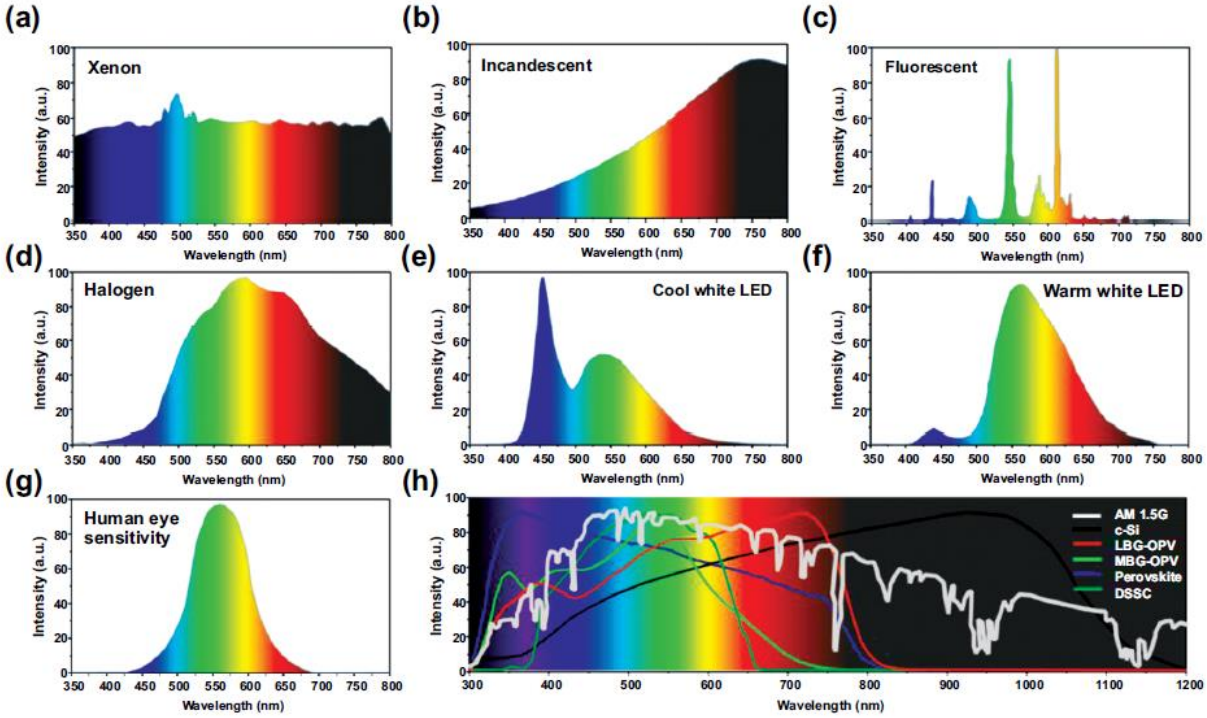

Figure 1.1. The difference of spectra from different light sources and human eye sensitivity to different wavelengths.

1.2 LIGHT CONVERTERS AND PERFORMANCE METRICS

Lighting converters are commonly applied to modify the spectral distribution of light sources. Figure 1.2 shows the most adopted architecture commercial white LEDs: a blue light source with a light converter on top.[7] The converter converts a portion of blue light that passes through to green or yellow or red light depending on the requirements of the application, and the nature of the material doing the converting. As for a commercial white LED, a fraction of blue light is converted to yellow light, which together forms white light with the unconverted blue light.

Another example is agricultural lighting that stimulates plant growth, where a fraction of blue light is converted to red light to optimize light conditions for photosynthesis.[8]

There are three types of lighting converters highlighted by industry and academia – inorganic phosphors,[9] nanocrystals (NCs)[10] and organic phosphors.[11] While inorganic phosphors have been used in the commercial market for a long time, NCs and organic phosphors are currently undergoing the transition from lab research to industrial applications. Despite their different stages in the R&D roadmap, each of these technologies is yet to realize their full potential and technical improvements are yet to be made. There are many parameters to be considered when evaluating the performance of light converters in LED application: photoluminescence quantum yield (PLQY), film transparency, emission spectrum coverage, and stability.

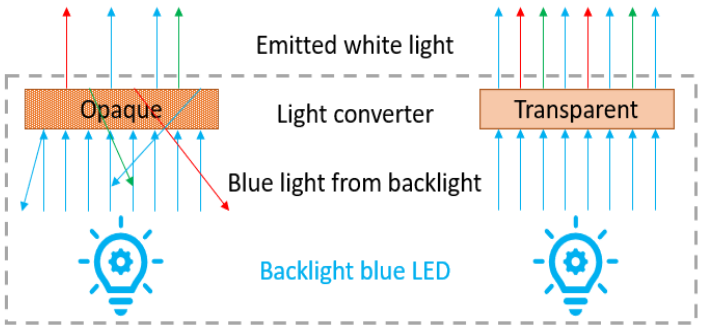

Figure 1.2. The device architecture of a phosphor-converted LED. The effects of optical transparency of the thin film are illustrated.

1.2.1 *Photoluminescence quantum yield*

PLQY is a metric to measure how efficient the material is in converting light into different wavelengths, and defined as below:

$$PLQY = \frac{Number\ of\ photons\ reemitted\ from\ the\ material}{Number\ of\ photons\ absorbed\ by\ the\ material} \quad (1.1)$$

A high PLQY is beneficial to the high energy efficiency of a LED. There are different factors that determine the value of PLQY, and they are dependent on the types of materials. We will discuss these factors in detail in Chapters 2, 3, 4 and 5.

1.2.2 *Film transparency*

Film transparency also plays a key role in determining the efficiency of a LED device. Fig. 1.2 compares the difference of light path in two LEDs, one with a transparent light converter and the other with an opaque light converter. Light is less likely to go through the opaque converter film, being backscattered and resulting in a decreased efficiency, and thus lower light output. [12]

1.2.3 *Emission spectra*

Emission spectra of lighting converters ultimately governs the color quality of LED lights. To obtain a high CRI, it is better to cover as much as possible in the visible spectrum from 380 – 780 nm. On the other hand, considering the sensitivity of human eyes to different wavelengths (Fig 1.1g), light outside this 400 – 700 nm window are much less efficient for illumination purpose and thus unnecessary. For general purposes such as residential lighting, a CRI of 80 is currently considered sufficient; CRI higher than 90 would be crucial to minimize the color distortion of artificial light sources, which is especially important for showcase and demonstration purposes. There are two major pathways for designing light converters based on their emission profiles: 1) developing materials with wide emission spectra so that one can utilize as few types of materials as possible to cover the full visible spectrum, such as YAG:Ce;[13] 2) narrow emission materials that allow precise control of emission spectra, such as nanocrystals, to limit wasteful light emission (*ie.* light outside of the 400-700 nm window).[14]

1.2.4 *Stability*

The relatively long lifetimes of LEDs (15-20 years) set a high stability requirement for light converters.[15] Owing to this long timeframe, accelerated stability measurements are usually performed. Materials are tested under elevated temperature, and occasionally with high humidity, and the PLQYs of the materials are monitored over time. On the other hand, considering the fact that LED generates a considerable amount of heat during operation and thermal quenching commonly exists in fluorescent materials,[16] it makes a good candidate when its PLQY remains unchanged, or mildly reduced, at high temperatures.

1.3 TYPES OF LIGHT CONVERTERS

1.3.1 *Inorganic phosphors*

Over the past decades, cerium doped yttrium aluminum garnet (YAG:Ce) are widely used in commercial LED products as light converters, due to its high PLQY and broad emission.[13] The broad emission enables a pure blue LED to be converted into a white LED; the spectra for this are shown in Figure 1.1 e & f. A problem with this system is that there is insufficient red light in the spectra of these white LEDs, significantly reducing the CRI values. Therefore, both academia and industry are currently searching for red phosphors with high PLQYs and stability, which are to be mixed with YAG:Ce and enhance the red light emission and thus the CRI of the resulting LEDs. Recent efforts have developed different red inorganic phosphors, however with PLQYs ranging from 70% to 80%.[17]

As mentioned earlier, lighting scattering in the light converting later is a major component for reduced efficiency of LEDs, and occurs independently of the PLQY of the component

materials. Considering the size of inorganic phosphors, approximately 1 – 10 μm, light is subject to substantial scattering when it passes through the light converters, reducing the light intensity outside the LED package. In manufacturing, light converting phosphors are usually blended with encapsulants and subsequentially applied on top of the blue LED chip, as shown in Figure 1.3. The micron-sized particles form dispersion in the encapsulant and because of this inhomogeneous system, around 20 wt% of inorganic phosphor is required for the optimal LED spectrum. This high usage of inorganic phosphor directly adds cost to manufacturers, increases the rate of scattering in the light converting layer, and increases the consumption of limited rare earth resources. Therefore, researchers are looking for alternatives to these micron-size inorganic phosphors, so as to simultaneously increase the energy efficiency and lower the manufacturing cost of LEDs.

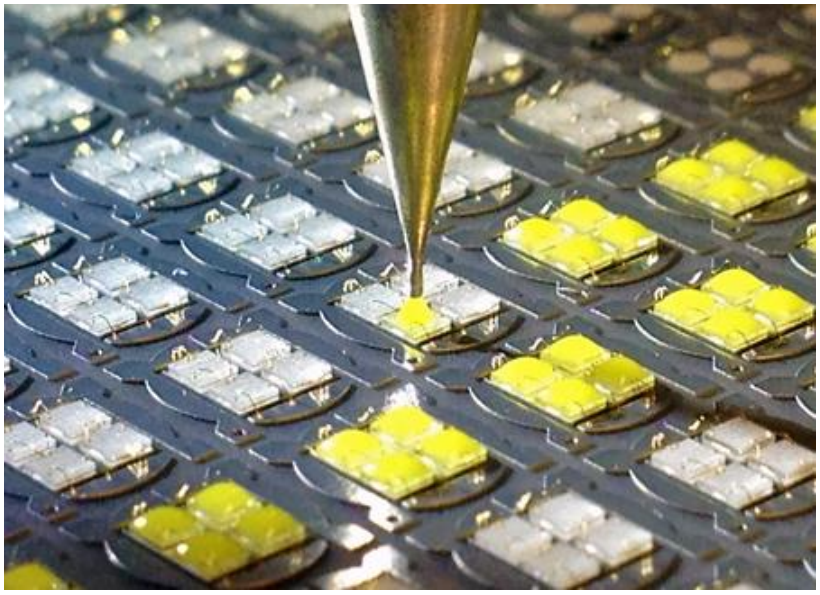

Figure 1.3. How phosphor-converted LEDs are manufactured: phosphor dispersed encapsulant is added directly on top of a blue LED.

1.3.2 *Nanocrystals*

Nanocrystals (NCs) are one of the solutions to the problem mentioned above. NCs are inorganic phosphors that are typically synthesized with particle sizes less than 10 – 20 nm. This small diameter leads to optical and electronic properties that differ from bulk or even micron-size inorganic phosphors owing to quantum confinement effects.[18] Because their sizes are significantly smaller than the wavelength of visible lights (380 - 780 nm), these particles result in no scattering in the optical system if they are evenly dispersed in the encapsulant. In lighting converting applications, NCs based on cadmium chalcogenide,[19] lead halide perovskite[20] and $CuIn(S,Se)_2$[21] have received the most attention because of their high PLQYs and their spectrum tunability. In addition, researchers are actively looking to further increase the stability of NCs using various methodologies, such as growing silica shells around the NCs to prevent degradation facilitated by oxygen and moisture.[22] However, growing a silica shell is not applicable to lead halide perovskites because this procedure requires the use of protic solvents, which are detrimental to maintaining the crystal structure and thus optoelectrical properties of perovskite; alternative solutions are needed to make use of these high PLQY materials.[23] Thus methods for improving the stability of lead halide perovskites is a highly valuable research topic at the present.

There are concerns about NCs regarding environmental toxicity and sustainability, because of the elements used in these technologies.[24] For example, cadmium and lead used respectively in cadmium chalcogenide and lead halide perovskite are heavy metals, representing a great concern to human health. Although $CuIn(S,Se)_2$ is free from toxic elements, indium is a scarce element, and subjective to limited supply in long terms.[25] Department of Energy (DOE) is now keenly seeking alternative light converting technologies that are free from toxic or scarce elements, while

maintaining the high optical performances – high PLQY, reduced scattering and ready spectrum engineering. [26]

1.3.3 *Organic phosphors*

Organic phosphors are primarily made of carbon and hydrogen, which are renewable resources and render this technology more environmentally sustainable compared to the inorganic counterparts.[27] Organic phosphors benefit from the unique bonding property of carbon, which can form stable covalent bonds with itself, as well as many other elements. That fact substantially increases the structural variety of organic phosphors and thus greatly increases the tunability of their optoelectronic properties, including emission spectra which are crucial in light converter application. Moreover, organic compounds are made from earth-abundant elements, and thus can be low-cost and more environmentally friendly, in sharp contrast to inorganic phosphors that rely on rare-earth elements. In LED manufacturing, organic phosphors can be easily dissolved in an LED encapsulant and form a highly transparent film, reducing the scattering loss of the devices. This can be explained by the structural compatibility between encapsulants and organic phosphors, both of which are organic-based. However, the stability problem of organic phosphors remains challenging in R&D developments and is necessary to address before further implementation as light converters for LEDs, where they are exposed to elevated temperatures and intense UV or blue light radiation.

1.3.4 *Summary*

In summary, even though micron-size inorganic phosphors are now widely applied in commercialized LED lightings and result in significant energy savings compared to incandescent and compact fluorescent lamps, they don’t provide optimal energy efficiency because of light

scattering. In addition, their reliance on rare-earth elements and the relatively large loadings in LED lighting raise concerns about the environmental sustainability of the industry. To address these problems, both academia and industry are putting efforts into developing high-performance NCs and organic phosphors to be applied as light converters for LEDs. In the paper, we discuss our efforts in developing NCs and organic phosphors with high PLQYs. Meanwhile, the stability and the environmental sustainability of the materials are also examined for their future application in commercial LED applications.

Chapter 2. ORGANIC PHOSPHORS: LOW-COST SYNTHESES TO HIGH PERFORMANCE

(This chapter is adapted from a paper published by Yunping Huang during this Ph.D program)[28]

2.1 INTRODUCTION

Aggregation caused quenching (ACQ) of chromophores commonly exists in organic semiconductors, dissipating excited state energy into heat instead of light emission.[29] This is detrimental for light converters in LEDs. While there are several reasons why ACQ can take place, in the case of organic luminophores with extended π conjugation, such as pyrene[29] and perylene diimide,[30] the molecules can interact with each other via π orbital overlap and form non-fluorescent excimers.

To date, numerous efforts have been invested into suppressing ACQ in organic luminophores. Huang *et al.* suppressed ACQ by attaching bulky oligo-alkylfluorene moieties onto luminophores (Figure. 2.1).[31,32] Once installed, the fluorene modifiers were able to act as spacers, preventing luminophore aggregation and thus improving the solid-state PLQYs. Moreover, because the oligo-alkylfluorenes are conjugated, charge mobilities were maintained after modification, in sharp contrast to insulating spacers. Tang *et al.* discovered that ACQ can be suppressed by attaching tetraphenylethene (TPE) onto luminophores triggering the mechanism of aggregation-induced emission (AIE).[29] Impressive results have been obtained by applying these types of materials to OLED and OL devices. However, these methods bring up environmental concerns: they heavily rely on Suzuki coupling, which uses air-sensitive and explosive organolithium compounds to prepare boronic ester precursors.[33] Should these materials be prepared at a commercial scale, a method avoiding organolithium would substantially diminish

workplace safety risks. Moreover, organolithium decreases the functional group tolerance in the synthesis, as it is strongly nucleophilic.

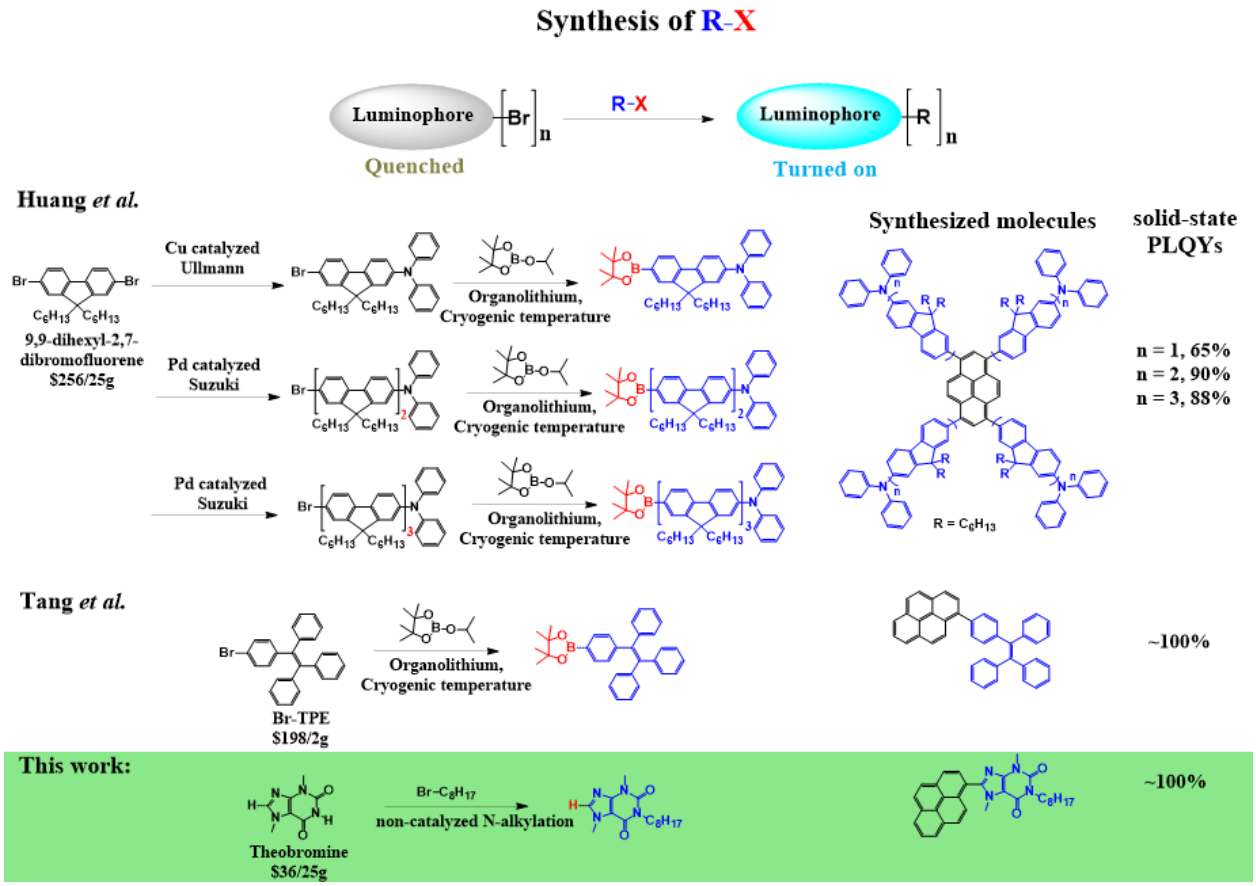

Figure 2.1. Chemical methods to improve the solid-state PLQYs of OLED emitters and PLQY values of target molecules. Cost of starting materials of each route: 1) 9,9-dihexyl-2,7-dibromofluorene: $267/25g; 2) bromo-TPE: $198/2g; 3) theobromine: $36/25g, on the Sigma Aldrich website.

Direct arylation offers a green and atom-efficient method to form C-C bonds between aromatic building blocks.[34,35] This direct formation of C-C bond allows us to bypass the extra step of precursor synthesis, where organolithiums are usually involved. Therefore, the risks of fire and explosion are reduced, while cost and productivity are optimized. Moreover, direct arylation is compatible with large-scale production. Major pharmaceutical companies, such as Merck[36] and Pfizer,[37] are applying it into commercial production of medicines; flow chemistry has been

successfully implemented and further enhances productivity.[38] Additionally, substrate compatibility is improved because of the absence of highly reactive intermediates. However, because the C-H bond on benzene has poor reactivity under the concerted metalation-deprotonation (CMD) mechanism,[39] it is not feasible to utilize direct arylation to attach oligofluorenes or TPE onto luminophores to minimize ACQ. A new moiety needs to be identified to pair with direct arylation to develop a green method to suppress ACQ.

In this chapter, alkylated theobromine is introduced onto luminophores via direct arylation to suppress ACQ. The mild reaction conditions allow for wide functional group tolerance. In this strategy, theobromine has the following advantages: 1) it is a natural product originally from cacao plants that is now produced in an industrial scale and thus readily available and inexpensive (see Figure 2.1 for price comparison for starting materials on each route); 2) the imidazole C-H bond is highly reactive for direct arylation;[39] 3) the N-methyl group on imidazole will repulse the luminophore and induce a large dihedral angle, creating steric hindrances preventing the luminophores from interacting with each other; 4) the lactam group is applied widely in the design of organic semiconductors with high electronic performance and one can easily tune the processability of the final product by introducing different solubilizing chains onto it.[40,41] Pyrene was chosen as the luminophore to test the effectiveness of this method. Pyrene is highly fluorescent in solution but completely quenched in the solid state,[28] making it a good candidate to examine our approach. Three theobromine-pyrene derivatives, with differing theobromine:pyrene ratios, were successfully synthesized and characterized.

2.2 MATERIAL PREPARATION

Theobromine, 1-bromooctane, 1-bromopyrene, 1,6-dibromopyrene, 1,3,6,8-tetrabromopyrene and tris(2-methoxyphenyl)phosphine were purchase from TCI.

Bis(dibenzylideneacetone)palladium(0) and pivalic acid were purchased from Sigma Aldrich. Solvents used were purified *via* a PureSolv solvent purification system from Inert Inc. K_2CO_3 and Cs_2CO_3 were ground into a powder and dried at 120 ^oC overnight before reactions. Reactions were run under N_2 atmosphere using standard Schlenk techniques and detailed synthesis procedures are described below.

3,7-dimethyl-1-octyl-3,7-dihydro-1H-purine-2,6-dione (Theo8). Into a 500 mL round bottom flask, theobromine (18.0 g, 100 mmol), 1-bromooctane (23.2 g, 120 mmol), dried K_2CO_3 (20.7 g, 150 mmol) and 200 mL DMF was added. The system was degassed and then heated to 120 ^oC overnight. When finished, the reaction was cooled to room temperature. ethyl acetate was used to extract the product and brine was used to remove residue DMF. The organic layer was subsequently washed with brine to remove the DMF in the organic phase. The organic layer was then dried over Mg_2SO_4 and concentrated under reduced pressure. The crude product was further purified with column chromatography using dichloromethane/methanol in a 10:1 ratio as an eluent. The collected fraction was then recrystallized from hexane. 25.7 g of collected white solid was collected, with 96% yield. ^{1}H NMR (500 MHz, $CDCl_3$) δ 7.51 (s, 1H), 4.02 – 3.97 (m, 5H), 3.57 (s, 3H), 1.70 – 1.58 (m, 2H), 1.47 – 1.20 (m, 10H), 0.92 – 0.82 (m, 3H). ^{13}C NMR (126 MHz, $CDCl_3$) δ 155.17, 151.41, 148.73, 141.61, 107.59, 41.39, 33.48, 31.84, 29.56, 29.34, 29.24, 28.12, 27.05, 22.64, 14.07.

3,7-dimethyl-1-octyl-8-(pyren-1-yl)-3,7-dihydro-1H-purine-2,6-dione (PT1). Theo8 (552 mg, 2 mmol) and 1-bromopyrene (562 mg, 2 mmol), pivalic acid (40 mg, 0.4 mmol) and dried Cs_2CO_3 (1.30 g, 4 mmol) were added into a 25 mL round bottom flask. 10 ml toluene was then adding into the system followed by degassing with N_2 flow for 10 min. Tris(2-methoxyphenyl)phosphine (56 mg , 0.097 mmol) and bis(dibenzylideneacetone)palladium(0) (40

mg, 0.044 mmol) were added to the solution under N_2 flow, and the solution turned purple. The flask was then sealed with a rubber stopper and heated to 100 ^oC. After reacting for 1 day, the system was cooled and filtered. The organic phase was then concentrated under reduced pressure. The crude product was further purified with column chromatography using chloroform/methanol in a 400:5 ratio as an eluent (chloroform/methanol = 400/5). 715 mg of white solid was obtained in a 75% yield. ^1H NMR (500 MHz, $CDCl_3$) δ 8.29 (d, *J* = 2.5 Hz, 1H), 8.28 (d, *J* = 2.5 Hz, 1H), 8.26 (d, *J* = 10 Hz, 1H), 8.20 (d, *J* = 9.0 Hz, 1H), 8.15 (q, 2H), 8.08 (t, 2H), 7.92 (d, *J* = 9.2 Hz, 1H), 4.19 – 4.02 (m, 2H), 3.83 (s, 3H), 3.70 (s, 3H), 1.83 – 1.69 (m, 2H), 1.50 – 1.23 (m, 10H), 0.98 – 0.83 (m, 3H). ^{13}C NMR (126 MHz, $CDCl_3$) δ 155.58, 152.03, 151.65, 150.16, 148.59, 132.90, 131.26, 130.74, 130.40, 129.40, 129.14, 127.80, 127.19, 126.61, 126.30, 126.08, 124.84, 124.60, 124.42, 123.90, 122.40, 108.58, 41.67, 33.49, 31.88, 29.88, 29.29, 28.27, 27.14, 22.67, 14.08.

8,8'-(pyrene-1,6-diyl)bis(3,7-dimethyl-1-octyl-3,7-dihydro-1H-purine-2,6-dione) (PT2). Theo8 (1,932 mg, 7 mmol) and 1,6-dibromopyrene (1,080 mg, 3 mmol), pivalic acid (80 mg, 0.8 mmol) and dried Cs_2CO_3 (3 g, 9 mmol) were added into a 50 mL round bottom flask. 25 mL toluene was then adding into the flask, followed by degassing with N_2 flow for 10 min. Tris(2-methoxyphenyl)phosphine (122 mg, 0.194 mmol) and bis(dibenzylideneacetone)palladium(0) (80 mg, 0.088 mmol) were added to the solution under N_2 flow, and the solution turned purple. The flask was then sealed with a rubber stopper and heated to 100 ^oC. After reacting for 1 day, the system was cooled and filtered. The organic phase was then concentrated under reduced pressure. The crude product was further purified with column chromatography using chloroform/methanol in a ratio of 400/5 as an eluent. 1,472 mg pale yellow solid was obtained in a 65% yield. ^1H NMR (500 MHz, $CDCl_3$) δ 8.38 (d, *J* = 7.9 Hz, 2H), 8.23 (d, *J* = 9.2 Hz, 2H), 8.16 (d, *J* = 7.9 Hz, 2H),

8.09 (d, *J* = 9.2 Hz, 2H), 4.16 – 4.05 (m, 4H), 3.88 (s, 6H), 3.71 (s, 6H), 1.80 – 1.69 (m, 2H), 1.51 – 1.22 (m, 20H), 0.94 – 0.85 (m, 6H). ^{13}C NMR (126 MHz, $CDCl_3$) δ 155.54, 151.55, 151.38, 148.51, 132.31, 130.48, 129.11, 128.51, 125.64, 124.54, 123.65, 108.66, 41.68, 33.59, 31.86, 29.89, 29.39, 29.27, 28.23, 27.11, 22.66, 14.11.

8,8',8'',8'''-(pyrene-1,3,6,8-tetrayl)tetrakis(3,7-dimethyl-1-octyl-3,7-dihydro-1H-purine-2,6-dione) (PT4). **Theo8** (1,932 mg, 76 mmol) and 1,3,6,8-tetrabromopyrene (517 mg, 1 mmol), pivalic acid (80 mg, 0.8 mmol) and dried Cs_2CO_3 (3 g, 9 mmol) were added into a 50 mL round bottom flask. 15 mL toluene was then adding into the system followed by degassing with N_2 flow for 10 min. Tris(2-methoxyphenyl)phosphine (122 mg , 0.194 mmol) and bis(dibenzylideneacetone)palladium(0) (80 mg, 0.088 mmol) were added to the solution under N_2 flow, and the solution turned purple. The flask was then sealed with a rubber stopper and heated to 100 ºC. After reacting for 1 day, the system was cooled and filtered. The organic phase was then concentrated under reduced pressure. The crude product was purified with column chromatography using chloroform/methanol in a ratio of 40:1 as an eluent. 585 mg green-yellow solid was obtained in a 43% yield. ^{1}H NMR (500 MHz, $CDCl_3$) δ 8.36 (s, 2H), 8.27 (s, 4H), 4.08 (t, 8H), 3.91 (s, 12H), 3.68 (s, 12H), 1.73 (m, 8H), 1.47 – 1.23 (m, 40H), 0.92 – 0.87 (m, 12H). ^{13}C NMR (126 MHz, $CDCl_3$) δ 155.44, 151.42, 149.53, 148.51, 131.43, 131.14, 127.32, 124.79, 124.64, 109.01, 41.76, 33.86, 31.84, 29.89, 29.37, 29.26, 28.18, 27.08, 22.66, 14.10.

2.3 RESULTS AND DISCUSSION

The synthetic route to PT1, PT2 and PT4 is straightforward, beginning with the N-alkylation of theobromine, as shown in Scheme 2.1. The relatively long octyl chains were introduced to increase the hydrophobicity of the final products, improving solubility in common

solvents and enabling solution processing. The key intermediate Theo8 was obtained in nearly quantitative yield. Subsequently, Theo8 and pyrene were cross-coupled by direct arylation, forming PT1, PT2, and PT4 with increasing equivalents of Theo8. Notably, these materials are made in just two steps from commercially available starting materials. In contrast, it would take two extra steps to synthesize these materials via Suzuki coupling: converting brominated pyrenes to pyrene boronic esters and brominating Theo8. Moreover, as for products with high functionalities such as PT4, their overall yields would be significantly reduced with each step added to the overall route due to relatively higher incomplete conversion of each synthetic step. As hypothesized, these three compounds show high PLQYs in both solid state and solution, and their absorption and emission spectra are shown in Figure 2.2. Notably, PT1 shows the highest PLQYs of all, approaching 100% both in solution and as thin films. Increasing the ratio of Theo8 leads to a decrease of PLQYs as thin films, as shown in Table 2.1, consistent with the photoluminescence lifetime measurements in Figure. 2.3. Increasing the amount of Theo8 in the molecules increases the size of their conjugated systems. This could lead to the increase in intermolecular π overlap in solid state, facilitating ACQ and thus lowering solid-state PLQYs.

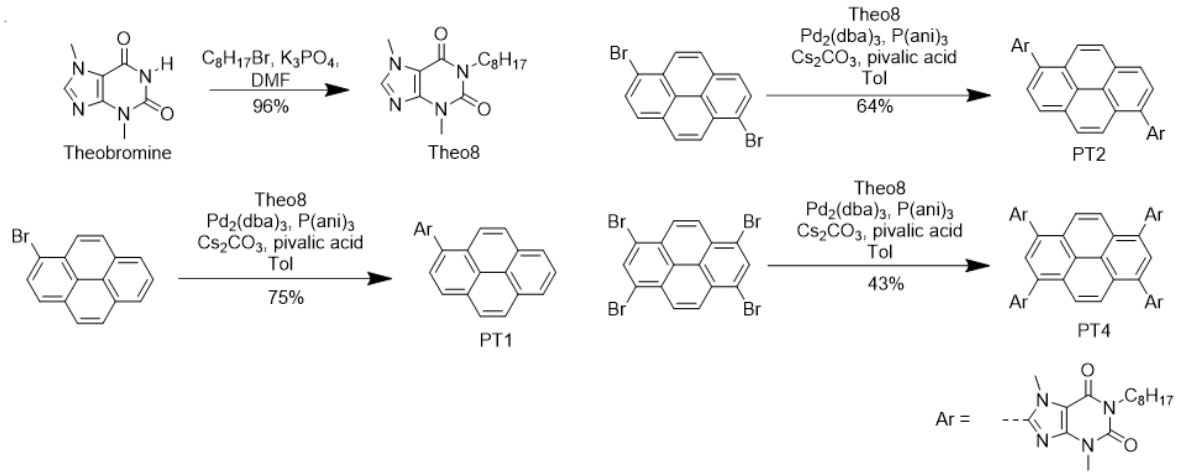

Scheme 2.1. The syntheses of PT1, PT2 and PT4.

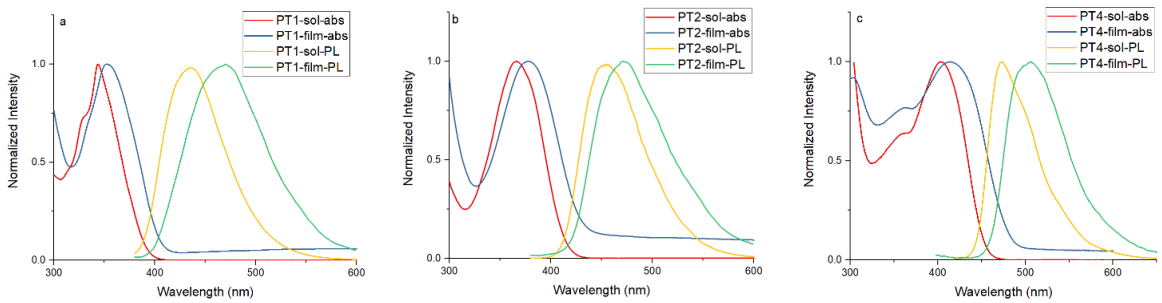

Figure 2.2. Absorption and PL spectra of a) PT1, b) PT2 and c) PT4 in the concentration of 10^{-5} M at room temperature.

Table 2.1. Summary of photophysical details of PT1, PT2 and PT4 in 10^{-5} M chloroform and as thin films.

	PT1	PT2	PT4
LE state lifetime	2.75 ns	1.67 ns	1.78 ns
ICT state lifetime	10.27 ns	2.81 ns	2.15 ns

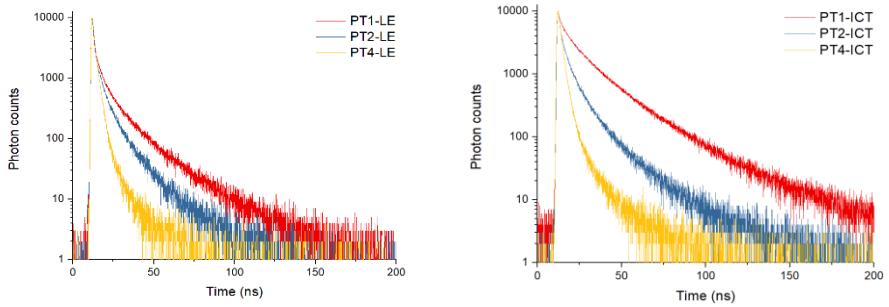

Figure 2.3. PLQY lifetime measurements of PT1, PT2 and PT4 as thin film.

Table 2.2. PLQY lifetime values of PT1, PT2 and PT4 as thin film.

	Solution					Thin film				
	abs, max /nm	PL, max /nm	abs, onset / nm	Energy gap /eV	PLQY /%	abs, max /nm	PL, max /nm	abs, onset /nm	Energy gap /eV	PLQY /%
PT1	343	432	395	3.13	100	360	475	409	3.03	95
PT2	367	455	420	2.95	100	380	485	440	2.81	90
PT4	400	474	457	2.71	85	430	530	490	2.53	74

Molecular packing has significant impacts on solid-state PLQYs.[40] We thus investigated how the molecules are arranged through single crystal X-ray diffraction (SCXRD) (Figure. 2.4). The dihedral angles between theobromine and pyrene are relatively large: 63°, 80° and 47° for PT1, PT2 and PT4 respectively. These large dihedral angles are caused by the steric repulsion between pyrene and the adjacent methyl group on theobromine. This steric repulsion forces these molecules to adopt a twisted conformation which prevents the π-π interaction between pyrene cores. Figure 2.4 shows the crystalline molecular arrangement of PT1, PT2 and PT4. While each compound has different packing patterns, in all cases theobromine drives self-assembly, due to strong polar interactions between the lactam groups. Meanwhile, the pyrenes and alkyl chains are arranged according to the positioning of the theobromine moieties. As a result, adjacent pyrenes are separated from each other, effectively suppressing pyrene's ACQ in the solid state.

As shown in Table 2.2, increasing the theobromine ratios leads to spectral redshifts in absorbance and emission, which implies that theobromine is conjugated to the luminophore it attaches to. This presents an apparent contradiction with the large dihedral angles observed by SCXRD, which would limit any such conjugation. It is proven feasible and widely applied using gas-phase density function theory (DFT) simulations as close approximations for spincoated films considering their amorphous nature. Molecular orbitals (MOs) were simulated based on B3LYP functional and 6-31g (d) basis set to investigate the apparent conjugation between theobromine and pyrene despite the large dihedral angles. Notably, there is an unusual distribution in the ground state (S0) MOs of both PT1 and PT2, as circled in Figure 2.5. Despite the large dihedral angle between the pyrene and theobromine moieties, 63° for PT1 and 80° for PT2, the orbital symmetries allow for MO overlap between the two moieties, intertwining around the single bond linkage. On

the other hand, with a relatively smaller dihedral angle of 47°, the MOs of PT4 extend through the molecule as commonly seen in other planar conjugated structures.

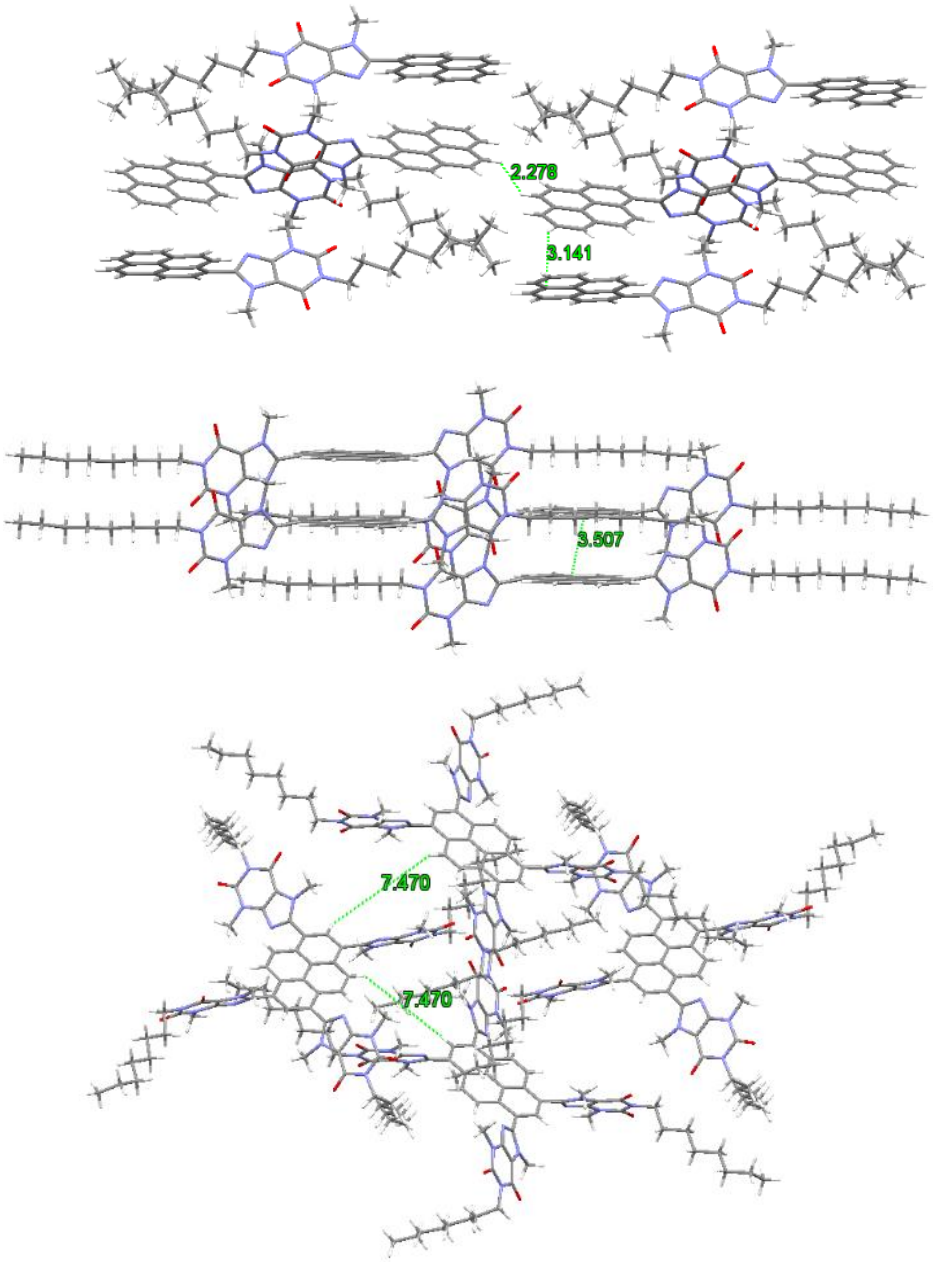

Figure 2.4. Crystal structures of PT1 (Top), PT2 (middle) and PT4 (bottom). H atoms, C atoms, N atoms and O atoms are labelled in white, grey, blue and red respectively. Distances between pyrenes moieties are given in green in the unit of Å.

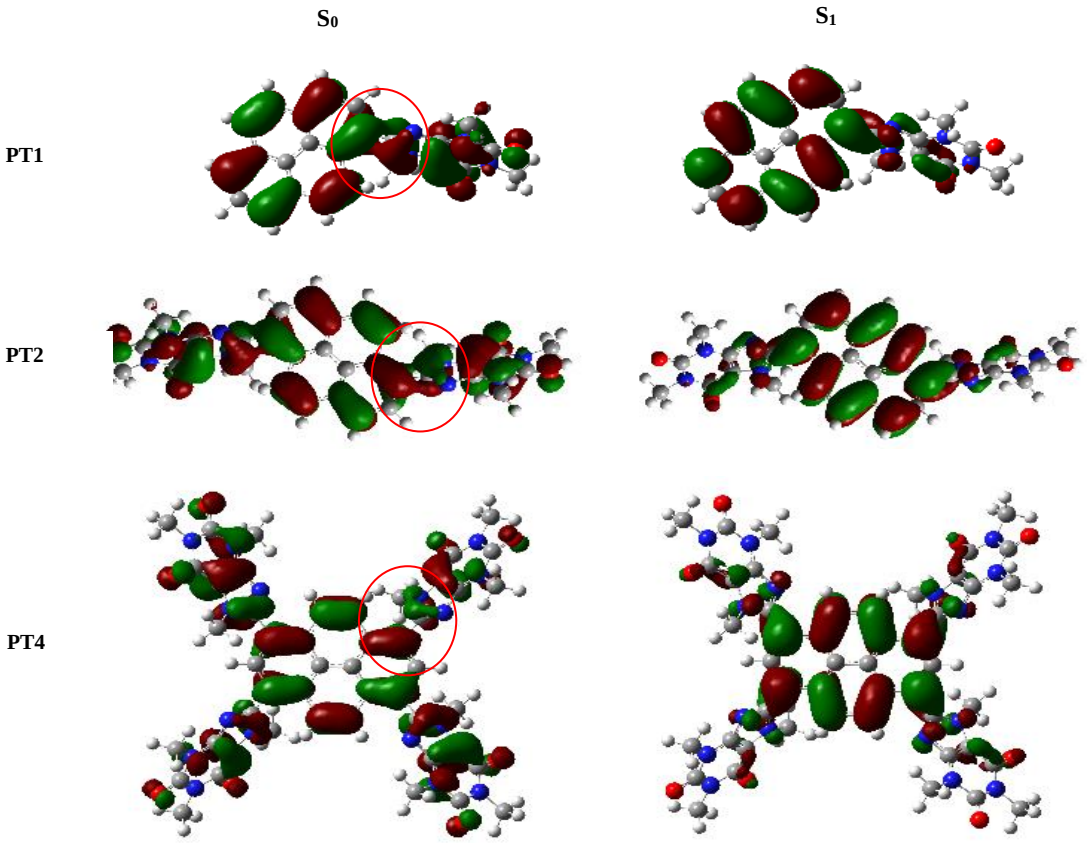

Figure 2.5. Ground state and excited state MOs of PT1, PT2 and PT4. The red circles highlight the differences of MOs at the pyrene-theobromine linkage.

In all three molecules, the MOs are spread out among the whole molecule in S_0, while in the first singlet excited state (S_1) the MOs are more localized onto the pyrene moieties. Therefore, their $S_0 \rightarrow S_1$ transitions contain a major part of locally excited (LE) transition of pyrene and a minor part of an intra-molecular charge transfer (ICT) transition from theobromine to pyrene. This implies that the S_1 MO is a hybridized local and charge-transfer excited (HLCT) state, as a result of LE state and ICT state inter-crossing.[42,43] HLCT states were further confirmed by solvatochromic experiments in PT1, PT2 and PT4, as shown in Figure 2.6. HLCT states are crucial for the design of next-generation electroluminescence devices, where triplet excitons are converted

into singlets excitons for fluorescence, breaking the theoretical limit of fluorescence devices. Notably, previous research has pointed out large dihedral angles are responsible for the formation of HLCT states and DFT simulations have shown that the energy curves of LE state and ICT state can crossover when its dihedral angle is sufficiently large.[44] Using our method, attaching theobromine moieties onto luminophores via direct arylation, one can easily introduce large dihedral angles into organic luminophores, thus inducing HLCT states in resulted materials.

As shown in Table 2.2, these pyrene-theobromine compounds possess high solid-state PLQYs and large Stokes shifts, which make them potential candidates for organic laser application.[45] We therefore studied their waveguiding properties in the solid state. When photopumping of the film is intense enough, spontaneously emitted photons are waveguided through the gain medium and amplified by stimulated emission, resulting in amplified spontaneous emission (ASE). To measure their ASE thresholds, a 375 nm laser beam was focused through a cylindrical lens into a stripe and used to photoexcited the thin film at a normal angle. Emission was collected from the edge of the film. Figure.2.8 shows fluence-dependent emission spectra of a 90 nm thin film of PT2 on a glass substrate. Its output spectrum significantly narrowed as the excitation fluence was raised above 20 $\mu J/cm^2$. This spectral narrowing was accompanied by a sudden increase in output intensity vs. excitation fluence curve (Figure 2.8b). Taken together, Figure 2.8a & 2.8b indicate that the ASE threshold for PT2 is 20 $\mu J/cm^2$. In contrast, we did not observe ASE in PT1 and PT4 films of ~50 nm. Although emission was waveguided through the excitation area, PL emission intensity increased with pump intensity only in a linear fashion over several orders of magnitude (Figure. 2.7 & 2.9). We were not able to obtain smooth films of 90 nm from PT1 and PT4 because of the poor film-forming ability of small molecules in general.[46,47]

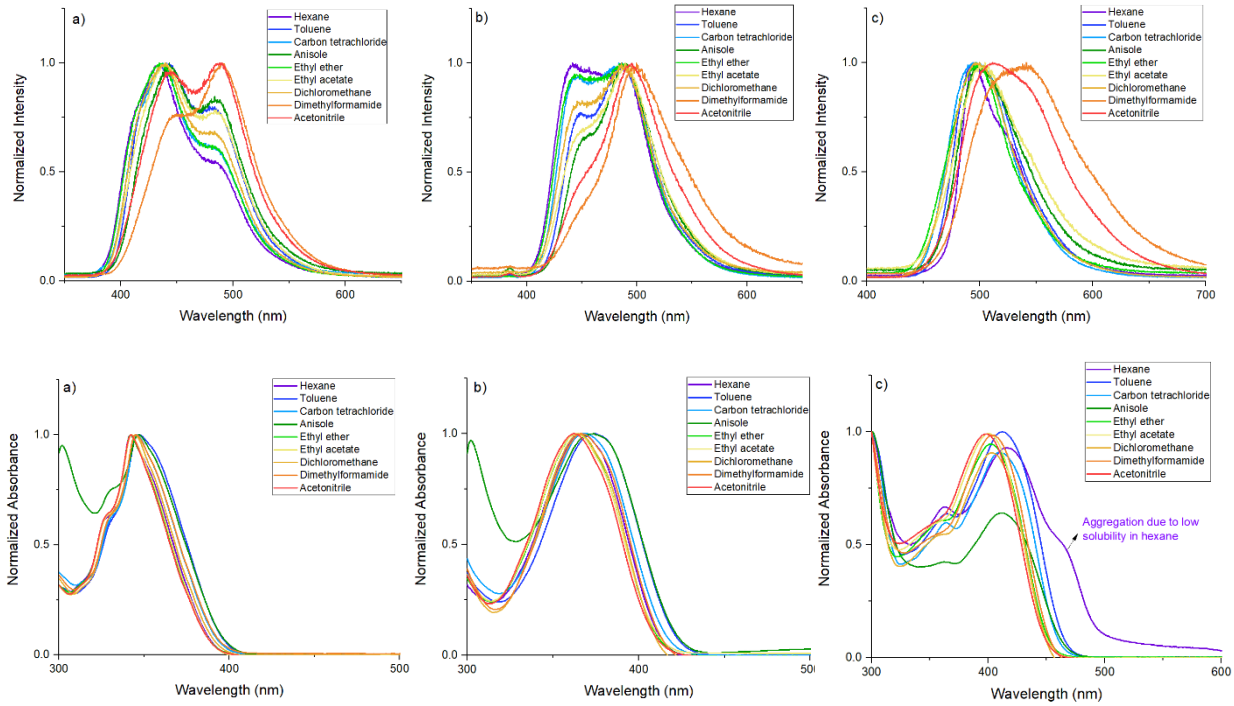

Figure 2.6. (top) PL solvatochromic experiments of a) PT1, b) PT2 and c) PT4 in the concentration of 10^{-5} M at room temperature. (bottom)Absorption solvatochromic experiments of a) PT1, b) PT2 and c) PT4 in the concentration of 10^{-5} M at room temperature.

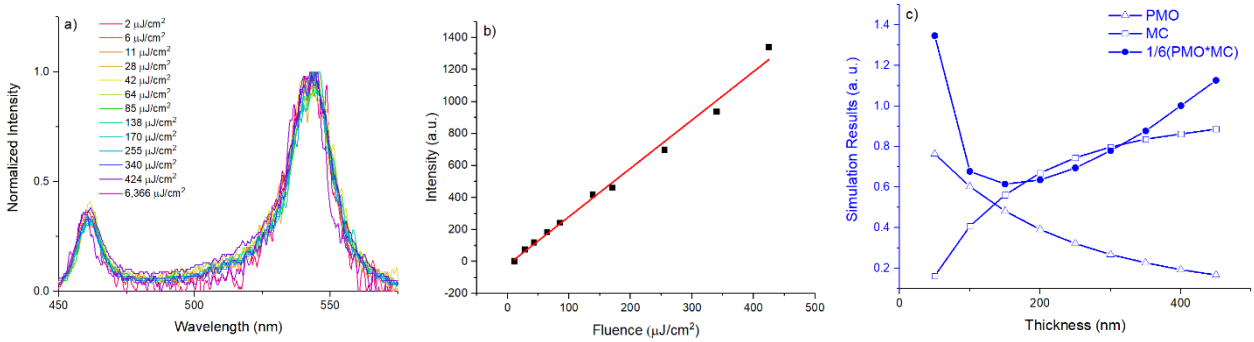

Figure 2.7. a) Emission spectra of a ~50 nm thick PT1 film collected from the edge with different excitation. b) Output intensity from the film edge as a function of the excitation fluence. c) PMO and MC modelling of PT1 and PMO*MC was scaled to fit in the same plot.

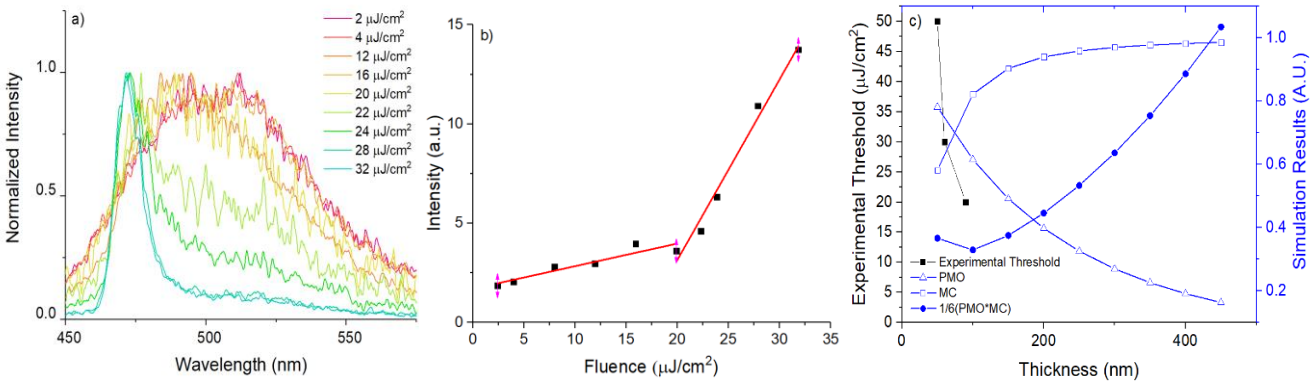

Figure 2.8. a) Emission spectra of a 90 nm thick PT2 film collected from the edge with increasing excitation fluence. b) Output intensity from the film edge as a function of the excitation fluence. c) PMO and MC modeling of PT2 and PMO*MC was scaled to fit in the same plot; experimental thresholds are plotted within for comparison.

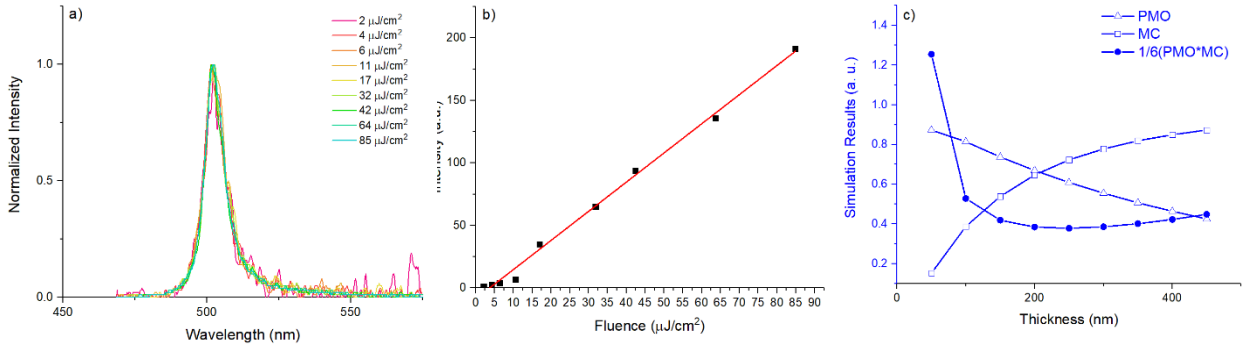

Figure 2.9. a) Emission spectra of a ~50 nm thick PT4 film collected from the edge with different excitation. b) Output intensity from the film edge as a function of the excitation fluence. c) PMO and MC modelling of PT4 and PMO*MC was scaled to fit in the same plot.

It is well-known that ASE threshold is dependent on film thickness,[47] and Bradley *et al.* calculated that a film thickness of 40 – 70 nm, depending on the compound, is a prerequisite for ASE.[48] We did not observe ASE in the 50 nm films of PT1 and PT4, likely because their thickness cut-offs are located at the upper end of 40 -70 nm range. We next investigated the theoretical thickness for the lowest ASE threshold in PT2 films based on the method reported by Anni *et al.*,[46] using optical constants determined via a previously reported transfer matrix method[49] (Figure 2.10). Briefly, we assume that the ASE threshold thickness dependence is governed by two factors: (1) the spatial overlap between the pump electric field and the guided mode (pump mode overlap,

PMO in Figure 2.7c, 2.8c, 2.9c) and (2) the fraction of the guided mode that exists within the organic film (mode confinement, MC in Figure 2.7c, 2.8c, 2.9c). We simulated the waveguiding of 0-1 emission, resolved from low-temperature PL measurements (Figure 2.11) in a SiO_2-PT film-air slab waveguide. Figure 2.7c, 2.8c, 2.9c show MC and PMO in the waveguide as a function of film thickness. The ASE threshold, which is inversely proportional to the product of PMO and MC,25a reached a minimum around 100 nm. This is consistent with our thickness-dependent ASE measurement, where ASE thresholds of PT2 decreased from 50, 30 to 20 $\mu J/cm^2$ as the film thickness increased from 50, 60 to 90 nm. No ASE was observed in PT2 film of 30 nm, in agreement with the calculation by Bradley *et al*.[47]

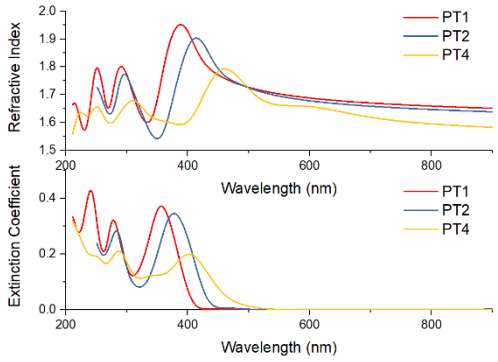

Figure 2.10. Refractive index and extinction coefficient used for ASE threshold simulation.

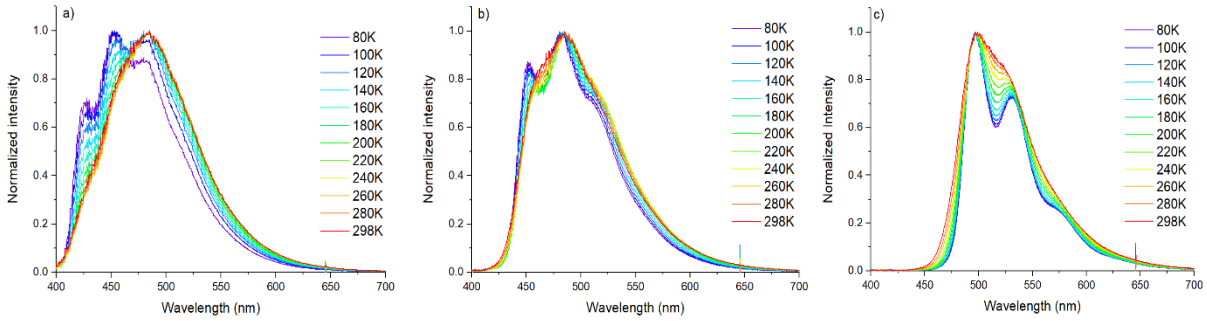

Figure 2.11. Temperature dependent PL spectra of a) PT1, b) PT2 and c) PT4 in chloroform solution with the concentration of 10^{-5} M.

2.4 CONCLUSION

In this paper, we demonstrated that ACQ in pyrene can be effectively suppressed by modifying them with theobromine moieties via direct arylation. With this green and low-cost method, we synthesized three highly fluorescent pyrene-theobromine prototypes in two steps. SCXRD results showed the intermolecular π-π interaction between pyrenes were hindered due to the large dihedral angles introduced by theobromine moieties. As a result, ACQ was suppressed in these compounds and they are highly emissive both in solution and as solid. In addition, large dihedral angles further induce the formation of HLCT states in these molecules, which is verified by DFT simulation and solvatochromic experiments. We further explore their potentials in OL via ASE measurements, where PT2 showed an optimal threshold of 20 $\mu J/cm^2$. In summary, we presented a green and low-cost method to suppress ACQ in organic semiconductors and Dinduce HLCT states at the same time, offering a solution for the scalable material production for next-generation electroluminescence devices.

Chapter 3. GREEN SYNTHESES OF STABLE AND EFFICIENT ORGANIC DYES FOR ORGANIC HYBRID LIGHT-EMITTING DIODES

(This chapter is adapted from a paper published by Yunping Huang during this Ph.D program)[50]

3.1 INTRODUCTION

In the last chapter, we discussed the underlying mechanism that enables the high PLQYs of the theobromine-derived fluorescent dyes, and how their optoelectrical properties, such as absorptions and emission, are largely dependent on the center chromophore.[28] This suggests the optoelectronic properties of the resulting materials can be easily tuned by only changing the center chromophore. In this chapter, we discuss the design and synthesis of a series of theobromine-derived organic phosphors with different center chromophores to expand their spectral coverage. Furthermore, their potential as light converting layers in LEDs is discussed.

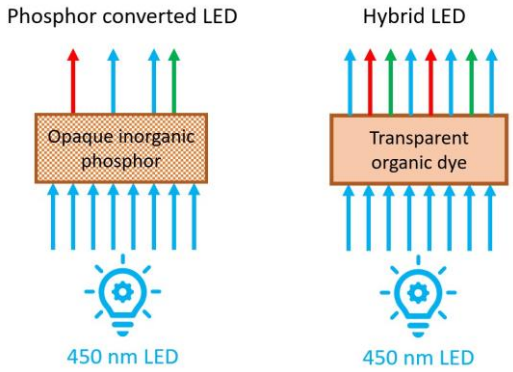

Figure 3.1. The structure comparison between a phosphor-converted LED and an organic hybrid-LED. In phosphor-converted LEDs, a portion of light is scattered and reabsorbed by the LED chip and phosphor powders, which reduces the overall output of the device.

LEDs are the foundation of lighting and display products surrounding us. While they have obtained great success in the commercial market, related research and development activities remain highly active aiming to enhance factors such as energy efficiency, stability, and

environmental sustainability.[9,51,52] Currently, commercial LED products comprise of two key components: an indium gallium nitride LED backlight with emission centered at 450 nm to cover the blue region of the visible spectrum, and powder inorganic phosphors on top converting blue light into longer wavelengths (e.g., green and red) to tune the emission of the device (Figure 3.1). A drawback of inorganic phosphors is that scattering of the emission from the micron-sized phosphor powders leads to substantial backscattering and subsequent absorption of the emission into the LED chip, and reabsorption losses in the phosphor itself, both of which reduce the overall light output of the final LED device.[51,53,54] In addition, there are environmental concerns over the use of inorganic phosphors because they are synthesized from rare-earth and/or heavy metallic elements where mining and refinery activity leads to deforestation, loss of biodiversity and air, water and soil pollution.[51,55-57] Organic dyes possess environmental advantages over inorganic phosphors because they are π-conjugated molecules made from abundant elements (C, H, N, O, etc.) and are potentially bio-sourced. As shown in Figure 3.1, by switching inorganic phosphors in LEDs to organic dyes, the resulting hybrid-LEDs could be manufactured with improved environmental sustainability. Moreover, organic dyes are fluorescent materials capable of addressing the light scattering problems faced by inorganic phosphors, simply by adjusting solubilizing sidechains attached to their fluorescent cores.[27] The appropriate sidechain can hinder the self-aggregation of organic dyes and tune their solution processability, which is crucial for homogeneous materials with high transparency. However, at present most fluorescent dyes are

unstable in ambient conditions due to photooxidation,[58-60] a problem that must be addressed before organic hybrid-LEDs become commercially viable.

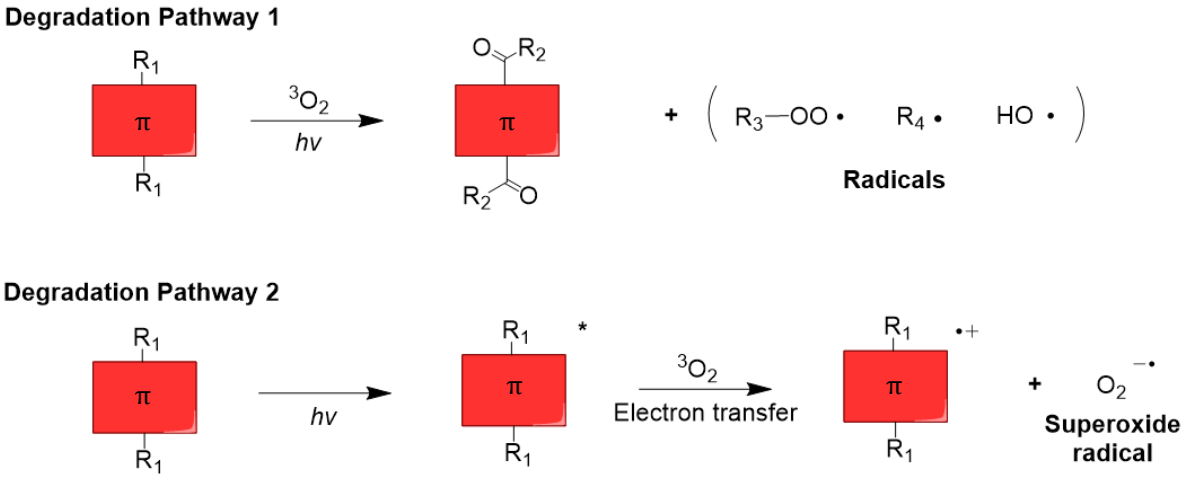

Figure 3.2. The mechanisms generating highly reactive radical species responsible for the breakdown of π-conjugated systems. The LUMO alignments and charge transfer mechanism in degradation pathway 2 will be discussed in Section 3.3.2 and Figure. 3.8.

Figure 3.2 summarizes two major degradation pathways of π-conjugated molecules.[58,59,61-65] Degradation pathway 1 is directly associated with the sidechains of the π-conjugated molecules. Radicals can form on the methylene groups directly bonded to the π-conjugated backbone or heteroatoms with assistance from oxygen.[64] The resultant radicals can subsequently initiate the degradation of the π-conjugated molecule. Degradation pathway 2 is associated with the reactivity of organic dyes towards ground-state triplet oxygen ($^3O_2$) in the atmosphere. When an organic dye molecule is excited by light, an electron will be promoted to the lowest unoccupied molecular orbital (LUMO) from the highest occupied molecule orbital (HOMO). When the LUMO of the organic dye is shallower than the electron affinity (EA) of $^3O_2$ (-3.75 eV), it is energetically favorable for the electron in the LUMO of the organic dye to transfer to $^3O_2$. This is followed by the formation of a radical cation of the π-conjugated moiety and a superoxide radical ($O_2^{-\bullet}$), the latter of which is highly reactive and initiates the degradation of the π-conjugated structure.

Notably, it has been concluded that singlet oxygen ($^1O_2$) has minimal effect on the degradation of the organic semiconductors investigated.[59,66]

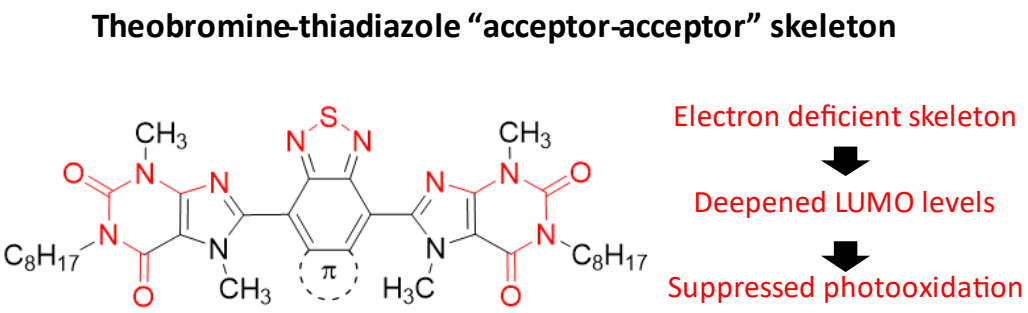

Figure 3.3 The structure of the proposed molecular architecture and its structural characteristics to suppress degradation pathway 2.

Considering the significance of sidechains for transparent high-performance materials, it is more practical to enhance their stability via lowering the energy levels of organic dyes instead of removing sidechains. Introducing electron-withdrawing moieties into organic dye lowers their energy levels. Therefore, in this contribution we present a novel "acceptor-acceptor" skeleton for fluorescent organic dyes with enhanced stability, comprising thiadiazole and theobromine as shown in Fig. 3. Thiadiazole is an electron-withdrawing moiety; its derivatives, such as benzo[c][1,2,5]thiadiazole (BT)[67-69] and naphtho[2,3-c][1,2,5]thiadiazole (NT),[70,71] have been applied in the design of high-performance OLEDs covering wavelengths from green to infrared. Recently, electron-withdrawing theobromine was used in a low-cost and green molecule design that suppresses aggregation caused quenching of fluorescence, which is crucial for synthesizing materials with high photoluminescence quantum yields (PLQYs), while simultaneously enhancing solution processability of organic dyes.[28] Chromophores are covalently linked to alkylated theobromine at the 9-position, sterically repulsing the methyl group at the 8-position of theobromine (Figure 3.3). The resulting molecules therefore adopt highly twisted conformations with large dihedral angles between the chromophore and the theobromine moiety, which prevents

the close interaction among chromophores and therefore suppresses aggregation caused quenching (ACQ) of fluorescence. We hypothesized that by incorporating these two electron-withdrawing moieties in a single molecule, the HOMO and LUMO energy levels would be substantially lowered. This should inhibit degradation pathway 2, an additional benefit along with the previously observed improvements in fluorescence and processability crucial for film transparency. To examine our hypothesis, two molecules consisting of theobromine and thiadiazole, Theo-Green and Theo-Red (Figure 3.3), were synthesized respectively. Four other structurally representative organic dyes were included in the experiment to determine the scope of this hypothesis, which affords a comprehensive understanding of the relationship between structure and photostability.

3.2 MATERIAL SYNTHESIS AND EXPERIMENTAL PROCEDURES

3.2.1 *Synthetic procedures*

Theobromine, 1-bromooctane, R305 DCJTB, 4,7-dibromo-benzo[c][1,2,5]thiadiazole were purchase from TCI. Bis(dibenzylideneacetone)palladium(0) anhydrous xylene and pivalic acid were purchased from Sigma Aldrich. K_2CO_3 and Cs_2CO_3 were ground into a powder and dried at 120 °C overnight before reactions. Reactions were run under N_2 atmosphere using standard Schlenk techniques and detailed synthesis procedures are described below. Theo8[28] and 4,7-dibromobenzo[c][1,2,5]thiadiazole[71] were prepared according to literature procedures. NMR was taken with Bruker 500 MHz spectrometer.

8,8'-(benzo[*c*][1,2,5]thiadiazole-4,7-diyl)bis(3,7-dimethyl-1-octyl-3,4,5,7-tetrahydro-1H-purine-2,6-dione) (Theo-Green). Theo8 (1,932 mg, 7 mmol) and 4,7-dibromobenzo[*c*][1,2,5]thiadiazole (873 mg, 3 mmol), pivalic acid (80 mg, 0.8 mmol) and dried

Cs_2CO_3 (3 g, 9 mmol) were added into a 50 mL round bottom flask. 25 mL *o*-xylene was then adding into the flask, followed by degassing with N_2 flow for 10 min. Tris(2-methoxyphenyl)phosphine (122 mg, 0.194 mmol) and bis(dibenzylideneacetone)palladium(0) (80 mg, 0.088 mmol) were added to the solution under N_2 flow, and the solution turned purple. The flask was then sealed with a rubber stopper and heated to 100 °C. After reacting for 1 day, the system was cooled and filtered. The organic phase was then concentrated under reduced pressure. The crude product was further purified with column chromatography using dichloromethane/methanol in a ratio of 40/5 as an eluent. 1.31 g yellow solid was obtained in 61% yield. ^{1}H NMR (500 MHz, Chloroform-*d*) δ 8.10 (s, 2H), 4.10 – 4.02 (m, 4H), 4.00 (s, 6H), 3.64 (s, 6H), 1.75 – 1.63 (m, 4H), 1.47 – 1.21 (m, 20H), 0.91 – 0.84 (m, 6H). ^{13}C NMR (126 MHz, $CDCl_3$) δ 155.93, 153.11, 151.88, 148.87, 148.10, 132.60, 124.81, 110.04, 42.15, 34.79, 32.30, 30.26, 29.72, 28.62, 27.52, 23.12, 14.56.

8,8'-(naphtho[2,3-c][1,2,5]thiadiazole-4,9-diyl)bis(3,7-dimethyl-1-octyl-3,4,5,7-tetrahydro-1H-purine-2,6-dione) (Theo-Red). Theo8 (1,932 mg, 7 mmol) and 4,7-dibromobenzo[*c*][1,2,5]thiadiazole (1,032 mg, 3 mmol), pivalic acid (80 mg, 0.8 mmol) and dried Cs_2CO_3 (3 g, 9 mmol) were added into a 50 mL round bottom flask. 25 mL *o*-xylene was then adding into the flask, followed by degassing with N_2 flow for 10 min. Tris(2-methoxyphenyl)phosphine (122 mg, 0.194 mmol) and bis(dibenzylideneacetone)palladium(0) (80 mg, 0.088 mmol) were added to the solution under N_2 flow, and the solution turned purple. The flask was then sealed with a rubber stopper and heated to 100 °C. After reacting for 1 day, the system was cooled and filtered. The organic phase was then concentrated under reduced pressure. The crude product was further purified with column chromatography using dichloromethane/methanol in a ratio of 40/5 as an eluent. 1.20 g red solid was obtained in 52%

yield. ^{1}H NMR (500 MHz, Chloroform-*d*) δ 7.97 (ddd, 2H), 7.72 – 7.48 (m, 2H), 4.19 – 3.98 (m, 4H), 3.82 (s, 6H), 3.67 (s, 6H), 1.91 – 1.63 (m, 4H), 1.50 – 1.21 (m, 20H), 0.94 – 0.77 (m, 6H). ^{13}C NMR (126 MHz, $CDCl_3$) δ 155.88, 151.91, 151.46, 148.96, 146.98, 134.70, 129.75, 126.76, 119.65, 109.58, 42.19, 33.95, 32.31, 30.37, 29.73, 28.64, 27.55, 23.12, 14.58.

3.2.2 *Density functional theory calculation results*

Chemical structures of all three molecules were imported from Chemdraw into Gaussview 5.0. Density functional theory calculations were performed using the Gaussian 16 (Revision b.01) software package. Structure optimizations were performed under the B3LYP functional and 6-31g (d) basis set. Once the optimization was complete, the saved checkpoint files were converted to form check files before being converted to cube files using the cubegen utility. The cube files were opened in Gaussview 5.0 and images of the molecular orbitals of each molecule were taken. This work was facilitated through the use of advanced computational, storage, and networking infrastructure provided by the Hyak supercomputer system and funded by the STF at the University of Washington.

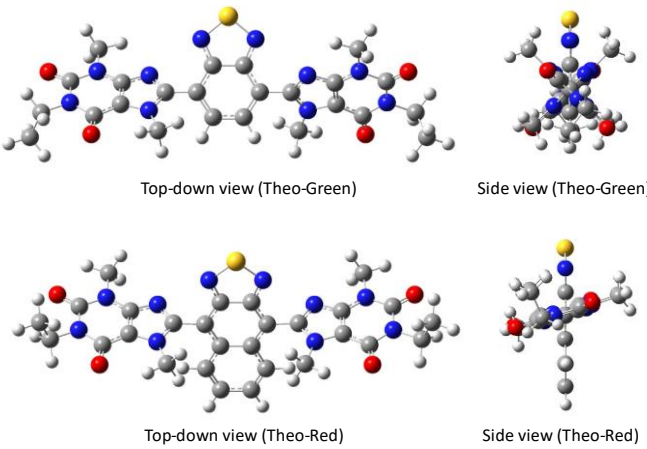

Figure 3.4 Optimized geometry of Theo-Green and Theo-Red.

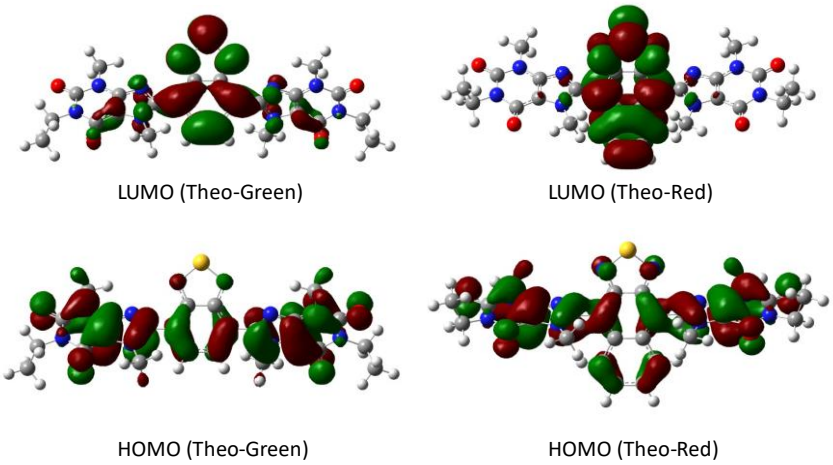

Figure 3.5 Frontial molecule orbitals of Theo-Green and Theo-Red.

3.2.3 *Monitoring singlet oxygen generation*

Procedure: An organic dye (0.005 mmol) and the singlet oxygen scavenger (diphenyl anthracene) (0.005 mmol) was weighed and added into a beaker, and 50 ml anisole was added to the beaker resulting in a clear solution. The dye concentration and scavenger concentration were both 10^{-4} M. The same procedure was repeated for the other organic dyes.

The resulting solutions in beakers were radiated in the open air with a 450 nm LED of ~90 mW/cm^2, and solution samples were collected from the beaker at 0, 20, 40, 60, 80 and 100 min.

The UV-vis spectra of these collected samples were measured, with 10^{-4} M anisole solution of respective dyes as a reference, so that we could directly monitor the changes in the diphenyl anthracene absorption. With the presence of singlet oxygen, diphenyl anthracene will be consumed (Scheme 3.1) and thus will lose its absorption features in the ultraviolet region.[72].

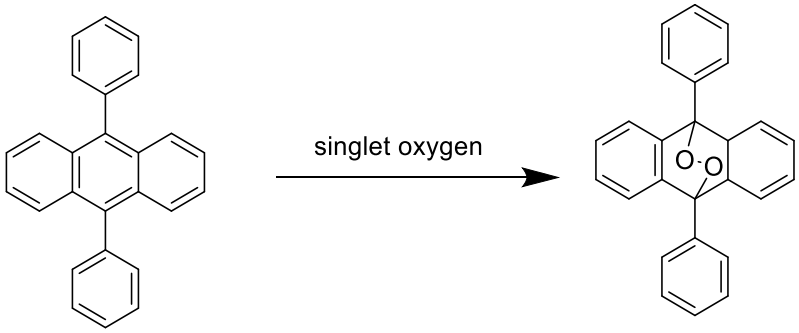

Scheme 3.1 The singlet oxygen scavenging mechanism of diphenyl anthracene.

3.3 RESULTS AND DISCUSSION

3.3.1 *The Streamlined Syntheses of Theo-Green and Theo-Red*

Theo-Green and Theo-Red were synthesized according to Scheme 3.2 using a concise and straightforward pathway. To begin with, an n-octyl chain was attached to theobromine (an abundant non-toxic natural product) to increase the solubility and processability of the final products. Alkylation on theobromine afforded the intermediate in quantitative yield. The second and final step in this simple synthesis is direct arylation, an atom- and step-efficient cross-coupling methodology,[34,35] to couple the octyltheobromine with chromophores of interest to yield the final products. Compared to Suzuki and Stille coupling commonly applied in organic dye syntheses, direct arylation requires no pre-functionalization to the boronic ester or organotin intermediate. This shortens the overall synthetic procedure and bypasses the use of explosive organolithium or toxic organotin compounds, further lowering the cost and environmental risk in industry-scale production.[35] The cross-coupling reaction between octyltheobromine and BT and NT yields the green-emitting Theo-Green and the red-emitting Theo-Red in decent yields, 61% and 51%, respectively.

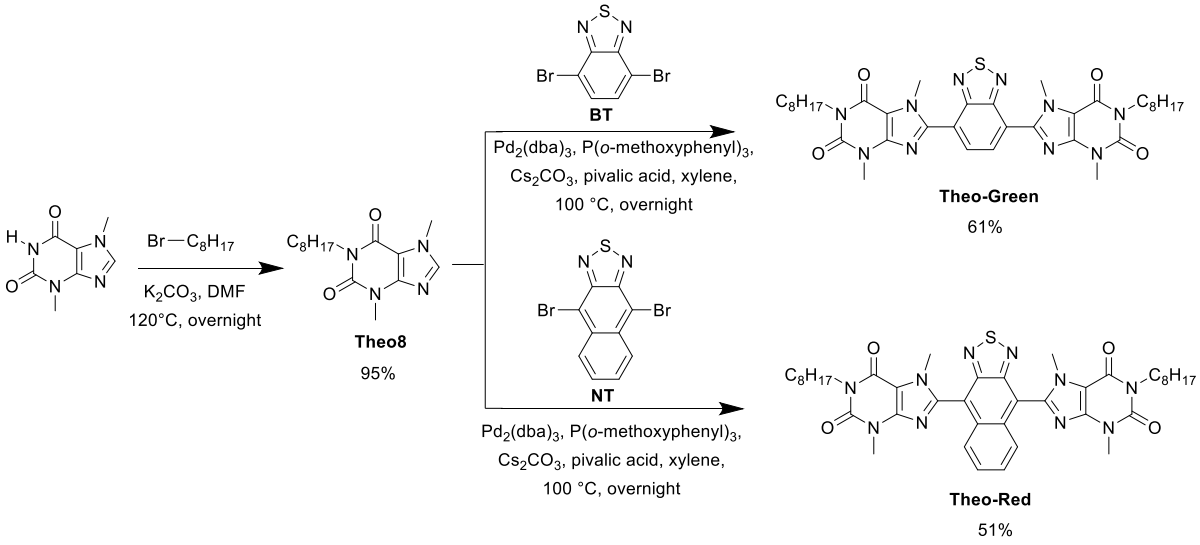

Scheme 3.2 The synthetic routes of Theo-Green and Theo-Red.

Figure 3.4 shows the absorption and photoluminescence spectra of Theo-Green and Theo-Red with the emission spectra of BT and NT for comparison. The PL of Theo-Green and Theo-Red are red-shifted compared to those of their original chromophores, BT and NT respectively, indicating the theobromine moieties are conjugated to the center chromophores. Figure 3.5 shows frontier molecular orbital simulations of Theo-Green and Theo-Red generated based on the B3LYP functional and 6-31g(d) basis set. HOMOs of Theo-Green and Theo-Red extend throughout the whole molecules, while their LUMOs are more localized on the BT/NT core. This indicates a weak charge transfer feature in their HOMO-LUMO transitions while the local excited feature is predominant. The charge transfer feature is more pronounced in Theo-Red as demonstrated by the less spatial overlap between its HOMO and LUMO. This introduction of theobromine extends the conjugation of the BT/NT core and thus led to redshift emissions of Theo-Green and Theo-Red as regards to BT and NT respectively. We observed little overlap between their absorption and emission spectra, which is stemmed from the large dihedral angles between theobromine and the centered chromophores.[28] This minimal overlap between absorption and

emission, namely minimal self-absorption, is essential in minimizing light attenuation within materials and increasing the efficiency of final devices, including not only hybrid-LEDs, but also lasers and luminescence solar concentrators. [45,73]

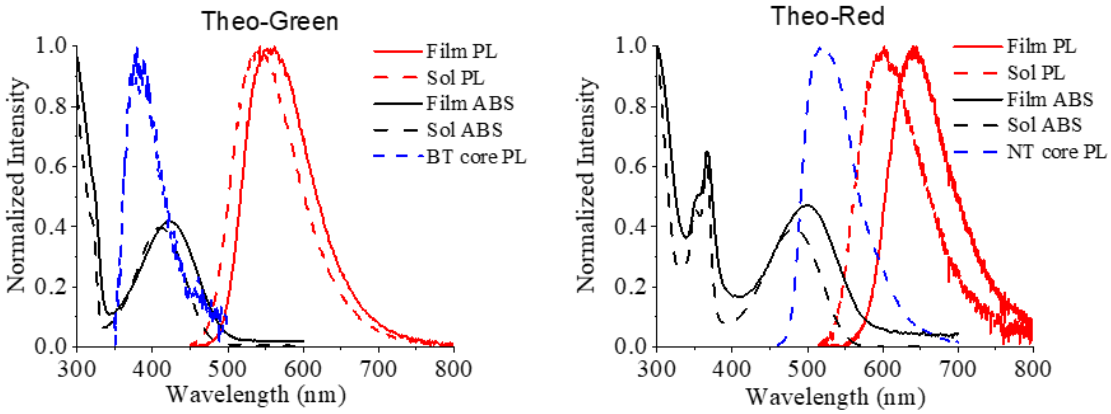

Figure 3.6 The absorption (ABS) and photoluminescence (PL) spectra of Theo-Green (left) and Theo-Red (right) in 10-5 M chloroform solutions (Sol) and as thin films. The PL of benzo[c][1,2,5]thiadiazole (BT) and naphtho[2,3-c][1,2,5]thiadiazole (NT) in chloroform is also included.

3.3.2 *Structure-Photostability Relationship*

Scheme 3.3 shows other organic dyes we studied to illustrate the relationship between structure and photostability. The selection criteria are as follows: First, BT-TPA and Theo-Green both contain a BT core, but the triphenylamine (TPA) moieties in BT-TPA are electron-donating with no side chains. This is in contrast with the electron-withdrawing alkylated theobromine, allowing direct comparison of the two degradation pathways in Fig. 2. It is worth mentioning that TPA is a popular building block for widely applied "donor-acceptor" dye molecules, which is also in contrast to our "acceptor-acceptor" design. Second, the TPA counterpart for Theo-Red, NT-TPA, absorbs little light around 450 nm and was excluded from this study,[74] as 450 nm is a standard backlight for most LEDs and well absorbed by the other dyes. Third, PT4[28] was chosen to better

illustrate the significance of the electron-withdrawing thiadiazole on stability within the theobromine-derived molecules. Compared to Theo-Green and Theo-Red, PT4 possesses a shallower LUMO, as pyrene is electron-neutral while BT and NT are both electron-withdrawing. Most commercial organic dyes are not suitable for light converting applications because of fluorescence quenching.[29] However, R305[73] and DCJTB[75-77] are commercial organic dyes that are well-suited for such applications and thus were chosen to expand the scope of the photostability study. While R305 has deep LUMO levels, the LUMO of DCJTB is significantly shallower due to the presence of the electron-donating aryl amine moiety. Therefore it is expected that these two commercial dyes will have distinctly different photostability parameters. Notably, R305 is one of the most stable fluorescent organic dyes reported thus far, with its fluorescence intensity unchanged during 6-year of outdoor exposure when imbedded in poly(methyl methacrylate) matrix.[78]

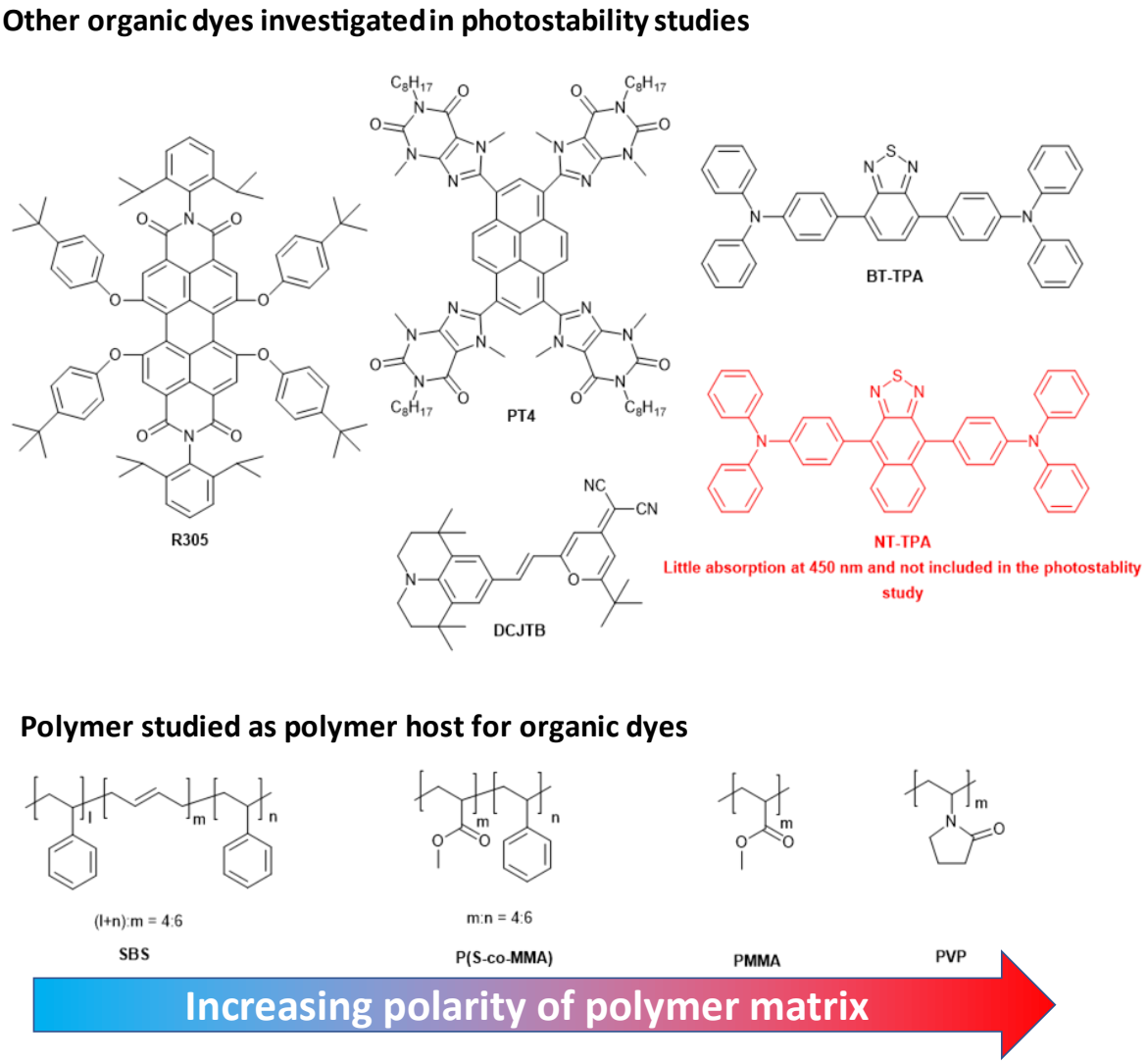

Scheme 3.3 The structures of other organic dyes studied, and polymers screened for the fabrication of light-converting films.

The energy levels of the organic dyes were subsequently determined with UV-Vis absorption spectroscopy and ultraviolet photoelectron spectroscopy (UPS) in tandem. The absolute positions of their HOMOs (E_{HOMO}) were measured by UPS, while their bandgaps (Eg) were calculated from their thin-film absorption onset. The positions of their LUMOs can be estimated with

$$E_{LUMO} = E_{HOMO} + E_g \qquad (1)$$

Cyclic voltammetry (CV) was not appropriate for this study because the energy levels of organic dyes shift when in contact with the polar solvents used to prevent the dissolution of their thin films during CV measurements.[79]

Figure 3.7 shows the UPS He (I) spectra of thin films of Theo-Green, Theo-Red, BT-TPA, PT4, R305 and DCJTB. The energetic position of the top of their HOMOs can be obtained with their highest occupied state (HOS) and cutoffs shown in Fig. 5a & c with this equation:

$$E_{Top,HOMO} = -(21.2\ eV - (E_{cutoff} - E_{HOS})) \qquad (2)$$

We noticed that relative to vacuum level, the top of the HOMOs of BT-TPA and DCJTB are -4.94 eV and -4.85 eV respectively, which is distinctly shallower than that of the other compounds. This can be ascribed to their extra valence bands centered at low binding energies as shown in Fig. 5b, 1.75 eV and 2.00 eV for BT-TPA and DCJTB respectively, corresponding to -5.77 eV (BT-TPA) and -5.82 eV (DCJTB) relative to vacuum level. Considering that the lone pair electrons of trialkylamines have oxidation potential onsets around -5.1 eV (determined by CV),[80] the formation of these shallow band in BT-TPA and DCJTB can be attributed to the tertiary amines in their conjugated systems. The relatively deeper band position of BT-TPA compared to DCJTB can be ascribed to the additional two adjacent phenyls that lower the electron density of the lone pair on the N atom via n-π interaction in BT-TPA. Although there are tertiary amines present in the other organic molecules, their lone pair electrons are closely interacting with electron-withdrawing groups (carbonyl and imine), which leads to the formation of 3-center 4-electron (3c–4e) π bond and the loss of their lone pair features.[40,81] Therefore the other compounds do not have these extra bands at lower binding energies.

The position of the bottom of their LUMOs can be calculated with

$$E_{Bottom,LUMO} = E_{Top,HOMO} + E_g \qquad (3)$$

and the bandgaps of these six compounds are estimated by UV-vis absorption of their thin films according to

$$E_g = \frac{1240}{\lambda_{cutoff}} \text{ eV} \qquad (4)$$

Their LUMO positions and their frontier band structures are visualized in Fig. 3.8. Two LUMO position trends can be observed in this data: 1) molecules that have uplifted HOMOs, BT-TPA and DCJTB, also possess shallow LUMO levels. 2) For molecules with similar HOMO positions (e.g., PT4, Theo-Red and R305) their LUMO positions deepen as their bandgaps decrease.

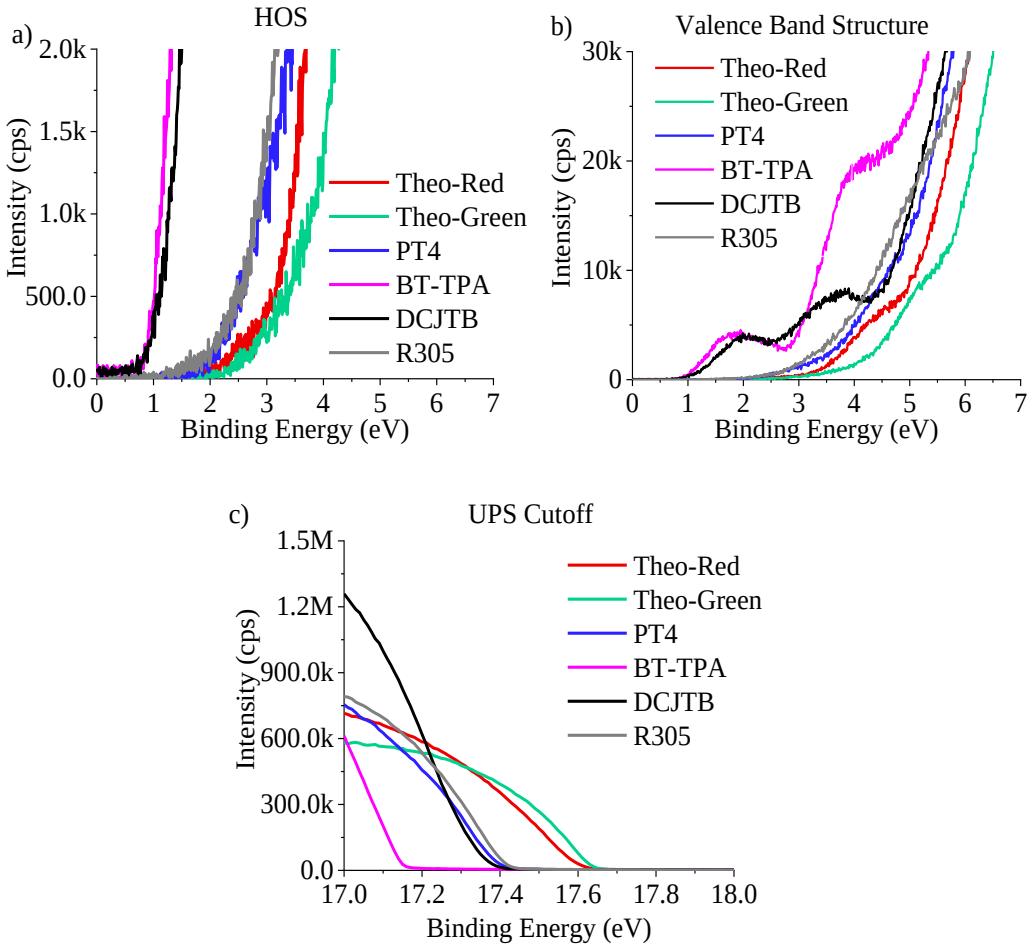

Figure 3.7 UPS results of the six organic dyes.

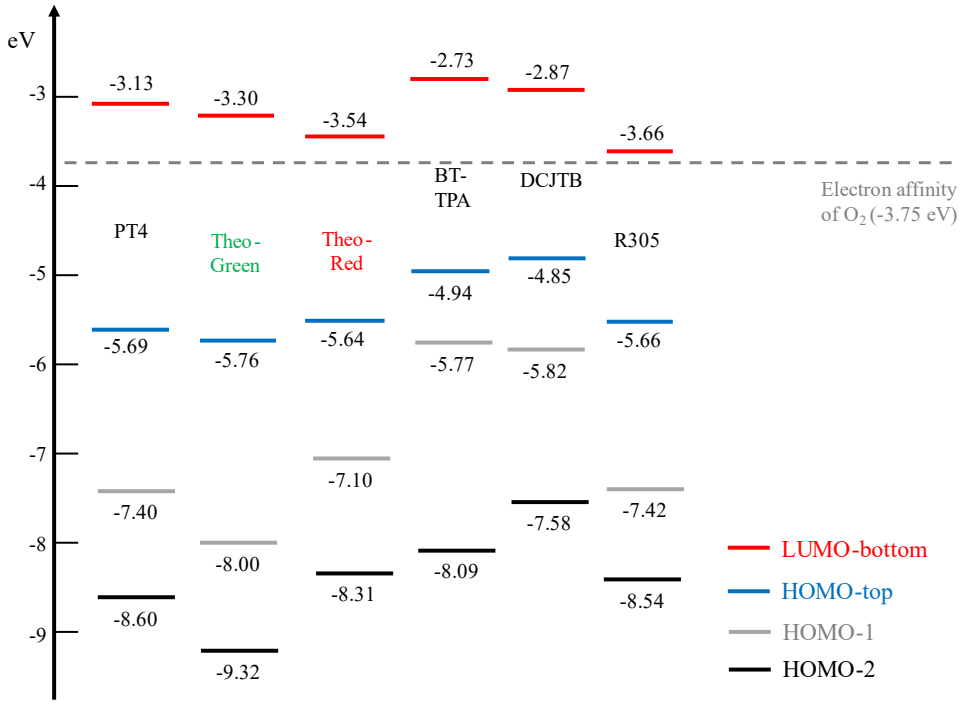

Figure 3.8 Frontier band structures of the six organic dyes of interest.

Photostability measurements were performed to investigate the structure-photostability relationship. The organic dyes were spin coated into thin films in ambient condition. Photostability measurements of these samples were performed at room temperature in ambient condition under constant, full-area excitation by a 450 nm blue LED (the same wavelength as one of the hybrid LED device) while the PL intensity emanating from the edge of the samples was monitored over time. A strong light intensity of ~90 mW/cm^2 was applied in this experiment to accelerate the degradation experiments. Figure 3.9 shows the evolution of integrated PL intensity of the six molecules as a function of irradiation time. The PL signals of these neat film samples rapidly decrease at the beginning of the stability tests and the rate of degradation decreases with time. We speculated that the fast decay is attributed to the degradation of molecules near the solid-air interface, while the slow decay is attributed to the degradation of the molecules farther away from the solid-air interface, where their degradation is limited by the diffusion of molecular oxygen.

This was supported by our degradation experiment of thicker dye-SBS composites, where the fast decay rate changed little compared to the neat films, while the slow decay rate was decreased (see Figure 3.10). Figure 3.10 shows the degradation profiles of these organic dyes in other polymer matrices. We observed the oxygen permeability and the polarity of the polymer hosts have significant impacts on the photostability of organic dyes.

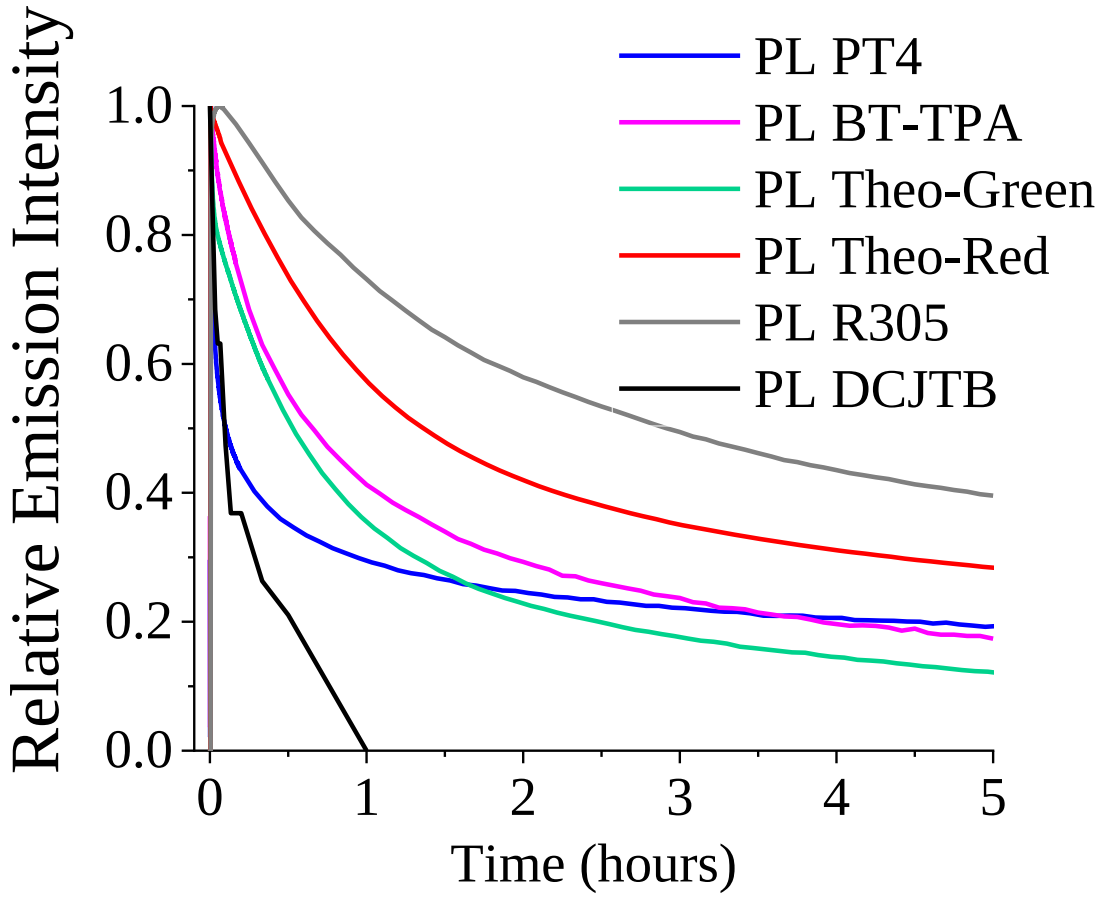

Figure 3.9 PL decays of the organic dyes under 450 nm radiation in air. The PL of DCJTB was measured ex situ with an integrating sphere because of aggregation caused quenching and thus low fluorescence as thin film.

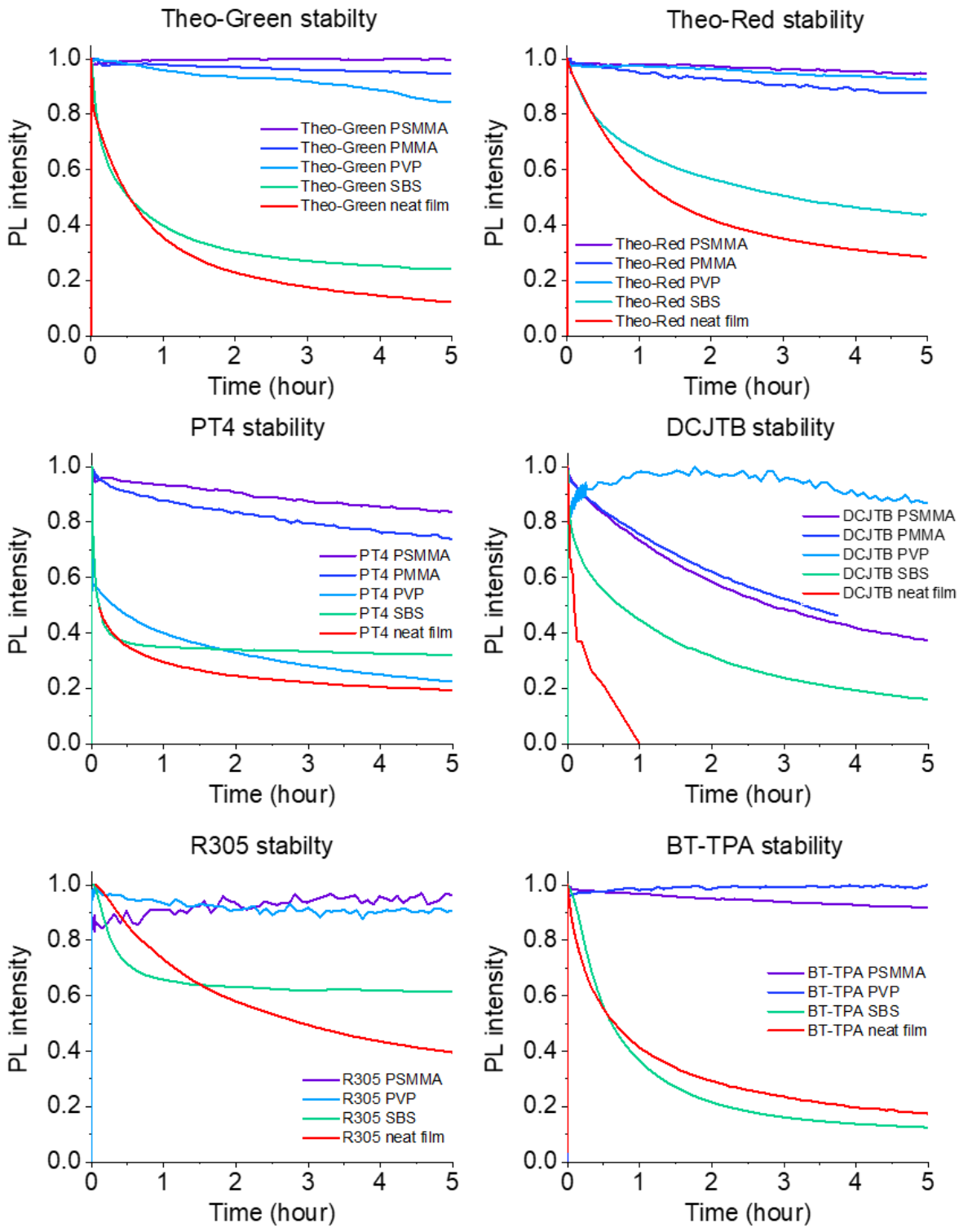

Figure 3.10. Stability results of the organic dyes samples (as thin films and in different polymer matrices).

PT4, BT2, NT2 and R305 have similar structural features (amide groups and alkyl side chains) but different LUMO levels. We observed that R305 has the best stability, followed by NT2, BT2, and PT4, which is consistent with the trend of LUMO depth and increased stability suggested by degradation pathway 2 in Figure 3.2. On the other hand, BT-TPA shows significantly higher stability relative to DCJTB and PT4 despite the fact that DCJTB, BT-TPA and PT4 have similar LUMO depths around -3 eV. This agrees with degradation pathway 1, where the presence of sidechains accelerates the photodegradation of organic dyes. On the contrary, the stability of Theo-Green is comparable to the stability of BT-TPA, even though the six extra side chains per molecule should significantly facilitate degradation pathway 1. This indicates that degradation pathway 2 in Theo-Green is successfully suppressed by modifying the electron-withdrawing theobromine to lower the LUMO energy level. Notably, the degradation mechanism from singlet oxygen formation could be excluded because we did not observe the formation of singlet oxygen from these six molecules under 450 nm radiation, as shown in Figure 3.11, which is consistent with previous work.[59,66] This trend that we observed with these six fluorescent dyes agreed with the trend of non-fluorescent organic semiconductors used in organic solar cells, together providing a more comprehensive understanding of the degradation of organic semiconductors. [58,59,61-65]

Moreover, the above results highlight the importance of the "acceptor-acceptor" design on stability: First, only utilizing one type of acceptor (e.g., PT4) is not sufficient to lower the energy levels enough to decelerate degradation pathway 2, and second, the incorporation of donor moieties is detrimental to stability due to the simultaneous uplifting of HOMO and LUMO (e.g., DCJTB and BT-TPA), which points out the stability drawback of the commonly applied "donor-acceptor" molecule design. While the stability of Theo-Red is significantly improved compared to most dyes, it did not exceed the current stability record of R305. However, Theo-Red substantially

outperforms R305 in hybrid-LEDs due to enhanced fluorescence intensity and transparency, which will be elaborated in the following section.

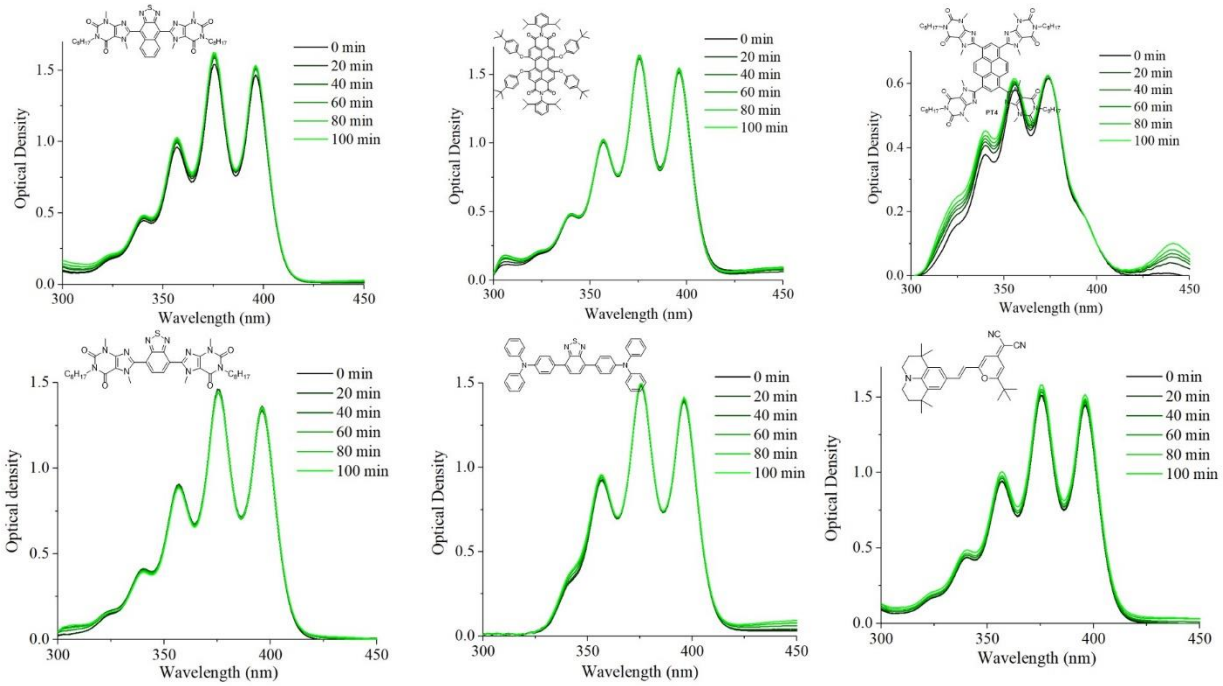

Figure 3.11. The monitoring of singlet oxygen generation from the six organic dyes.

3.3.3 *Lighting-converting efficacy in hybrid-LEDs*

In light of the enhanced stability of the Theo-Green and Theo-Red, we believe these dyes have great commercial potential in hybrid-LEDs. Moreover, Figure 3.6 shows that Theo-Green and Theo-Red have large emission bandwidths with full-width half maximums around 100 nm, which is beneficial to obtain lighting devices with high color fidelity index (CFI). CFI is an updated and comprehensive standard proposed recently to address the disadvantages of the incumbent color rendering index (CRI) standard. [82] Recent results have demonstrated it requires a smaller number of large-bandwidth emitters[83] to achieve high CFIs compared to narrow-bandwidth emitters.[84] As shown in Figure 3.1, there are two major components in a hybrid-LED: a blue light source and a

light-converting layer. In operation, a portion of the blue light emitted from the light source is converted to longer wavelengths by the light converter chosen. As such, the emission of a hybrid-LED is easily tuned by varying the converter, instead of integrating extra LEDs of different colors. The overall efficiency of a hybrid-LED is directly related to the efficiency of the blue LED that converts electricity to blue lights and the efficiency of the light converter that converts blue light into other wavelengths.[51,52]

PLQYs were used to quantify the light converting efficiency of the organic dyes, which can be directly measured by an integrating sphere. Due to the influence of the bandgap law,[85,86] it is challenging to obtain narrow bandgap materials, especially red emitters, with high PLQYs. A narrowed bandgap increases the chance of overlapping of vibronic modes between ground states and excited states within an emitter, which facilitates non-radiative decays via electron-phonon coupling and leads to a reduced PLQY. The PLQYs of spin-coated films of Theo-Green and Theo-Red were 46.4% and 30.2% respectively, even with the presence of the theobromine moieties that suppress aggregation quenching. Therefore, external factors are needed to further increase the PLQYs of these dyes and thus the overall efficiency of a final hybrid-LED.

The polarity of the organic dyes' surrounding environments strongly influences their PLQYs – generally PLQYs decrease with increasing polarity. [67,74] Therefore, the PLQYs of Theo-Green and Theo-Red in solvents of different polarity were measured and summarized in Table 1. The PLQYs of both Theo-Green and Theo-Red decrease as the polarity of the solvents increases, which is consistent with the general trend. High polarity environments intramolecular charge transfer states of the excited molecules, where non-radiative decay is more pronounced due to the limited spatial overlap between their HOMOs and LUMOs.[69]

Table 3.1 The PLQYs of Theo-Green and Theo-Red solution at the concentration of 10^{-5} M measured with an integrating sphere.

Solvent	Polarity Relative to water	Theo-Green [%]	Theo-Red [%]
Hexane	0.009	96.7	91.3
Toluene	0.099	90.9	77.4
Ether	0.117	92.0	63.2
Anisole	0.198	80.5	43.0
Chloroform	0.259	77.5	45.1
Dichloromethane	0.309	71.8	62.6
Acetonitrile	0.460	2.4	0

This polarity-PLQY relationship is also applicable in dye-polymer composites. We blended Theo-Green and Theo-Red with different polymers (listed in Scheme 3.3) at 1 wt% and measured the PLQYs (Table 3.2). It is observed that the PLQY of the dye-polymer composites decrease as the polarity of the polymers increase. In both solution and thin films, the PLQY of Theo-Red has a stronger dependence on polarity than Theo-Green, which can be explained by the stronger charge transfer feature in its excited state (Figure 3.5) and the fact that increased polarity of the environment induces larger special separation between its HOMO and LUMO. A slight decrease in PLQYs were observed with increasing content of Theo-Green or Theo-Red in SBS. This PLQY decrease in higher organic dye concentration is associated with an increase of film polarity, considering the polar nature of theobromine. The higher PLQY of the 20:100 Theo-Red-SBS sample compared to 20:100 Theo-Green-SBS can be ascribed to its limited solubility in SBS and aggregation at such a high concentration (Figure 3.11). SBS yields the highest PLQYs due to its low polarity and thus was chosen for the subsequent fabrication of the hybrid-LED device.

Table 3.2 The PLQYs of Theo-Green and Theo-Red polymer complex with varied blending ratio measured with an integrating sphere.

Polymer host	Film composition Dye:polymer weight ratio	Theo-Green [%]	Theo-Red [%]
SBS	0.1:100	95	90
SBS	1:100	94	87
SBS	10:100	71	61
SBS	20:100	49	56
P(S-co-MMA)	1:100	93	79
PMMA	1:100	91	75
PVP	1:100	80	61

In down-conversion LEDs, PLQYs are also commonly applied in evaluating the light converting efficiency of transparent materials (e.g., organic dyes,[87-89] quantum dots,[90-92] and fluorescent proteins[93-95]). On the other hand, micron-size inorganic phosphors utilize slightly different efficiency metrics compared to the other transparent light converters due to their optically opaque nature; these metrics are external quantum efficiency (EQE) and internal quantum efficiency (IQE). Similar to PLQY, IQE evaluates the non-radiative loss in light conversion. However due to the significant scattering loss within the phosphor powder, it is more accurate to use EQE to describe the down-conversion process of the actual device, leveraging energy loss from both non-radiative decay and scattering.

The scattering loss in transparent composites such as organic dyes and quantum dots are minimal and therefore two parameters are not typically reported and most only report PLQY. As shown in Table S2, the PLQYs of Theo-Green and Theo-Red-SBS composites are comparable to the state-of-art results in recent years.

Table 3.3 PLQY comparison of current state-of-art phosphors from different categories.

Phosphor(@Matrix)	Catagory	Color	Emission peak [nm]	PLQY/ EQE [%]	Reference
Theo-Green@SBS	Bio-derived, organic dye	Green	555	94 [a,d]	This work
Theo-Red@SBS	Bio-derived, organic dye	Red	603	87 [a,d]	This work
PT4@SBS	Bio-derived, organic dye	Green	516	90 [a,d]	Measured
BT-TPA@SBS	Organic dye	Orange	593	92 [a,d]	Measured
R305@SBS	Organic dye	Red	661	59 [a,d]	Measured
DCJTB@SBS	Organic dye	Red	627	37 [a,d]	Measured
DBQ@3DMAC	Organic dye	Green	551	84 [c,d]	96
TAT−FDBPZ@CBP	Organic dye	Orange	576	62 [b,d]	97
4CzTPNBu@ptBCzPO2TPTZ	Organic dye	Orange	576	90 [b,d]	98
BPPZ-PXZ@CBP	Organic dye	Red	607	100 [b,d]	99
mDPBPZ-PXZ@CBP	Organic dye	Red	638	95 [b,d]	99
DBQ@3PXZ	Organic dye	Red	618	76 [c,d]	96
HAP-3TPA@26mCPy	Organic dye	Red	610	91 [b,d]	100
eGFP-AA@TMPE:PMMA	Bio-derived, fluorescent protein	Green	509	80 [a,d]	93
FP@SF	Bio-derived, fluorescent protein	Green	526	65 [a,d]	94
mCherry@PEO	Bio-derived, fluorescent protein	Red	641	18 [c,d]	95
mScarlet@PDMS	Bio-derived, fluorescent protein	Red	600	70 [c,d]	101
$RbNa(Li_3SiO_4)_2:Eu^{2+}$	Micron-size inorganic phosphor	Green	523	44 [c,e]	102
$La_4GeO_8:Bi^{3+}$	Micron-size inorganic phosphor	Red	600	69 [c,e]	103
$Cs_2SiF_6:Mn^{4+}$	Micron-size inorganic phosphor	Red	632	71 [c,e]	104
$Sr[LiAl_3N_4]:Eu^{2+}$	Micron-size inorganic phosphor	Red	649	74 [c,e]	105
$CsPbBr_3@ZrO_2$	Quantum dots	Green	514	90 [c,d]	106
$CsPbBr_3@SiO_2/Al_2O_3$	Quantum dots	Green	519	90 [c,d]	90
$CsPbBr_3$@ZP3/EVA	Quantum dots	Green	519	93 [a,d]	107
InP/ZnSe/ZnS	Quantum Dots	Green	528	95 [c,d]	91
$CuInSe_xS_{2-x}$/ZnS	Quantum Dots	Green	590	95 [c,d]	108
$Ag_{1.3}In_{4.0}Zn_{1.0}S_{4.9}$	Quantum Dots	Red	623	60 [c,d]	92
$CsPbI_3$@ZP4/EVA	Quantum dots	Red	695	85 [a,d]	107
$CuInSe_xS_{2-x}$/ZnS	Quantum Dots	Red	650	95 [c,d]	108

a) Measured in ambient atmosphere; b) Measured in inert atmosphere; c) Measurement condition unspecified; d) PLQY values; e) EQE values; f) Photothermal threshold quantum yield.

Even though the blending ratio of Theo-Green and Theo-Red must be kept around 1 wt% to maintain high PLQYs around 90%, the low blending ratio is sufficient for hybrid-LED applications. Fig. 8 shows SBS blends of the Theo-Green, Theo-Red, other organic dyes and a commercial inorganic phosphor with and without UV irradiation. The dye-SBS samples appear to generate sufficient photoluminescence intensity for hybrid-LEDs when the dye:SBS ratios were a scant 1:100. However, the micron-sized inorganic phosphor SGA isophor® from Sigma Aldrich required ~100 times more material to achieve comparable output intensity. This can be ascribed to the fact that micron-size inorganic phosphors are unable to form a homogeneous film and excitation light can easily leak through between particles. This highlights the advantage of the organic dyes in light converting applications regarding material consumption, which helps further lower the cost of final hybrid-LED products in a significant way.

The SBS blends of Theo-Green, Theo-Red and BT-TPA appear to have minimal scattering under low blending ratios. However, only the Theo-Green maintained transparency at a high dye:SBS ratio of 20:100; Theo-Red and BT-TPA appear hazy at a blend ratio 10:100. Transmittance measurements were used to quantify the transparency of these samples (Figure 3.12). To eliminate the interference from absorption of the organic dyes, we use the wavelength range from 650 – 700 nm to evaluate the transmission of the different light-converting films. Shorter wavelengths (e.g., wavelengths from 450 - 650 nm commonly used in lightings) are more subjective scattering considering scattering intensity is strongly wavelength-dependent ($\sim\lambda^{-4}$), and thus the film transmittance from 650 - 700 nm provides a fair evaluation for light-converting materials in lighting. In the transmittance results, we find that only Theo-Green maintains high

transmittance at high blending ratios, around 95% for the 10:100 blend and around 90% for the 20:100 samples. As for Theo-Red and BT-TPA, while the transmittance values of 1:100 blends are around 100%, they drop below 20% when the blending ratio is increased to 20:100. This reduced transparency of BT-TPA and Theo-Red can be ascribed to micron-size particles formed in the dye-SBS composites at high blending ratios, while the film of Theo-Green-SBS remained homogeneous (Figure 3.13). The role of the sidechains in solution-processed organic dyes is underlined by these results. Theo-Green and BT-TPA have the same center aromatic unit (BT). Therefore, the difference in transparency must stem from their modifiers – alkylated theobromine endows higher transparency than non-alkylated TPA moieties. Compared with Theo-Green, there is a decrease in transparency in the Theo-Red samples. This is because the larger center aromatic unit (NT) enhances π -π interactions, facilitating the formation of large aggregates. This can be inhibited by changing its octyl sidechain to a longer or branched side chain, which would increase its solubility in the SBS matrix and recover the transparency of the dye-SBS composite. The SBS blends of R305 and DCJTB have limited film transparency due to the formation of micron-size aggregates (Figure 3.13) even at a low blending ratio of 1:100. Their film transparency values are below 80% at low blending ratio of 1:100 due to the presence of small aggregates, and their transparency continues to decrease as the blending ratio increases. This is explained by the fact that these two molecules have planar π conjugated structures, and their intermolecular π -π interactions facilitate the formation of large aggregates that scatter light.[29] This is consistent with the results observed by Kim *et al.* utilizing perylene dyes for micro-LED displays.[109] These traditional organic dyes suffer from aggregation when dispersed in a polymer matrix, which leads to opaqueness and fluorescence quenching even at low concentrations, and thus in their experiment the optimal dye mixing ratio was merely 0.6 wt% and the PLQYs were around 40%. However this

is overcome with our molecular design – we were able to enhance the blending ratio to 10 wt% with PLQY of 70% (Theo-Green), providing approximately 30 times increase in optical output. This emphasizes the advantages of introducing alkylated theobromine in the dye structure – preventing aggregation quenching and increasing solubility in the polymer matrix. Based on this result, the conclusion by Kim *et al.* stating "the overall intensity and color-conversion efficiency of organic dyes are low for down-conversion LEDs" should be reconsidered. SGA isophor®-SBS composite also has low transparency. For both organic dyes and inorganic phosphors, low film transparency is disadvantageous in hybrid-LEDs because it leads to scattering losses, which decrease the overall light output of hybrid-LEDs.[53,54] Notably, because the sizes of traditional inorganic phosphors are usually several microns, the scattering losses in these phosphor-based devices are the most pronounced.[53]

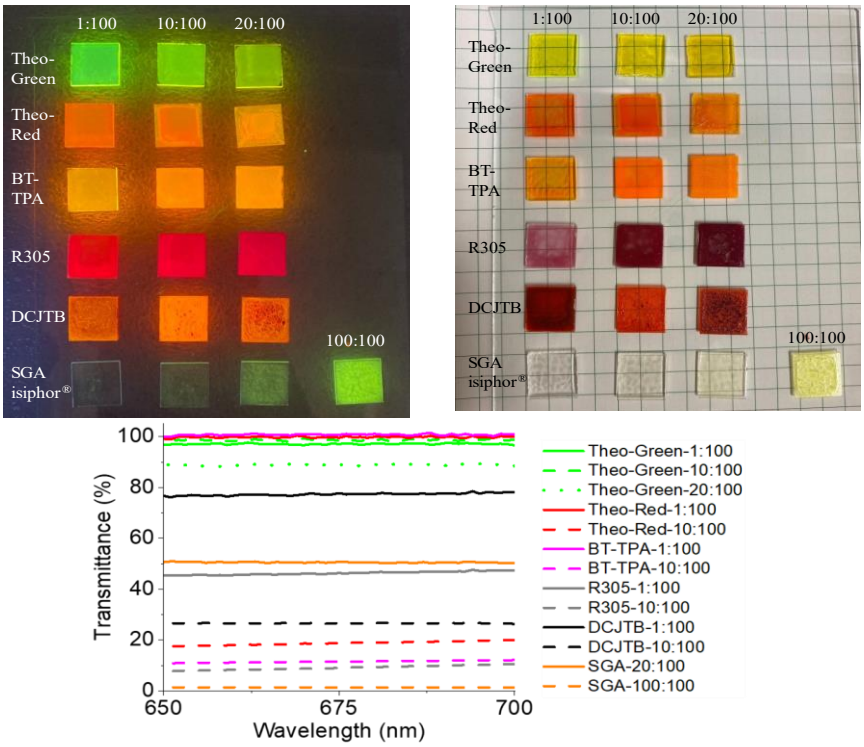

Figure 3.12. Comparison of light converting efficacy (top) and transparency (middle) of inorganic phosphors and organic dyes. Blending ratio (converter:SBS) are also labelled. (bottom) the transmittance of the light-converting films.

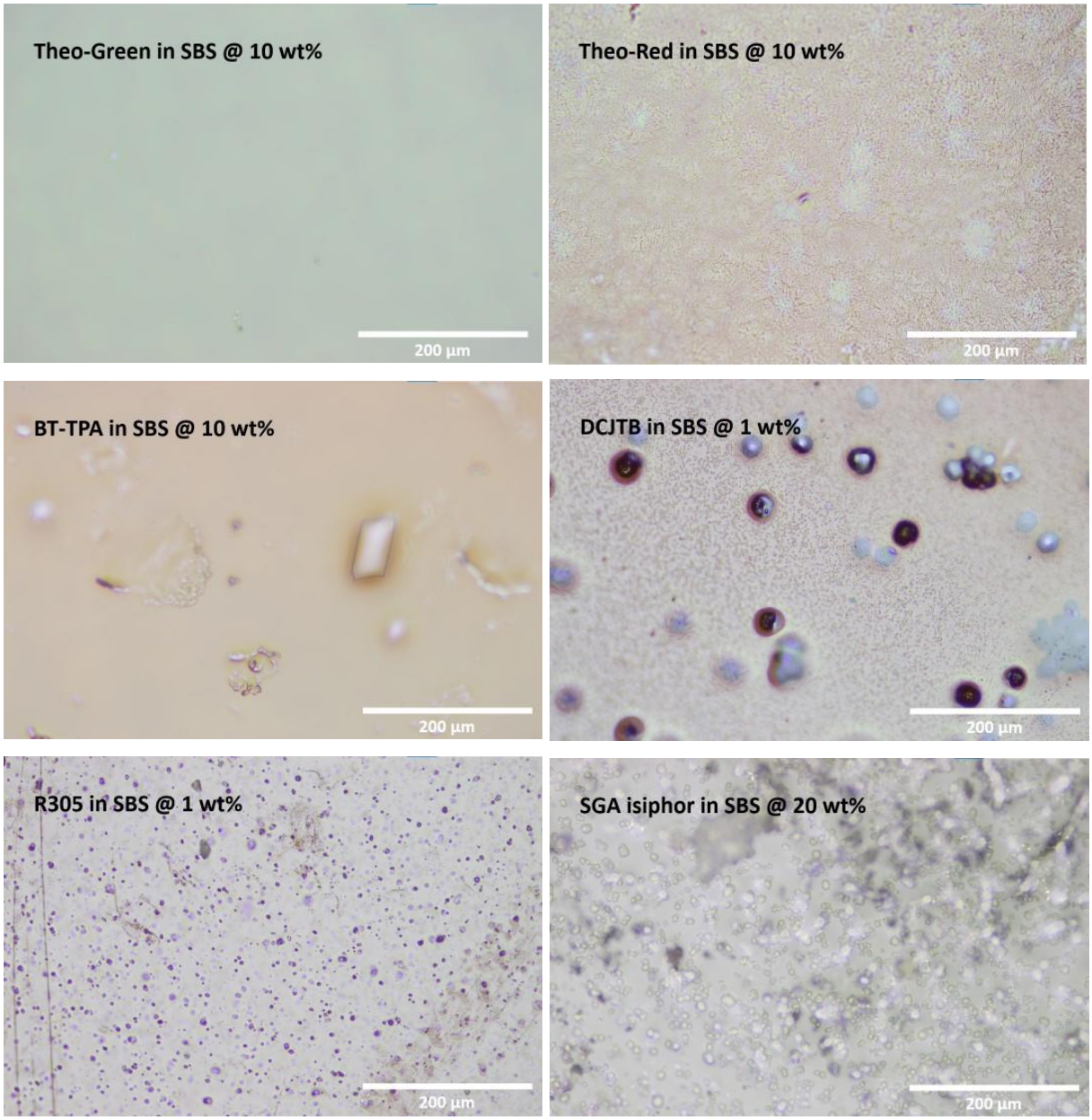

Figure 3.13. Images of the lighting converting composites under optical microscope.

Considering the high transparency of Theo-Green-SBS composite at high dye concentration and its high PLQYs, we subsequently processed it into a waveguide for a non-glare transparent edge-lit device.[110] The dye-imbedded waveguide was fabricated by blade-coating the Theo-Green-SBS (10 wt%) solution onto a 30 cm × 30 cm glass substrate. The edge-lit device was

assembled by coupling inorganic LEDs to the edges of the waveguide. As shown in Figure 3.14, the resulting device overcomes the problematic glares featured in traditional LED lightings, and its transparent appearance comparable to commercial OLED products. We were not able to measure the efficiency of this edge-lit device due to its relatively larger size and dual-side emitting configuration.

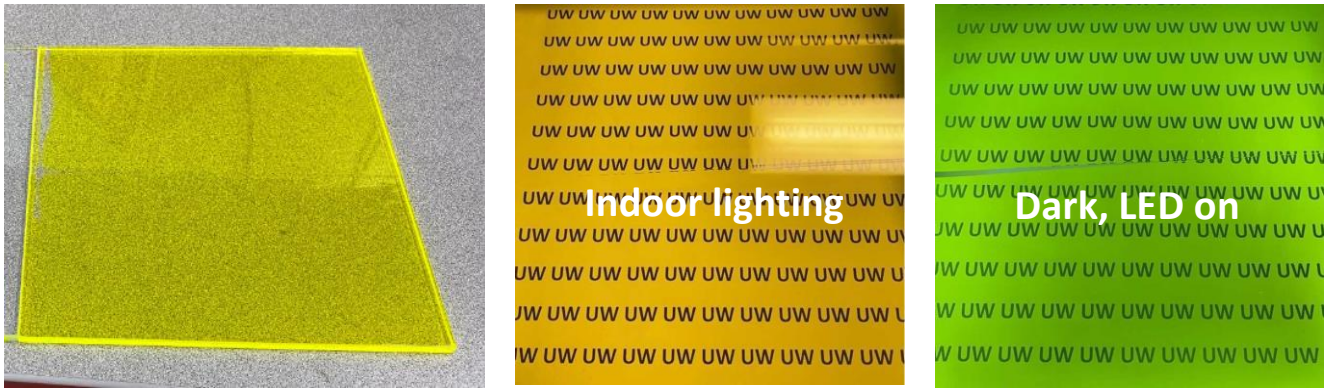

Figure 3.14. (left) as-fabricated waveguide by blade-coating the Theo-Green-SBS composite on a glass substrate; (middle & right) demonstration of transparency and non-glare feature of the edge-lit lighting device based on the waveguide shown on the left.

3.4 CONCLUSIONS

In this paper, we used direct arylation and an abundant non-toxic natural product to synthesize two organic dyes (Theo-Green and Theo-Red) for hybrid-LED application, uniting the advantages of inorganic LEDs and OLEDs. These two dyes are comprised of an "acceptor-acceptor" skeleton featuring theobromine and thiadiazole. It was demonstrated that this "acceptor-acceptor" skeleton significantly lowers the energy levels of resultant organic dyes relative to the electron affinity of triplet oxygen to decelerate photooxidation. While the "donor-acceptor" skeleton is sufficient in tuning the bandgap of organic dyes,[111] it facilitates photooxidation due to the presence of electron-donating units, such as arylamines, increasing the energy levels relative

to the electron affinity of triplet oxygen. In addition to enhanced stability, the “acceptor-acceptor” design results in organic dyes with high PLQY and enables processability optimization through simply sidechain modification. We fabricated highly transparent films when Theo-Green and Theo-Red were blended with SBS, which is crucial to reduce light scattering loss in hybrid-LEDs. In addition, these dye-SBS films achieved PLQYs of around 90% under ambient conditions. Such PLQYs are comparable to the state-of-art results from organic dyes, bio-derived phosphors, traditional inorganic phosphors, and quantum dots achieved in recent years. Taking advantage of the enhanced transparency and PLQY of Theo-Green-SBS composite, we were able to fabricate an edge-lit device utilizing waveguide optics and low-cost inorganic LEDs. The resulting device demonstrated enhanced aesthetics comparable to commercial OLED lightings. Considering the aforementioned enhancements on stability, transparency, PLQY, and aesthetics, these theobromine dyes demonstrate potential in high-performance, environmentally sustainable hybrid-LEDs.

Chapter 4. NATURALLY DERIVED ORGANIC DYES FOR LED LIGHTINGS OF HIGH COLOR RENDERING AND FIDELITY INDEX

(This chapter is adapted from a paper published by Yunping Huang during this Ph.D program)[112]

4.1 INTRODUCTION

Light-emitting diodes (LEDs) are a rare-earth element (REE) based technology with surging market demand.[51] REEs are used in the production of phosphors, a light converter in LEDs to tune their emission spectra based on the needs of different lighting applications. Due to their high energy efficiency, 1,440 million units of REE-based LEDs were installed in the US till 2017, and this number is projected to reach 7,910 million by 2035.[26] However, due to the necessity of mining and refining in REEs productions, environmental concerns such as deforestation, air pollution, and water contamination, have attracted substantial public scrutiny.[55-57] In addition, REE supply is subject to future shortage considering their booming industrial demand and limited supply.[113,114] Conversely, organic dyes are light-converting materials made from organic elements, primarily C, H, N, O, and S, bypassing the need for REEs in light converter production. Therefore, the environmental profile of LEDs can be improved by adopting the organic hybrid LED architecture, switching the incumbent inorganic phosphor to organic dyes as shown in Figure 4.1. Furthermore, the scattering loss from inorganic phosphors can be eliminated due to the high transparency of organic dye composites. [51,53,54]

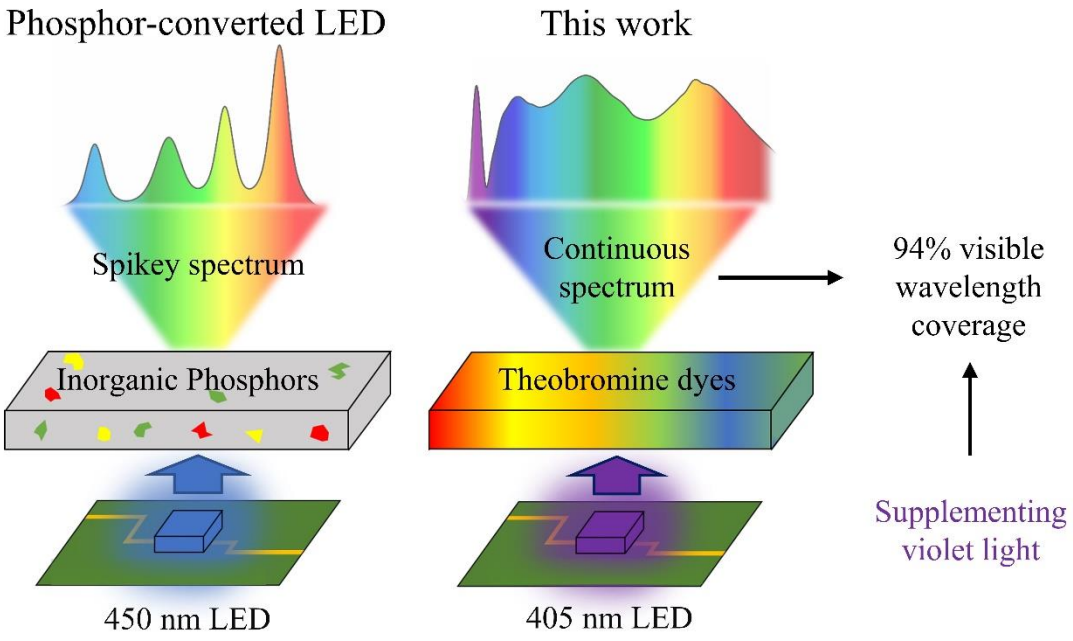

Figure 4.1. Structural comparison between commercial phosphor-converted LEDs and the organic hybrid LED proposed in this paper. Incumbent inorganic phosphors are powderous, introducing scattering loss and reducing the overall light output of the final LED.

To gain industrial interest in organic dyes for LEDs, several issues must be addressed. Price plays a key role in the commercial viability of novel technologies. According to the U.S. Department of Energy, light converting materials typically account for around 24% of the total cost of a 1 W commercial warm-white LED (¢ 80), requiring the cost of the organic dye component to be less than ¢ 19.2.[26] However, the prices of industrially available fluorescent dyes are significantly higher than inorganic phosphors due to their complicated structures that require long synthetic routes and explosive and toxic reagents.[28] In addition, the light converting materials should have high photoluminescent quantum yields (PLQYs) to improve the energy efficiencies of LED devices. For example, cerium doped yttrium aluminum garnet (YAG:Ce) is the most applied REE phosphor in LED lighting partially because it has PLQYs of around 90%.[115]

Currently most commercial LEDs pair yellow-emitting YAG:Ce phosphors with a blue backlight LED. The resulting white light LEDs achieve Color Rendering Indices (CRI, *Ra*) near 80 of 100.[26] However, the current industry CRI standard was first developed in the 1960s for the evaluation of fluorescent lights and as shown in Figure 4.2, *Ra* only evaluates 8 colors.[116] Importantly, despite the fact that our brains weigh red more heavily than other colors, the 60s' CRI standard does not evaluate red color rendering.[117] A good representation of red color is crucial not only in our daily lives (e.g. affecting our skin tones and increasing sales in department stores), but also in life-and-death moments (e.g. surgeries where it helps better distinguish different organs and blood vessels). Therefore, in updated CRI standards, an additional color rendering index for strong red, *R9*, is supplemented, along with *R10*, *R11*, *R12*, *R13*, and *R14* for strong yellow, strong green, strong blue, light yellowish pink, and moderate olive green respectively.[116] Considering that YAG:Ce is the most adopted light converter, and it has a limited emission in the red region, most commercial LEDs have *R9* values below 25. This explains why human skin looks pale in most LED lightings, despite their *Ra* of 80. Therefore, both industrial and academic researchers are developing high-performance red phosphors to improve red emissions in LEDs.[26]

Still, the updated CRI standard is not ideal for assessing light source color rending. Due to the highly non-uniform color space of CRI, color differences are extremely exaggerated in the red region and suppressed in yellow and blue regions.[84,118] Therefore, in 2015, a new evaluation system, TM-30, was developed by the Illuminating Engineering Society of North America that leverages a set of 99 real test samples with color space uniformity and spectral uniformity.[82] In the TM-30 standard, there are two parameters to quantify the rendition of light sources. The Color Fidelity Index (CFI, *Rf*) quantifies the accuracy with which the color appearance of illuminated objects match their appearances under a reference light source (e.g daylight or black body radiation), and

the color gamut index (*Rg*) quantifies the average increase or decrease of the chroma (the degree of vividness of colors) of objects related to those under reference illuminations.

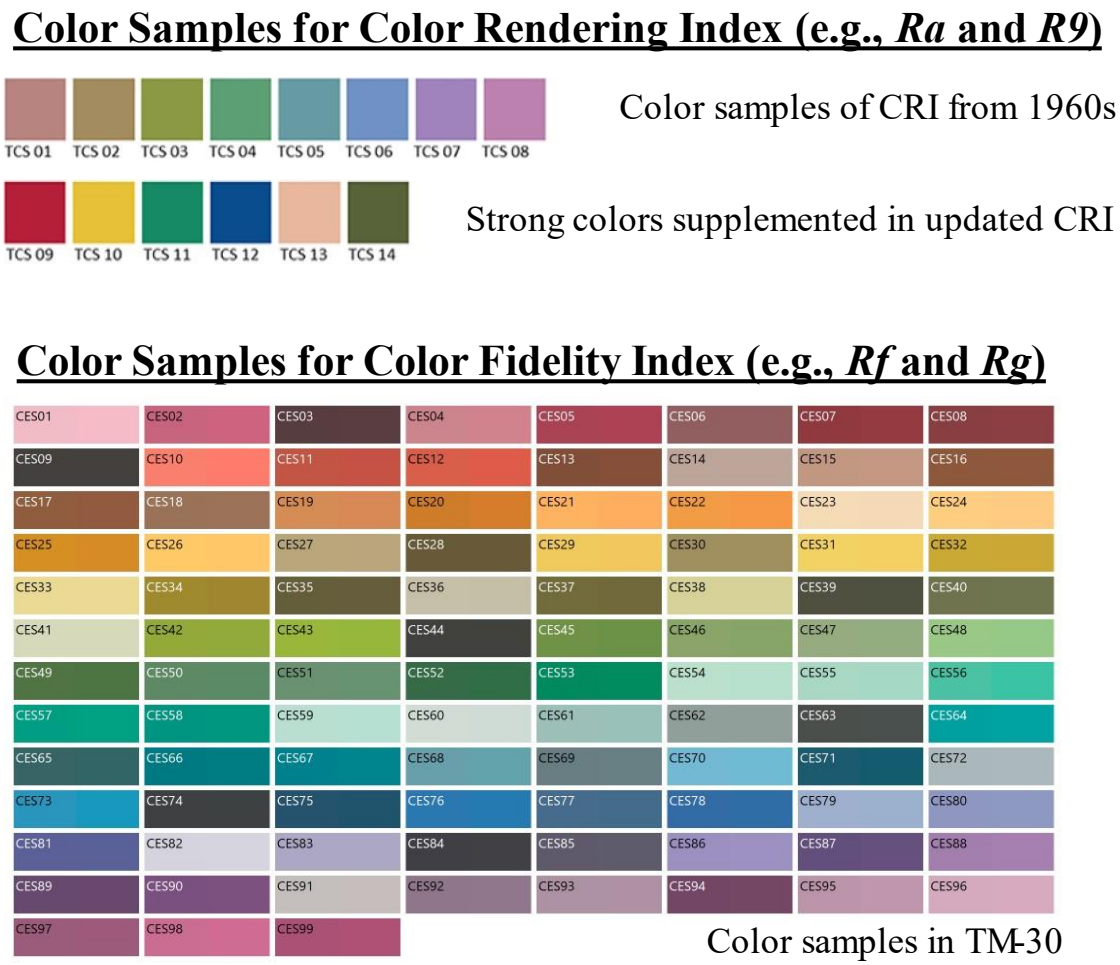

Figure 4.2. Demonstration of color samples of different methods utilized for lighting color quality evaluation.

Both sunlight and black body radiation possess continuous spectra across visible wavelengths. Therefore to achieve high *Rf* and *Rg* values in LED lightings, the phosphor emission spectra should be continuous and uniform across visible wavelengths. Using broad-band emitters can simplify the manufacturing process by reducing the number of phosphors needed to achieve a uniform LED emission spectrum. Recently, our group reported several organic dyes with broad-

band emissions from theobromine, an abundant natural product originally found in cacao beans.[28] The syntheses of these theobromine dyes are streamlined and eco-friendly. The resultant dyes possess high PLQYs when blended with an inexpensive industrial polymer, poly(styrene-butadiene-styrene) (SBS), that serves as the host matrix to enable device integration. Moreover, these dye-SBS composites only require low blending ratios of theobromine dyes, around 1 wt%.[50] In this paper, we further advance the efficacy of theobromine dyes in LED lightings with a new deep red-emitting dye, Theo-Ruby. We developed a white light converter by blending Theo-Ruby with two other theobromine dyes (Theo-Blue and Theo-Green) into SBS. We paired the resulted light-converting dye-SBS composite with a 405 nm LED backlight to generate white emission (Figure 4.1). We further show that the final LED device fabricated with this combination of dyes could achieve a *Ra* of 90 and a *Rf* of 92 with continuous spectral coverage from 400 – 740 nm, corresponding to 94% of visible wavelengths. This demonstrates that extending the emission to the violet region is crucial for high CFIs, in contrast to incumbent LEDs utilizing a 450 nm LED backlight. Moreover, the dyes' low blending ratios significantly reduce the estimated cost of the light converting film to ¢ 1.30 for a 1 W LED, which is significantly lower than the estimated cost of incumbent inorganic phosphor-converted LEDs.

4.2 MATERIAL SYNTHESIS AND EXPERIMENTAL PROCEDURES

Reactions were run under N_2 atmosphere using standard Schlenk techniques and detailed synthesis procedures are described below. Theo8[28] and 4,9-dibromonaphtho[2,3-c][1,2,5]selenadiazole [119] were prepared according to literature procedures. NMR was taken with Bruker 500 MHz spectrometer.

8,8'-(naphtho[2,3-c][1,2,5]selenadiazole-4,9-diyl)bis(3,7-dimethyl-1-octyl-3,7-dihydro-1H-purine-2,6-dione) (Theo-Ruby). Theo8 (1,932 mg, 7 mmol) and 4,7-dibromobenzo[*c*][1,2,5]thiadiazole (1,194 mg, 3 mmol), pivalic acid (80 mg, 0.8 mmol) and dried Cs_2CO_3 (3 g, 9 mmol) were added into a 50 mL round bottom flask. 25 mL *o*-xylene was then added into the flask, followed by degassing with N_2 flow for 10 min. Tris(2-methoxyphenyl)phosphine (122 mg, 0.194 mmol) and bis(dibenzylideneacetone)palladium(0) (80 mg, 0.088 mmol) were added to the solution under N_2 flow, and the solution turned purple. The flask was then sealed with a rubber stopper and heated to 100 °C. After reacting for 1 day, the system was cooled and filtered. The organic phase was then concentrated under reduced pressure. The crude product was further purified with column chromatography using dichloromethane/methanol in a ratio of 40/5 as an eluent. A purple solid was obtained (1 g, 41% yield). ^{1}H NMR (500 MHz, Chloroform-*d*) δ 7.74 (dd, *J* = 7.1, 3.1 Hz, 1H), 7.55 – 7.43 (m, 2H), 4.21 – 3.94 (m, 4H), 3.80 (d, *J* = 26.2 Hz, 6H), 3.73 – 3.51 (m, 6H), 1.83 – 1.58 (m, 4H), 1.50 – 1.20 (m, 20H), 0.88 (dt, *J* = 12.6, 6.8 Hz, 4H). ^{13}C NMR (126 MHz, $CDCl_3$) δ 156.84, 155.41, 151.47, 148.46, 147.00, 141.30, 134.75, 129.37, 126.29, 120.05, 108.99, 41.70, 33.34, 31.85, 29.89, 29.27, 28.18, 27.09, 22.65, 14.09, -0.01.

4.3 Results and Discussions

Scheme 1 shows the synthetic routes to converting alkylated theobromine into Theo-Blue,[28] Theo-Green[50] and Theo-Ruby. In the molecule design, alkylated theobromine increases PLQYs of the final products and their solubility in SBS,[28] while the central π-conjugated luminophores are used to tune their emission wavelengths. These two key components guide the synthesis of theobromine dyes of various emission wavelengths and enhanced PLQYs. Theo-Blue, Theo-Green

and Theo-Ruby were synthesized by cross-coupling alkylated theobromine with pyrene, benzo[c][1,2,5]thiadiazole and naphtho[2,3-c][1,2,5]selenadiazole, affording organic dyes of desired emissions respectively in blue, green and red regions required for high CRI and CFI lightings. It is worth mentioning that the introduction of selenium atom into Theo-Ruby is necessary to achieve sufficient emission in the strong-red and deep-red region (beyond 610 nm) to realize continuous emission across visible wavelengths. It was found that the light-converter fabricated from its sulfur counterpart (Theo-Red) only achieved *Ra* of 70 due to limited spectral coverage beyond 610 nm.[50] This highlights the excellent structural and spectral tunability of organic dyes.

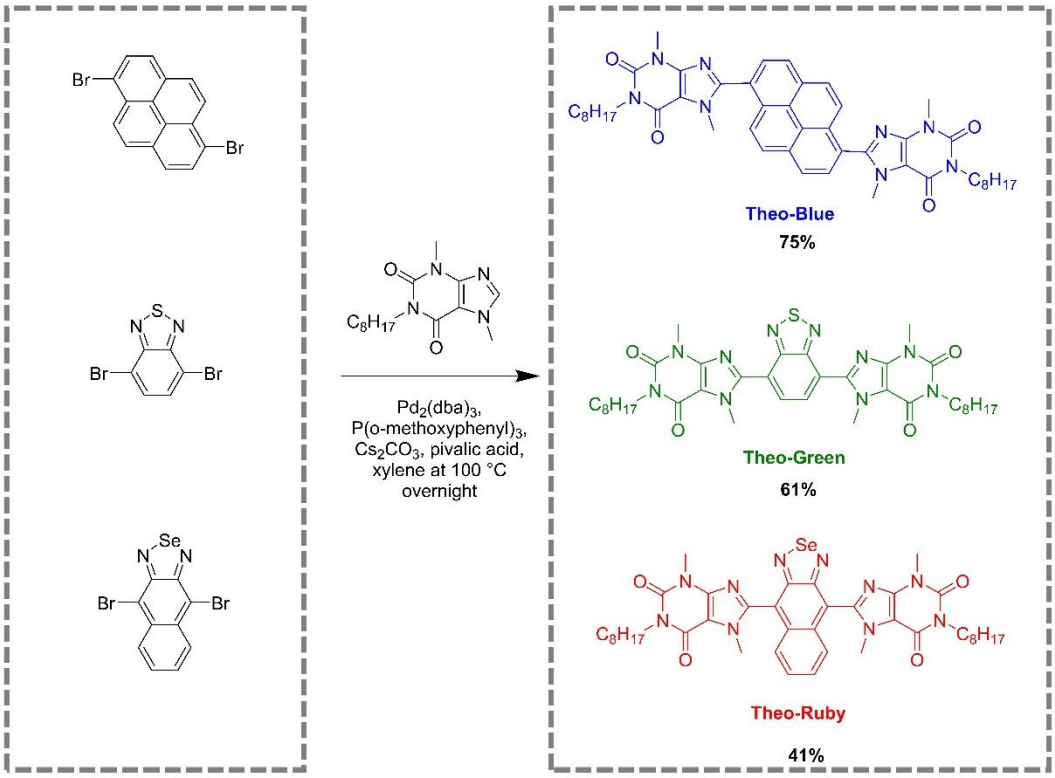

Scheme 4.1. Synthetic route for Theo-Blue, Theo-Green and Theo-Ruby.

In our syntheses, direct arylation was applied to cross-couple alkylated theobromine with the chosen luminophores, instead of Stille or Suzuki coupling commonly applied in organic dye syntheses. Direct arylation is an ascending green and atom-efficient methodology for synthesizing aromatic compounds.[34,35] It directly utilizes a C-H bond for C-C bond formation, and bypasses C-H pre-functionalization required for Stille or Suzuki coupling. This not only shortens the synthetic routes, but also avoids utilizing toxic reagents (e.g., organotin) and explosive reagents (e.g., organolithium) commonly used in C-H bond pre-functionalization. Their streamlined syntheses restrict their production cost to a relatively low range – the cost of Theo-Blue, Theo-Green and Theo-Ruby are respectively $14.6/g, $17.1/g and $45.6/g based on lab-scale estimation (detailed cost breakdowns are shown in SI Section 2). The price of rare-earth phosphors was estimated based on the cost of a 1 W commercial warm-white LED (¢ 80) and the cost percentage (24%) of rare-earth phosphors provided in a lighting report by the Department of Energy.[26] This estimation is close to the procurement costs of lighting manufacturers. On the other hand, our cost calculations of theobromine dyes based on lab-scale synthesis may underestimate cost savings from bulk ordering and process optimization (e.g., solvent recycling) in industrial production.[120] More importantly, the final LED light-converting film only requires around 1 wt% of the theobromine dyes to be blended into an inexpensive industrial polymer, SBS (purchased from Sigma Aldrich at $ 82.4/kg), and thus the overall cost contribution from the theobromine dyes is minimal. SBS, a non-polar polymer, is chosen as the matrix due to the light converting efficiency of the theobromine dyes decrease in a polar environment; moreover, 1 wt% is proven sufficient for LED application because of the high optical density of the dye-SBS film.[50]

To combine these dyes with a 1 W 405 nm LED, the light converting composite is made by dissolving 50 mg SBS, 0.5 mg Theo-Blue, 0.025 mg Theo-Green and 0.025 mg Theo-Ruby

into 0.5 ml toluene and drop casting the resultant solution onto a clean glass substrate. While the cost of the 405 nm LED is comparable to that of 450 nm, the cost of our light converting film is ¢ 1.30, which is significantly lower than ¢ 19.2 for a comparable LED phosphor fabricated with REE phosphors.[26] Notably, the blending ratios of Theo-Green and Theo-Ruby are only 10% of Theo-Blue's. We attribute this to Theo-Green and Theo-Ruby both absorbing light at around 405 nm, and the emission of Theo-Blue overlapping with the absorption of Theo-Green and Theo-Ruby (Figure 4.3). Therefore, within the composite, a portion of the blue light generated by Theo-Blue is reabsorbed by Theo-Green and Theo-Ruby and converted to green and red light, respectively. Similarly, the green light generated by Theo-Green is reabsorbed by Theo-Ruby. We do not believe that energy transfer is taking place between the theobromine dyes since the distance between each molecule is calculated to be around 10 nm (estimated based on the blending ratio of 1 wt%), which would be too large for energy transfer to take place.[121]

Figure 4.3 shows the absorption and photoluminescence spectra of Theo-Blue, Theo-Green, and Theo-Ruby blended in SBS at 1 wt%. These dye-SBS composites have strong absorption from 300 – 420 nm, which enables the use of a violet excitation backlight (e.g. 405 nm used in this paper). Their emissions are respectively centered at 450 nm, 540 nm and 658 nm. Notably, all three theobromine dyes have broad emission bands, with full-width half maximums (FWHMs) of 55 nm, 78 nm and 95 nm. These large FWHMs are ideal for lighting applications because they enable wide spectral coverage of final LED devices.

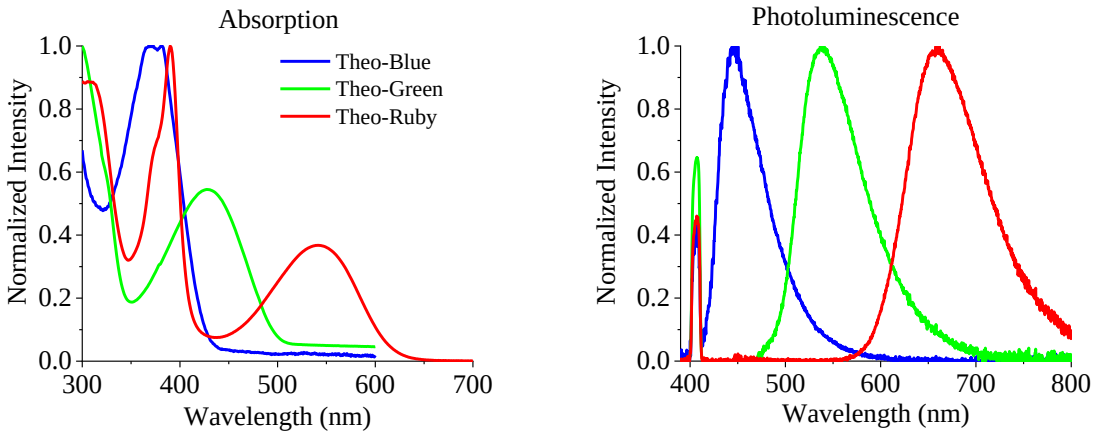

Figure 4.3. Absorption and photoluminescence spectra of Theo-Blue, Theo-Green and Theo-Ruby in SBS at 1 wt% (the narrow peak at 405 nm is attributed to unfiltered excitation light).

Figure 4.4a shows the emission spectra of the hybrid LED device, utilizing a 1 W 405 nm LED chip as the light source and the light-converting dye-SBS composite. Due to the balanced intensity of violet, blue, green and red light, the emission of the hybrid LED achieved a CIE coordinate of (0.34, 0.34) and a correlated color temperature of 5383K (Figure 4c & 4e). Figure 4.4e & 4.4f summarize the hybrid LED device's color renditions based on TM-30. A high *Rf* value of 92 is achieved, and all 99 special CFIs are larger than 80. This indicates that when illuminated by a hybrid-LED device based on the theobromine dyes, the color appearance of illuminated objects matches well with their appearances under sunlight. The slightly higher *Rg* score of 104, compared to 100 of daylight, originates from the slight oversaturation at the blue and red region, as it is observed in Figure 4.4e. Figure 4.4g shows the 99 special color fidelity indexes of a commercial specialty white LED with *Ra* of 97 and *R9* of 95. This commercial high-CRI LED uses a blue LED backlight (450 nm) and narrow-band converters. Unfortunately, due to the insufficient emission of the violet and blue wavelengths, it has lower special CFIs in both blue and

purple regions (Figure 4.4g) compared to our devices with a 405 nm backlight (Figure 4.4f). Furthermore, in the green, yellow and red regions, there are some special CFIs lower than 80, such as #5, #30, #36, and #38. This can be ascribed to the narrow emissions of inorganic phosphor components that cannot fully cover the visible spectrum. These two factors contribute to a relatively low *Rf* value of 89, highlighting the advantages of utilizing a 405 nm backlight and broad-band emitters. In addition, the *Ra* and *Rf* values in our configuration are comparable to the state-of-art values from rare-earth phosphors and perovskite quantum dots down-converted LEDs that are currently under lab development (Table 4.1). In comparison to these reported structures, our materials possess economic and environmental advantages. Notably, there is a strong red emission peak in the emission spectrum of this high-CRI LED. This is crucial to obtain *Ra* and *R9* values approaching 100, whereas it does not lead to equally high *Rf* and high special CFIs at the red region. This underlines the disadvantages of the current industry CRI standard – it possesses a skewed color space where differences in red colors are exaggerated while differences in blue colors are suppressed. [82,118]

The overall efficiency of the hybrid LED is determined by the efficiency of the backlight LED that converts electricity into blue/violet light and the efficiency of the light converter that converts blue/violet light into longer wavelengths. PLQY is used to quantify the efficiencies of light converters and is defined by the ratio of the number of photons emitted by the light converter to the number of photons absorbed by the light converter. An integrating sphere was used to measure a PLQY of 82% for the white light converter, which is contradicted by the combined PLQY contributions from Theo-Blue (~100%), Theo-Green (94%), and Theo-Ruby (39%). This can be explained by the fact that the PLQY of Theo-Ruby is highly dependent on concentration due to the heavy atom effect from Se atoms, which introduces intersystem crossing (detailed in the

following lifetime measurements) and reduces PLQY. Considering the blending ratio of Theo-Ruby in the white-light convertor is 0.05 wt%, we measured the PLQY of 0.05 wt% Theo-Ruby-SBS blend, which is 66%. It is worth mentioning that the PLQYs of Theo-Blue and Theo-Green are also reduced by this small amount of Theo-Ruby *via* the external heavy atom effect,[122] which likely limits the PLQY of the white composite to 82%. These results suggest that by changing the Theo-Blue:Theo-Green:Theo-Ruby ratio, one can adjust the blue, green, and red content in the emission spectra, thus tuning the color temperature. Because the PLQY of Theo-Blue and Theo-Green are similar, change in the Theo-Blue:Theo-Green ratio would not have a significant impact on the PLQY; however, the heavy atom effect from the Se in Theo-Ruby decreased the PLQY of the final dye-polymer composite.

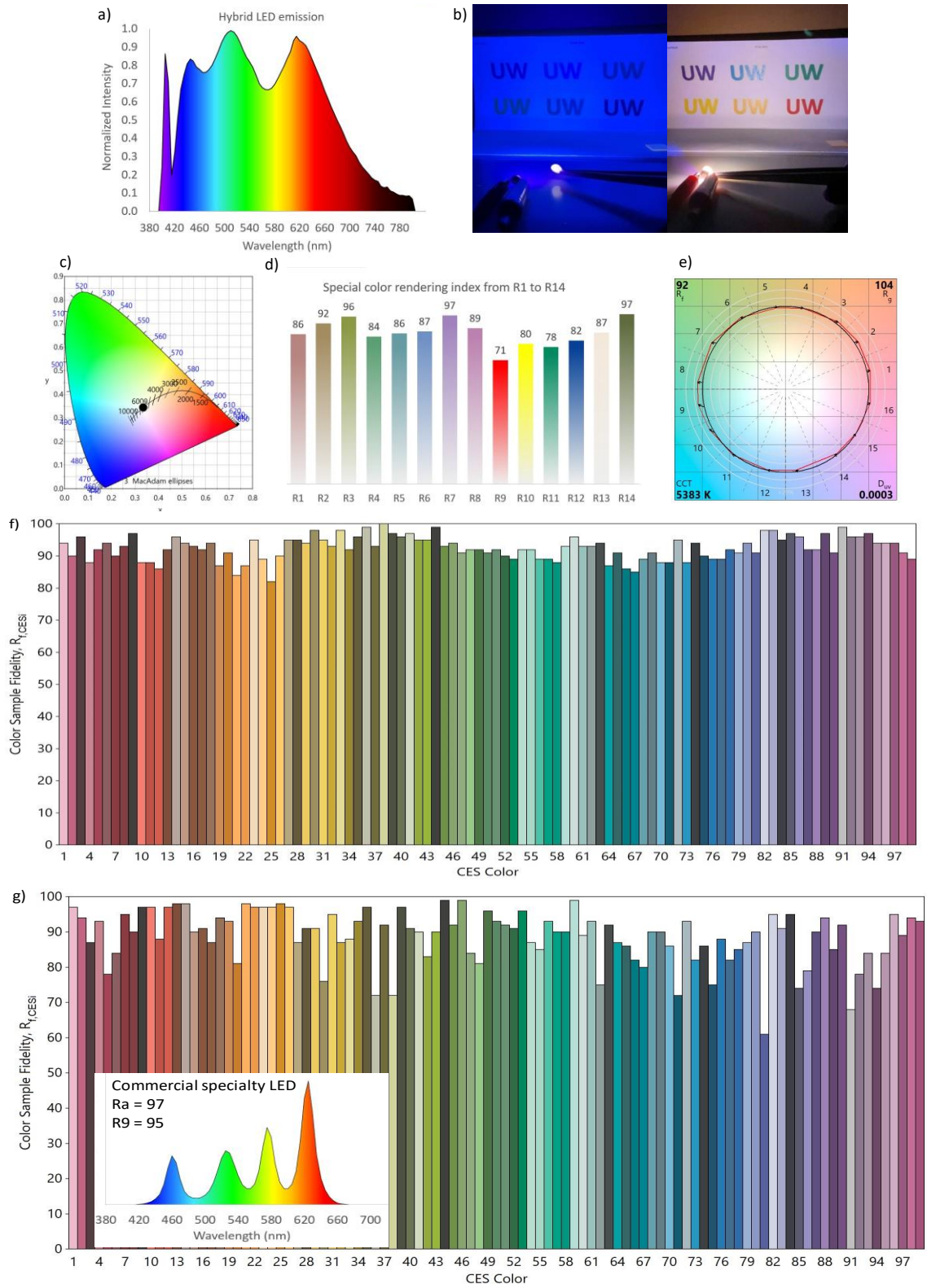

Figure 4.4. a) The emission spectrum of the hybrid LED with 405 nm blacklight and a theobromine dye SBS composite as a light converting layer; b) Photographs of a demonstration

of light-conversion; c) CIE coordinate of the emission of the hybrid device; d) 14 special CRIs of the hybrid device; e) Color distortion graph: the hybrid LED device (red line) *vs.* standard white light (black line); f) 99 special CFIs of the hybrid LED; g) 99 special CFIs of the commercial high-CRI LED.

Table 4.1. Light quality rendition of different lighting configurations and PLQYs of their light converting materials.

Category	PLQY	*Ra*	*R9*	*Rf*	*Rg*	Ref
Theobromine dyes [a)]	82%	90	87	90	104	This work
Rare-earth phosphors	N.A.	98	84	95	101	[17]
Rare-earth phosphors	N.A.	95	95	91	102	[83]
Perovskite quantum dots	61%	96	N.A.	91	99	[84]
Carbon quantum dots [a)]	63%	97	N.A.	N.A.	N.A.	[123]
Carbon quantum dots [a)]	48%	86	N.A.	N.A.	N.A.	[124]
Carbon quantum dots [a)]	41%	85.3	N.A.	N.A.	N.A.	[125]

[a)] Eco-friendly light-converters.

To better understand the origin of the lower PLQY of Theo-Ruby compared to other theobromine dyes, we conducted photoluminescence lifetime measurements on these dyes, and the results are summarized in Figure 4.5**.** To have a comprehensive understanding of the structure-PLQY relationship, Theo-Red (an analog to Theo-Ruby replacing the Se atom in Theo-Ruby to S atom) was also included. Theo-Red has a PLQY of 87% in SBS.[50] Their prompt fluorescence lifetimes (Figure 4.5a) increase in the order of Theo-Blue (1.59 ns), Theo-Green (8.55 ns), Theo-Red (14.03 ns) and Theo-Ruby (14.6 ns). According to the Einstein relation, the lifetime of prompt transition is *inversely* proportional to the oscillator strength of the transition, and proportional to the square of the emission wavelength.[126] We observed a trend in the molecular orbital simulation of Theo-Blue,[28] Theo-Green and Theo-Red[50] – the spatial overlap between their highest occupied

molecular orbitals and lowest unoccupied molecular orbitals decreases as the electron-withdrawing ability of the center unit increases (pyrene < benzo[c][1,2,5]thiadiazole < naphtho[2,3-c][1,2,5]thiadiazole). The reduced spatial overlap leads to a reduction in oscillator strength of the electronic transitions. The increasing values in emission wavelength and reducing values in oscillator strength together result in the increase of emission lifetimes in the order of Theo-Blue, Theo-Green to Theo-Red. The slightly longer lifetime of Theo-Ruby compared to Theo-Red can be explained by its slight redshift emission and small structure variation. Most of these lifetimes are monoexponential, but there is a longer lifetime component in Theo-Blue (12.85 ns) which may originate from the formation of pyrene excimers.[127]

Furthermore, in the 200 -1000 ns range of the lifetime plots (Figure 4.5b), the photon signal of Theo-Ruby is significantly stronger than those of the other theobromine dyes. The linear character of this signal on a log-log plot indicates that the lifetime decay follows a power law dependence at long times. This suggests that the long time decay of Theo-Ruby is ascribed to delayed fluorescence due to reversible trapping.[128,129] We speculate that this stems from enhanced intersystem crossing (ISC) facilitated by the presence of heavy atoms, in this case, the Se atom in Theo-Ruby.[128] Since ISC rate is proportional to Z^4,[130-132] it is likely that the ISC rate in Theo-Ruby is significantly higher than that of the other dyes. As shown in Figure 4.6, ISC converts singlet excited states into triplet excited states. Electronic transitions from triplet excited states to singlet *ground* states are usually slow and non-emissive due to spin restriction and their large energy gaps. Most of the triplet excited state electrons dissipate to the ground state through thermal decay instead of light generation, which is detrimental for high PLQYs. However, the energy offset between triplet excited states and singlet excited states is smaller. This smaller energy gap allows reversed ISC, back-converting non-emissive triplets to emissive singlets and enabling

delayed fluorescence. Notably, both ISC and reversed ISC are still spin restricted, and they have much smaller kinetic rates compared to fluorescence, which is associated with transitions between singlet states. Therefore, we observed delayed fluorescence in smaller intensity and at longer lifetime ranges. These lifetime experiments demonstrate that the introduction of heavy atoms facilities non-radiative decay of theobromine dyes *via* ISC, which is a valuable insight for future development of theobromine dyes.

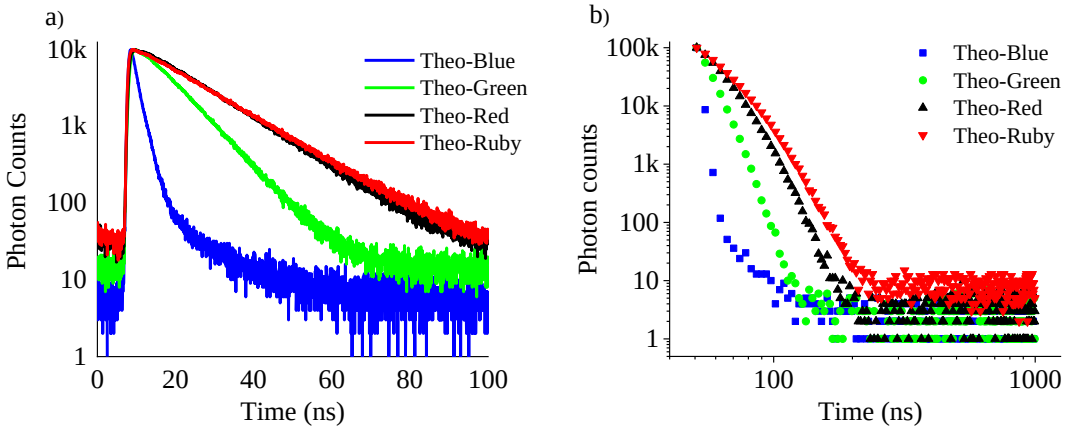

Figure 4.5. PL decay curves of theobromine dyes measured in an inert atmosphere with 405 nm excitation: a) short time range; b) long time range plotted on log axes.

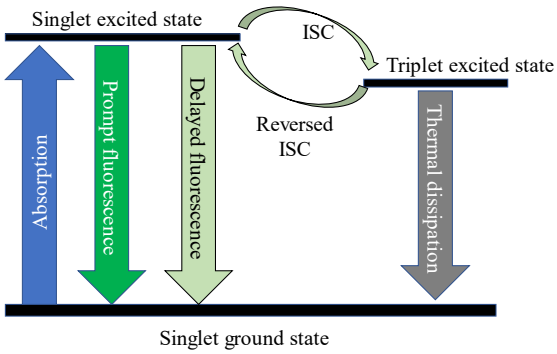

Figure 4.6. Energy level diagram to illustrate the interplay between singlet and triplet excited states *via* ISC and the resulting difference in prompt fluorescence (strong green) and delayed fluorescence (light green).

4.4 CONCLUSION

In this paper, we developed a hybrid LED structure utilizing three organic dyes (Theo-Blue, Theo-Green and Theo-Ruby) synthesized from an abundant and non-toxic natural product (theobromine) with a 405 nm LED backlight. These three dyes possess broad emission and along with a 405 nm LED backlight, the resultant hybrid LED generates a continuous emission profile covering wavelengths from 400 – 740 nm (94% of human visible wavelengths). This emission yields excellent color rendition values, *Ra* of 90 and *Rf* of 92, which rival existing common LEDs and specialty LEDs in the market that are based on REE phosphors. In addition, the light-converting composite is made from 99 wt% SBS, an inexpensive industrial polymer, and 1wt% theobromine dyes, reducing the cost of light-converter to ¢ 1.30 for a 1 W LED. This is significantly lower than the current cost of rare-earth phosphors (¢ 19.2). The PLQY of the dye-SBS composite is 82%, resulting from the combined contributions from Theo-Blue (~100%), Theo-Green (94%) and Theo-Ruby (66%). Their excited state kinetics shows that the reduced PLQY of Theo-Ruby stems from increased ISC due to the presence of selenium atom in the structure, providing guidance for future optimization of high-performance red theobromine dyes.

Chapter 5. MODULAR ZWITTERION-FUNCTIONALIZED POLY(ISOPROPYL METHACRYLATE) POLYMERS FOR HOSTING LUMINESCENT LEAD-HALIDE PEROVSKITE NANOCRYSTALS

(This chapter is adapted from a paper published by Yunping Huang during this Ph.D program)[107]

5.1 INTRODUCTION

Nanocrystal emitters possess narrow band emission, which is complementary to organic phosphors in optical engineering applications. Lead halide perovskite nanocrystals (NCs) have gained substantial research interest and advanced significantly in the past decade owing to their excellent optoelectronic properties and being solution processable – the former factor enhances high device performance while the latter reduces the cost and difficulties in device fabrication. Perovskite NCs have been successfully implemented light emitting diodes, lasers, spintronics and luminescence solar concentrators, and obtained distinguished performance. However, to bridge the gap between laboratory research and commercial application, the stability of lead halide perovskite NCs needs to be substantially improved, ideally without trade-offs in optoelectronic properties and processabilities.

Lead-halide perovskite NCs have been heavily investigated for their intriguing properties,[133-137] including broad spectral tunability with anion[138-140] and cation[141-145] replacement, unique electronic structure,[146-148] and high defect tolerance.[149-152] These properties have made such NCs a popular emitter for application in light-emitting diodes (LEDs),[23,153] lasers,[154-157] single-photon sources,[158-160] and luminescent solar concentrators.[161-164] Unfortunately, these NCs are sensitive to degradation in the presence of oxygen and water.[165,166] To bridge the gap between laboratory research and commercial application, NC stability needs to be improved without sacrificing optoelectronic properties or processability. Furthermore, the broad range of potential

applications means that different functional polymer matrices may be required for different uses. For instance, whereas as-synthesized NCs can be supported in various apolar polymers,[161,167-171] some applications require that NCs are suspended in silicone,[23,172-174] aqueous,[175] fluorinated,[163,176-178] or semiconducting[179-181] matrices to enable the desired functionalities. Because these host matrices have limited chemical compatibility with the aliphatic ligands often used to stabilize perovskite NCs, additional interface modifiers must be introduced to improve compatibility between the native NC surface ligands and the polymer. Alternatively, these ligands must be replaced with novel ligands tailored to be compatible with the host polymer of interest.

The interface modifier approach has been demonstrated by direct synthesis of perovskite NCs in a hydrophobically stabilized micelle of lauryl methacrylate[171] and by using custom polymers that form micelles to stabilize the NCs in different hosts,[175,182-185] with varying levels of success. Novel-ligand approaches have mostly focused on ammonium,[23,92,179,180,186,187] carboxylate,[188] and poly(vinylidene difluoride)[153,189] NC coordination. These binding groups have limited affinity for perovskite NC surfaces,[190] however, and some are consumed during subsequent polymerization reactions in making the NC/polymer composites.[191] Consequently, most of these polymer-suspension protocols yield samples with poor dispersion and reduced NC photoluminescence quantum yields (PLQYs). Alternatively, strongly binding phosphonate,[192-196] sulfonate,[150] and zwitterionic[197,198] ligands have recently been used to synthesize perovskite NCs with improved PLQYs and stability. The covalently tethered positive and negative ions on zwitterionic ligands are well matched to the highly ionic surface of the NCs. These ligands are mostly aliphatic, however, which limits their ability to solvate NCs in many non-aliphatic functional polymers, complicating device fabrication and ultimately limiting the application range of perovskite NCs. Zwitterionic polymers have been used to passivate perovskite thin films,[199,200] and while this

manuscript was in preparation, zwitterionic polymers were reported to stabilize $CsPbBr_3$ NCs in solution and solid state.[201,202] These works solidify the idea that zwitterionic polymers have high potential as perovskite NC host matrices.

Here, we describe a set of modular zwitterion-functionalized poly(isopropyl methacrylate) polymers developed to match the specific needs of various colloidal lead-halide perovskite NCs. In general, polymers with appended alkyl chains have high solubility in organic solvents,[203-205] but branched alkyl structures can also improve polymer solubility in green solvents that are sufficiently apolar to prevent NC degradation[206] and inhibit the formation of crystalline scattering structures in a solid composite.[207,208] Consequently, isopropyl methacrylate was used instead of commonly used long-chain alkyl acrylates; the increased solubility from the isopropyl side chain facilitates solution processing with green solvents such as butyl acetate that are still sufficiently apolar to prevent NC degradation. Within these polymers, the distances between positive quaternary ammonium moieties and negative sulfonate moieties are tuned using either 3- or 4-methylene spacers. This tunability allows the zwitterion separation to be matched with the relevant NC lattice spacings when the NC anions are changed from Cl^-/Br^- to I^-.[198] We show that the native NC ligands are easily replaced by these zwitterionic polymers, and the resulting polymers are shown to stabilize lead-halide perovskite NCs across the entire composition and luminescence-color range. For Yb^{3+}-doped NCs with near-infrared emission, we further utilize a fluorinated version of poly(isopropyl methacrylate) that reduces absorption from C–H vibrational overtones at Yb^{3+} emission at infrared wavelengths.[163,209] The modularity of these polymers provides access to a variety of perovskite NC/polymer composites with attractive solution processability, optical properties, and long-term stability, making these polymers appealing hosts for use of colloidal lead-halide perovskite NCs in various photonic applications.

5.2 MATERIALS SYNTHESIS AND PROCESSING

Amine precursor polymer syntheses. The polymer synthesis process is outlined in Scheme 1. 2-(Dimethylamino)ethyl acrylate (143 mg, 1 mmol) and either isopropyl methacrylate (1152 mg, 9 mmol) or 1,1,1,3,3,3-hexafluoroisopropyl methacrylate (2124 mg, 9 mmol) was added to a vial that was pre-dried overnight in a 120 °C oven. 2,2'-azobis(2-methylpropionitrile) (8 mg, 0.5 mmol) and *tert*-nonyl mercaptan (8 μL, 0.5 mmol) – a chain transfer agent to reduce molecular weight[191] – were added subsequently. The vial was then degassed and sealed. The reaction was heated at 60 °C for one day, and at 80 °C for another two days. After cooling down to room temperature, 2 mL of THF was added to dissolve the polymer, followed by precipitation with 50 mL of deionized water. The precipitate was later washed with methanol and dried under vacuum overnight.

Zwitterion-functionalized polymer syntheses. Amine precursor polymer (400 mg, 0.18-0.30 mmol of amine group depending on the polymer) was dissolved in 8 mL THF and heated to 60 °C. After 30 min, an excess of sultone (1,4-butanesultone (400 mg, 2.94 mmol) or 1,3-propanesultone (400 mg, 3.28 mmol)) was added dropwise. 3 mL of methanol was added after 1 hour and another 3 mL of methanol was added after 24 hrs. The reaction was further heated at 60 °C for another day before cooling down to room temperature. The solution was transferred into a dialysis tube (molecular weight cut-off = 1000) and stirred in 1000 mL of methanol for 2 hrs and 1000 mL ethyl acetate for an additional 2 hrs. After dialysis, the solution inside the dialysis tube was transferred to a round-bottom flask and concentrated under vacuum. Clear transparent solids were obtained and dried under vacuum to remove residual solvents. The zwitterionic polymers are soluble in most common organic solvents, including green organic solvents such as ethyl and butyl

acetate[210] that are common antisolvents for perovskite NC purification.[133,135,198] ^{1}H-NMR spectra of the polymers synthesized here are provided in the Supporting Information.

General aspects of NC/polymer composite film preparation. Glass substrates were cut and sonicated for 15 min sequentially in deionized water with 2% detergent, deionized water, acetone, and 2-propanol; after which each substrate was dried with compressed air. To transfer perovskite NCs into a zwitterionic polymer matrix, the desired quantities of polymer were added to 0.75 mL of ethyl acetate in a N_2-filled glovebox and stirred overnight. Then, a small volume of NC solution in hexanes was added to the solution of zwitterionic polymer in ethyl acetate. NC concentrations were determined using literature perovskite NC extinction coefficients,[190] and the volume of NC solution added was determined such that the equivalents (Eq) of zwitterionic groups per NC was kept between 10 and 300 kEq. This solution was then removed from the glovebox and sonicated for 5 min. The resulting NC/zwitterionic polymer composites were precipitated out of solution by adding an excess of hexanes and centrifuging the resulting turbid solution at 1318 gx for 10 min. Very few NCs remained in the resulting supernatant, indicating that the native aliphatic ligands were successfully exchanged for the zwitterionic polymer ligands. This final pellet was then dispersed in 0.5 mL of butyl acetate. To investigate the effect of aggregates on the observed PL red shifts, we diluted a representative solution of $CsPbBr_3$ NC/ZP3 composite by a factor of 50 with butyl acetate and drop cast an aliquot of this solution and all subsequent solutions onto clean glass substrates. After casting the first film, the remaining dilute NC/ZP3 solution was centrifuged at 16,060 gx for 10 minutes and the precipitate was discarded. Finally, the remaining centrifuged solution was filtered through a 0.22 μm PTFE syringe filter. This process yielded a total of three solid samples for future characterization.

5.3 RESULT AND DISCUSSION

5.3.1 *Preparation of zwitterion-functionalized polymers.*

Scheme 5.1 summarizes the approach used to synthesize modular zwitterion-functionalized polymers. We used 2,2'-azobis(2-methylpropionitrile) (AIBN) to initiate the radical copolymerization of two commercial acrylate monomers, 2-(dimethylamino)ethyl acrylate and isopropyl methacrylate (or fluorinated isopropyl methacrylate) in a 1:9 ratio, to obtain amine-precursor polymers. This approach allows adaptation for many other functional groups simply by replacing isopropyl methacrylate with other acrylate or methacrylate monomers. Thiol, a chain transfer agent, was added to the polymerization reaction to prevent formation of high-molecular-weight polymers with reduced solubility. These amine-precursor polymers were then reacted with the corresponding sultones to yield the desired zwitterion-functionalized polymers. This flexible chemistry allows integration of zwitterions with different anion-cation separations (3 or 4 methylene spacers). For this work, we successfully synthesized 3-carbon-separated zwitterion-functionalized polymers (ZP3) and their fluorinated analogs (ZFP3), as well as 4-carbon-separated zwitterion-functionalized polymers (ZP4) and their fluorinated analogs (ZFP4). ^{1}H-nuclear magnetic resonance (NMR) spectra of all four polymers are provided in the Supporting Information. According to NMR signals (Figure 5.1 – 5.4), these four polymers have similar values of degree of polymerization (DP) and molecular weight (MW) – DP around 10 and MW around 2 kDa, which are anticipated considering 0.05 *eq*. of radical initiator and 0.05 *eq*. of chain transfer agent were added in the polymerization reaction to limit the formation of high-MW polymers (see details in experimental procedures). We observed that the chemical structures of the polymers have big impacts on their solubility – the non-fluorinated polymers have good solubility in most organic

solvents except hexane, while the fluorinated polymers are less soluble in aprotic solvents.

Three of these polymers were then used for hosting three different categories of perovskite NCs, as summarized in Table 1: undoped NCs with small lattice parameters (*e.g.*, $CsPbBr_3$ NCs), large lattice parameters (*e.g.*, $CsPbI_3$ NCs), and doped NCs showing NIR emission (*e.g.*, Yb^{3+}:$CsPbCl_3$ NCs).

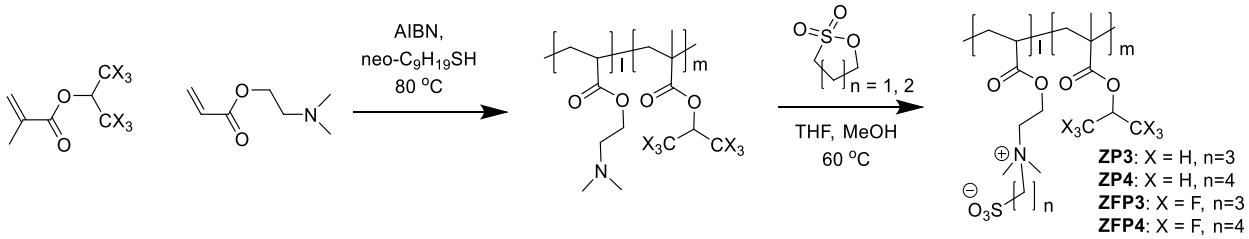

Scheme 5.1. Summary of the synthesis of a series of zwitterion-functionalized polymers. The ratio l:m is 1:9 for all polymers reported here.

Table 5.1. Summary of the zwitterionic polymers developed in this work and the perovskite NC/polymer composites prepared from each. The fluorinated polymer with 4-carbon zwitterion spacing was successfully synthesized but was not soluble in ethyl acetate.

Abbreviation	Zwitterion separation	Fluorinated	NCs used	Amt. ZP used per 3 pico-mol NC
ZP3	3 carbons	No	$CsPbBr_3$	77 mg
ZP4	4 carbons	No	$CsPbI_3$, $CsPb(Br_{1-x}I_x)_3$	7 mg
ZFP3	3 carbons	Yes	$CsPbBr_3$, Yb^{3+}:$CsPbCl_3$	120 mg

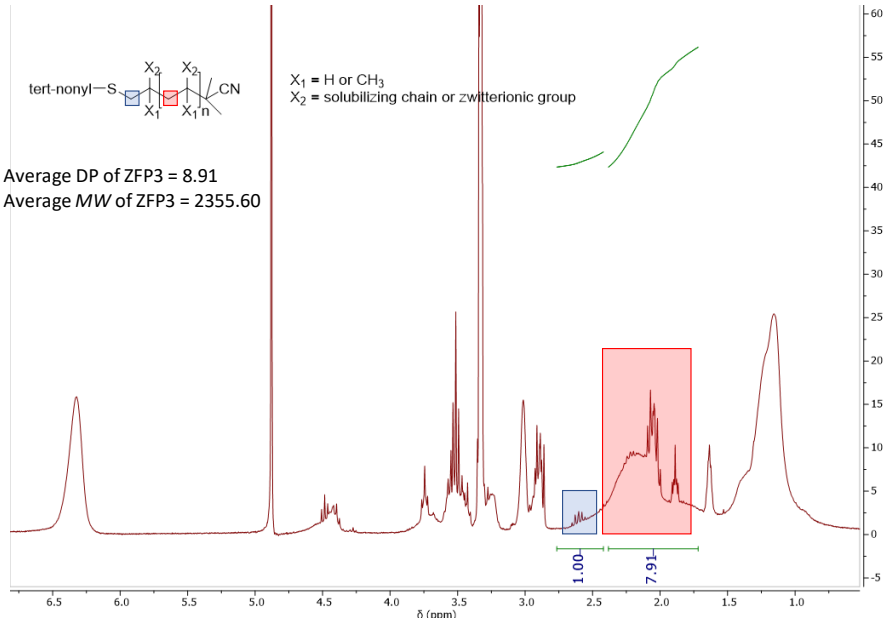

Figure 5.1. NMR spectrum of ZFP3 in methanol-d_4 measured at room temperature. NMR peaks used to calculate degree of polymerization (DP) and molecular weight (MW) are highlighted.

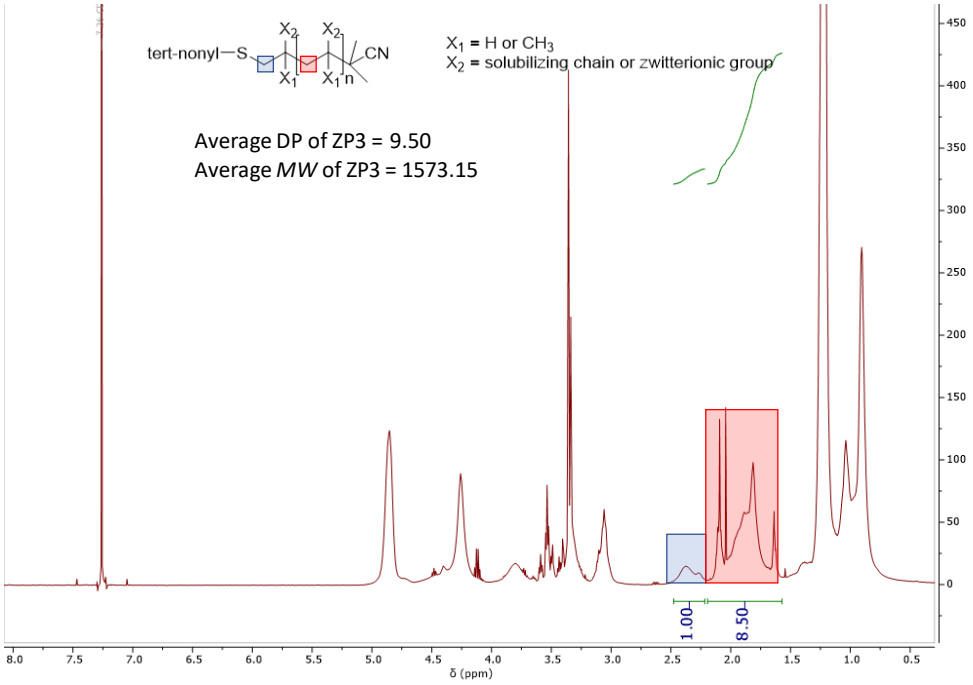

Figure 5.2. NMR spectrum of ZP3 in chloroform-d measured at room temperature. NMR peaks used to calculate degree of polymerization (DP) and molecular weight (MW) are highlighted.

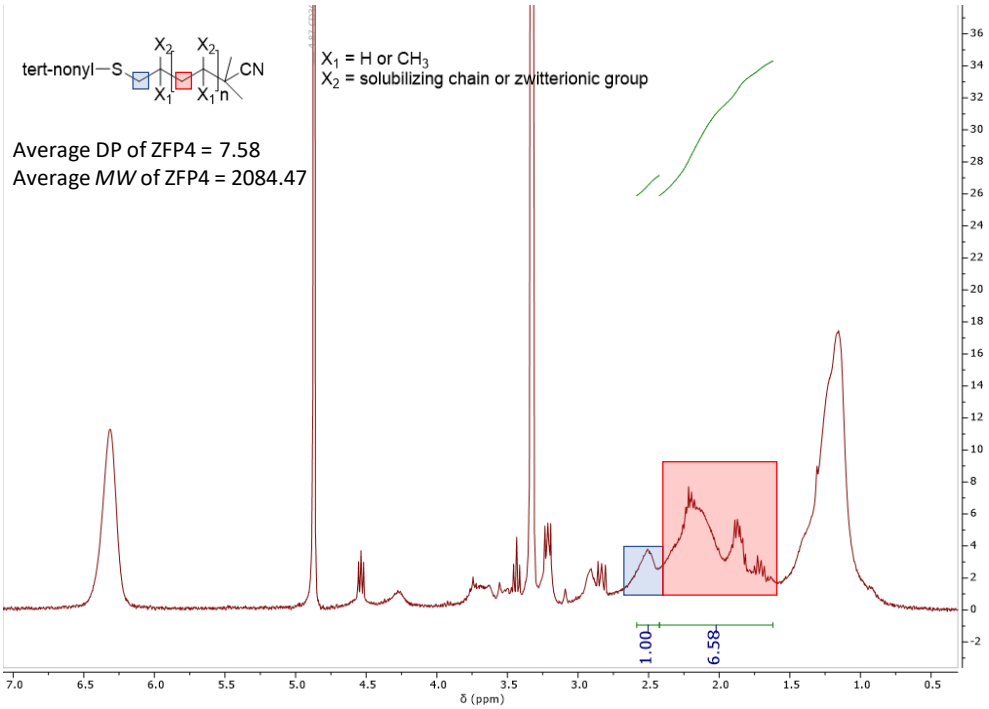

Figure 5.3. NMR spectrum of ZFP4 in methanol-d_4 measured at room temperature. NMR peaks used to calculate degree of polymerization (DP) and molecular weight (MW) are highlighted. This polymer was not used in this work because it was not soluble in ethyl or butyl acetate.

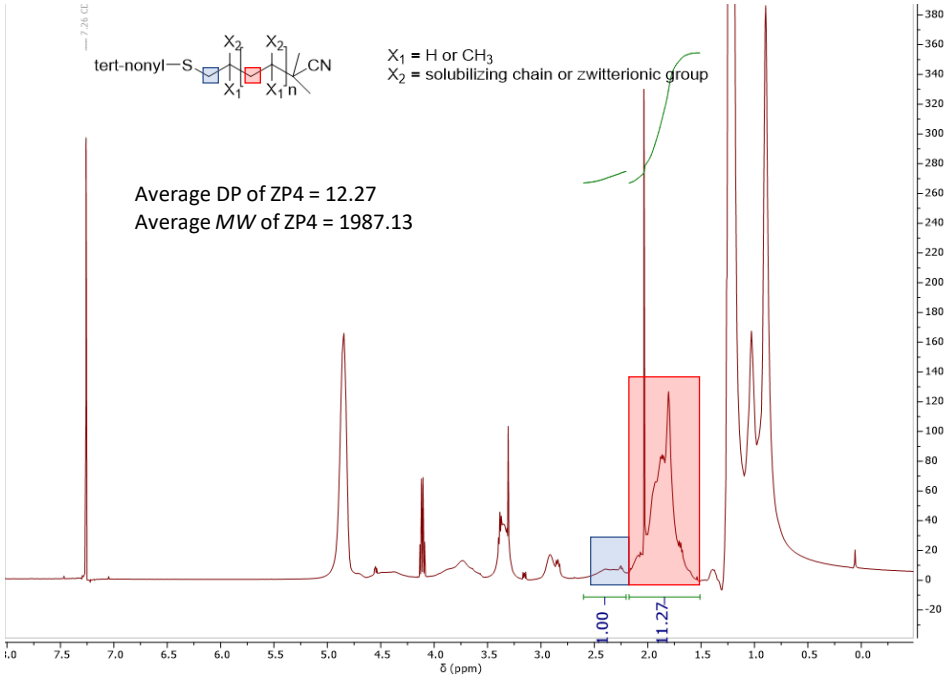

Figure 5.4. NMR spectrum of ZP4 in chloroform-d measured at room temperature. NMR peaks used to calculate degree of polymerization (DP) and molecular weight (MW) are highlighted.

5.3.2 *$CsPbBr_3$ NC/polymer composites.*

Figure 5.5a shows ^{1}H-NMR spectra of ZP3 before and after the $CsPbBr_3$ NC ligand exchange from native ligands to zwitterionic polymers. There is no signal at 5.5-6.0 ppm attributing to the C=C bond of OA or OAm in the pre-ligand-exchanged sample.[138] This result indicates that the original NC ligands are fully removed in the ligand exchange. In the ligand-exchanged sample, we do notice a singlet centered at 0.12 ppm, which is assigned to TMS-acetate,[211] indicating incomplete removal of acetate groups during NC preparation. No signals from TMS-Br (0.36 ppm) or TMS-sulfonate (0.40 ppm, the product after TMS-Br reacts with sulfonate groups) were detected. This result indicates that the TMS-halide precursors were all consumed during synthesis and converted to TMS-acetate, a molecule that is likely a spectator in subsequent procedures. NMR signals associated with the polymer backbone appear between 0.7 and 2.5 ppm. The additional peaks between 2.7 and 5.2 ppm are assigned according to the color-coded diagram in the inset of Figure 1a. Most NMR peaks remain essentially unchanged upon NC addition, but the reduced electron density of the sulfonate anion upon association with NC surface cations leads to a shift of the adjacent methylene protons from 2.93 to 3.05 ppm (highlighted magenta).[212-216] For the quaternary ammonium ion, the NMR data show that only one methylene group is closely associated with the NC surfaces (highlighted green), while the other methyl/methylenes are not. The NMR signal of the H atoms on this closely interacting methylene group have the highest frequency of all the methyl/methylene groups on the quaternary ammonium ion. This result indicates that those H atoms have the lowest electron density and thus are more likely to interact with halide anions of the NC surfaces. These NC polymer composites were soluble in butyl acetate, a green solvent that is a common antisolvent for perovskite NCs.[210] Furthermore, the solution-state NC PLQY in a given zwitterionic polymer did not increase as the NC concentration was increased

(see Supporting Information), indicating that the zwitterionic polymers are strongly bound to the NCs.[150,195] The NCs in a zwitterionic polymer solution had a maximum PLQY of 84 ± 5% compared with 59 ± 5% for the same as-synthesized NCs, indicating that surface defects are effectively passivated by the zwitterions on these polymers.

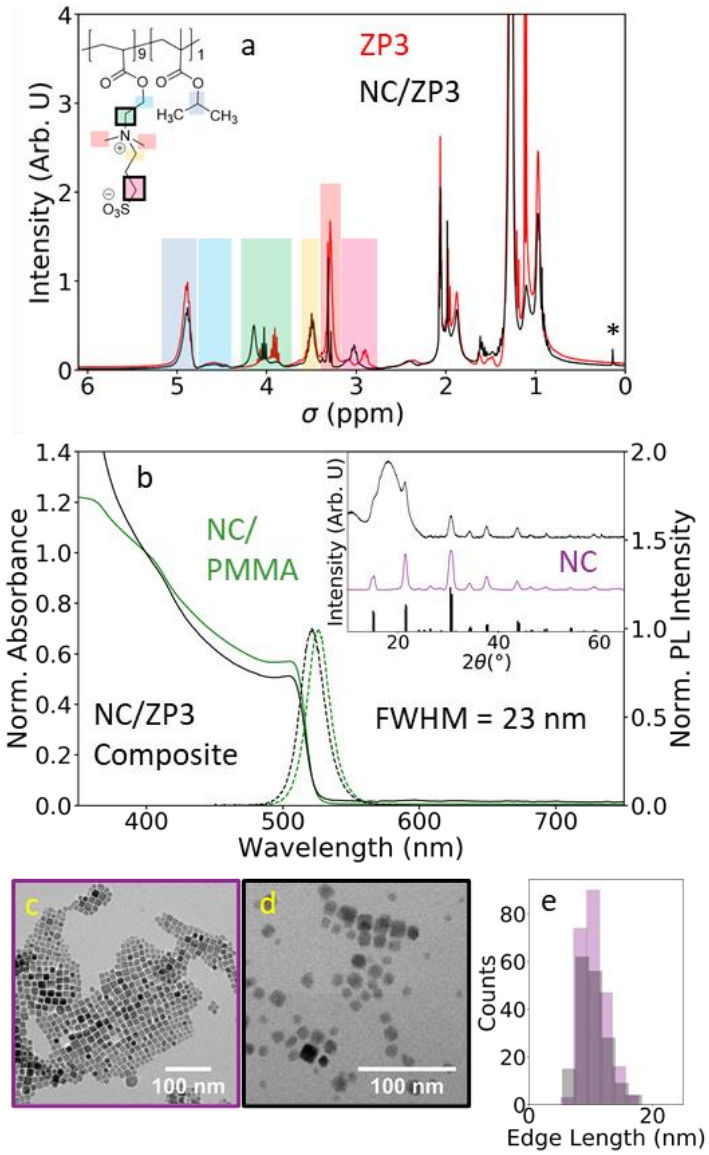

Figure 5.5. (a) ^{1}H-NMR spectra of ZP3 in acetone-d_6 before and after binding to $CsPbBr_3$ NCs. The peaks around 3 and 4 ppm are substantially shifted after NC binding, indicating that the protons associated with these peaks (bolded boxes) are confined near NC surfaces. * indicates the peak associated with TMS-acetate. (b) Absorption and PL spectra of $CsPbBr_3$

NC/polymer composites drop cast from a solution of NCs and ZP3 in butyl acetate and a solution of NCs and PMMA in toluene. Absorption spectra are normalized at 400 nm and PL spectra are normalized to the PL maximum. The PMMA sample was cast in a N_2-filled glovebox to maximize PLQY. *Inset*: XRD data collected before and after transfer of NCs to ZP3. The broad peaks from ~10 to ~17° are attributed to scattering by the amorphous polymer. TEM images of $CsPbBr_3$ NCs (c) drop cast from hexanes solution and (d) drop cast from a solution of NC/ZP3 composite in butyl acetate. (e) Histogram of edge lengths from the TEM images shown in panel c.

Once purified, the $CsPbBr_3$ NC/ZP3 solution was drop cast onto clean glass slides to form composite thin films. Figure 1b shows absorption and photoluminescence (PL) spectra of $CsPbBr_3$ NCs in a ZP3 film and, for comparison, the same NCs in a high-molecular-weight poly(methyl methacrylate) (PMMA) composite (see Supporting Information). Apart from small reabsorption- and aggregation-induced shifts in the PL (see Supporting Information), the UV/vis and PL spectra are nearly unchanged after the NCs are transferred into a ZP3 composite and the full width at half-maximum (FWHM) of the NC PL is sufficiently small for applications in LEDs with precise green color rendering.[217] The NC/ZP3 composite has no detectable sub-bandgap scattering, indicating that it has few NC aggregates.[218]

The inset of Figure 5.5b shows X-ray diffraction (XRD) data collected from as-synthesized $CsPbBr_3$ NCs and the same NCs in a ZP3 composite. Apart from additional amorphous scattering signals, the diffraction peaks are the same for both samples. Because each peak in the XRD consists of multiple Bragg reflections derived from the orthorhombic $CsPbBr_3$ crystal structure, we could not perform a precise Scherrer analysis. That said, although the XRD FWHM for the NC diffraction peak at 44° increases by ~0.006° (0.7%) in the ZP3 composite, this difference is likely within experimental uncertainty. Furthermore, the transmission electron microscope (TEM) images in Figure 5.5c,d show that the $CsPbBr_3$ NCs maintain their cube-like shapes in a ZP3

composite. The dark spots in both images are attributed to Pb^0 nanoparticles formed during TEM imaging. Figure 1e plots histograms of nanocrystal edge lengths taken from the images in Figure 5.5c,d and Figure S9. The average NC edge lengths before and after binding by ZP3 are 10.6 ± 2.1 nm and 10.4 ± 2.4 nm, respectively. Importantly, the solid-state PLQYs of the $CsPbBr_3$ NCs in PMMA and ZP3 composites were measured to be 55 ± 5% and 90 ± 5%, respectively. These PLQYs suggest that non-radiative recombination sites are effectively passivated when the NCs are transferred into ZP3.

The stabilities of the NC composites were assessed in ambient atmosphere both in the dark and under illumination. In initial experiments, we note that $CsPbBr_3$ NC/zwitterionic polymer solutions in butyl acetate stored in ambient conditions maintained ~95% of their initial PLQY after 5 months of dark storage (see Supporting Information), whereas as-synthesized NCs in hexanes generally precipitate from solution after several days of ambient dark storage. To understand how these observations might translate to solid-state samples, we performed systematic stability measurements on various solid composites. To probe the PL stability of these NC composites, Figure 5.6a plots PLQYs of solid $CsPbBr_3$ NC/ZP3 and NC/PMMA composites measured as a function of ambient dark storage time. The NCs showed similar long-term dark storage stability in ZP3 as in PMMA, but the PLQY of the NC/ZP3 composite was ~2 times greater, indicating the efficacy of these zwitterionic polymers as a ligating matrix. XRD data (Supporting Information, Figure S11) show that $CsPbBr_3$ NCs in solid zwitterionic polymer composites maintain their crystal structure after 9 months of dark storage and PLQY data show that the PL is preserved after 1 year of dark storage. Both results are indications of the resilience of these NCs in zwitterionic polymer composites.

Figure 5.6b plots PLQYs of various NC/polymer composites measured as a function of

illumination time under ambient atmosphere, using ~90 mW cm^{-2} of full-area, 450 nm irradiation. The NC/ZP3 sample loses about 20% of its absolute PLQY in the first 12 hrs of illumination, but the NC PL intensity remains constant through the remaining 75 hrs of the experiment. Furthermore, the PLQYs of the NC/ZP3 samples recover over multiple time scales. For example, Figure S13 shows an initial PLQY loss (5-10 sec) that fully recovers after ~10 min of dark storage, and Figure 2b shows that both the rapid PLQY loss and the slower PLQY decrease (~12 hrs) recover to ~90% of the initial PLQY after 6 days of dark storage. In contrast, the NC/PMMA sample loses almost all of its PLQY after 24 hrs of irradiation, and this PLQY does not recover with dark storage. This result is consistent with the observation that perovskite NC/PMMA composites cannot withstand the high fluences (>100 W cm^{-2}) of single-particle spectroscopic measurements in ambient conditions.[219] Most reports of related NC/polymer composites do not perform irradiation stability measurements on the timescale needed to observe the rapid PLQY loss observed in Figure S13, so it is unclear whether this drop is even more general among perovskite NCs.

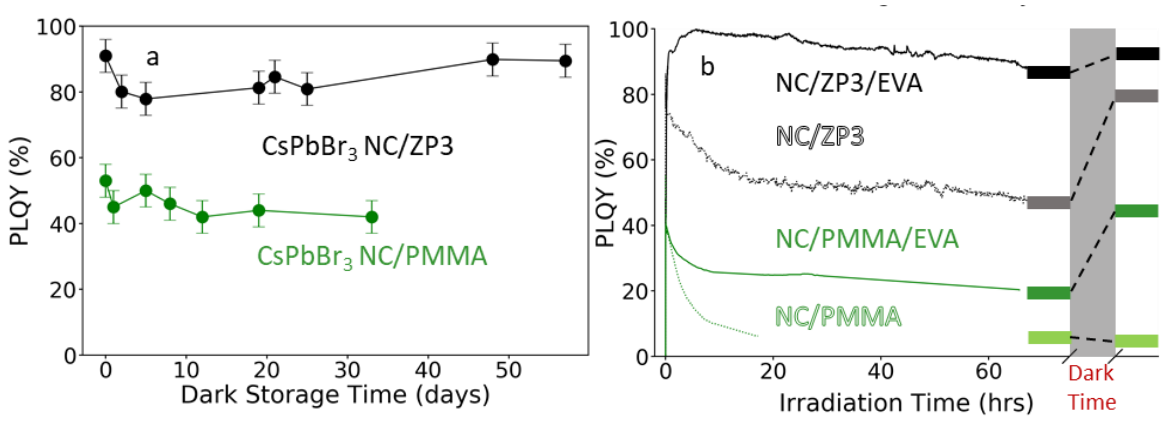

Figure 5.6. (a) PLQYs as a function of dark storage time under ambient atmosphere for drop-cast $CsPbBr_3$ NCs in PMMA and ZP3 composites. The NCs in ZP3 preserve all their original

PLQY over 2 months while NCs in PMMA lose 20% of their PLQY over the first 15 days of dark storage. (b) PLQYs plotted as a function of 450 nm irradiation time for $CsPbBr_3$ NC/ZP3 and NC/PMMA composites with and without EVA encapsulation. The PLQYs were measured again after each sample was stored in the dark for several days following the irradiation experiment, and the values measured before and after dark storage are indicated as horizontal bars.

To better evaluate the potential of these NC/polymer composite in commercial applications, we laminated $CsPbBr_3$ NC/ZP3 and NC/PMMA samples between two layers of glass with poly(ethylene-*co*-vinyl acetate) (EVA) to reduce exposure of the NCs to air. Remarkably, the PLQY of the EVA-laminated NC/ZP3 sample increases to nearly 100% within the first few hours of illumination and stays constant at this value for the remaining 75 hrs of the experiment. *Ex situ* integrating-sphere measurements verify that after 75 hrs of irradiation, the PLQY of the EVA-laminated sample increased from 48 ± 5% to 93 ± 5%; this PLQY is among the highest reported to date for any inorganic or hybrid bromo-perovskite NC/polymer solids.[153,182,188,220] We also note that the PL spectra of both samples do not change substantially over the course of this measurement (see Supporting Information), suggesting that this photo-brightening is not attributable to irreversible etching of the NCs.[158,168] In contrast, the PLQY of the EVA-laminated NC/PMMA sample decreased under illumination, recovering again after dark storage. These irradiation results indicate that the photostability of $CsPbBr_3$ NCs can be substantially enhanced by limiting air exposure. Additionally, when these NCs are hosted in a ZP3 composite, the high density of zwitterionic passivating groups in this polymer improves photostability in ambient conditions and increases PLQY in inert conditions relative to the same NCs in PMMA.

5.3.3 *$CsPbI_3$ NC/polymer composites.*

We now turn our attention to polymer composites that stabilize red-emitting $CsPbI_3$ NCs. The $CsPbI_3$ NCs were found to be noticeably less stable than $CsPbBr_3$ NCs upon mixing with the zwitterionic polymers. Although $CsPbBr_3$ NC/ZP3 composites in butyl acetate were stable under ambient conditions for up to 5 months, $CsPbI_3$ NC/ZP4 composites in butyl acetate were only stable for ~24 hrs in similar storage conditions.

Fortunately, the $CsPbI_3$ NCs in ZP4 show significantly improved PL compared to the same NCs either drop cast without polymer or embedded in PMMA composites. Figure 5.7a plots absorption and PL spectra of a $CsPbI_3$ NC/ZP4 composite and, for comparison, also of a $CsPbI_3$ NC/PMMA composite. The absorption and PL spectra for NCs in ZP4 and PMMA are nearly identical, apart from greater sub-bandgap scattering and a slight PL blue shift in the NC/ZP4 sample. The PL decay of the NCs in ZP4 is nearly monoexponential, whereas that of the NCs in PMMA appears biexponential (Figure 5.7c). The PLQYs of the NCs in ZP4 and PMMA composites are 85 ± 5% and 45 ± 5%, respectively, suggesting that the additional PL decay component of the NCs in a PMMA composite can be attributed to non-radiative recombination at non-passivated surface traps.

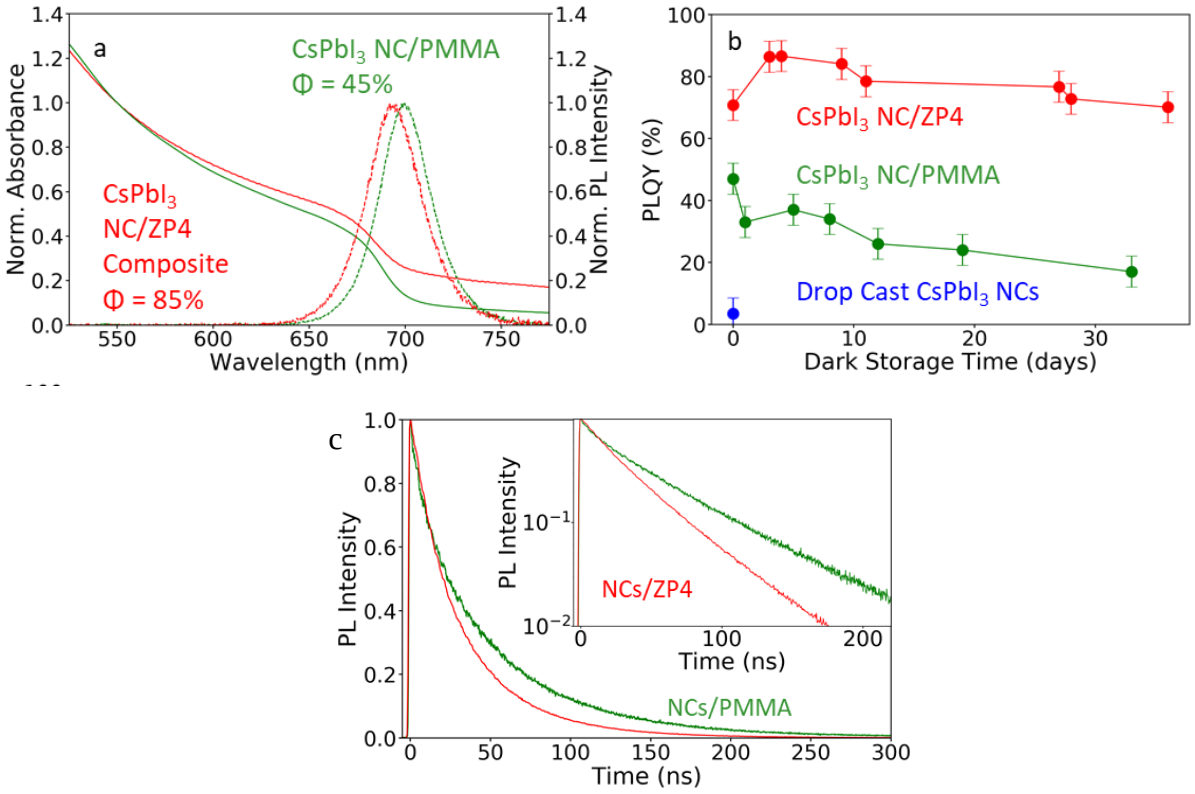

Figure 5.7 (a) Absorption and PL spectra of $CsPbI_3$ NCs in ZP4 and PMMA composites. Absorption spectra are normalized at 550 nm and PL spectra are normalized to the PL maximum. The PLQYs of these samples are also indicated. (b) $CsPbI_3$ NC PLQYs plotted as a function of dark storage time in ambient atmosphere, measured for $CsPbI_3$ NC/ZP4 and NC/PMMA composites and the same NCs drop cast from hexane solution. (c) PL decay curves measured in ambient conditions with 405 nm excitation for CsPbI3 NCs in ZP4 and PMMA composites shown in Figure 3 of the main text, normalized at t = 0. Inset: PL decay curves plotted on a log scale.

Figure 5.7b plots PLQYs of $CsPbI_3$ NCs drop cast onto a glass substrate along with $CsPbI_3$ NC/ZP4 and $CsPbI_3$ NC/PMMA composites, measured as a function of dark storage time under ambient atmosphere. The drop-cast $CsPbI_3$ NCs degraded almost as soon as they were exposed to air, and the NCs in PMMA lost two thirds of their PLQY over the course of ~32 days, dropping to 18 ± 5%. In contrast, the NCs in ZP4 maintain their PLQY well over the entire 36-day experiment,

indicating improved long-term stability of $CsPbI_3$ NCs embedded within the ZP4 polymer matrix. Furthermore, NC/ZP4 composites recover most of their PLQY after dark storage time, while the PLQY of the NC/PMMA composites remain low after dark storage time. These observations demonstrate that, like the $CsPbBr_3$ NC/ZP3 composites, $CsPbI_3$ NCs in ZP4 show *reversible* PL degradation when irradiated in the presence of air whereas the same NCs in PMMA show irreversible PL degradation.

5.3.4 *Yb^{3+}-doped $CsPbCl_3$ NC/polymer composites.*

Figure 5.8a shows the absorption spectrum of Yb^{3+}:$CsPbCl_3$ NCs in a ZFP3 composite thin film. The corresponding fluorinated polymer without zwitterions is insoluble in the apolar solvents used to process as-synthesized NCs. When zwitterionic groups are added, however, the zwitterionic fluorinated polymer is soluble in butyl acetate and can be used to stabilize as-synthesized Yb^{3+}:$CsPbCl_3$ NCs *via* the ligand exchange procedure described here. The absorption spectrum of the NC/ZFP3 film shows minimal sub-bandgap scattering, indicating that high concentrations of NCs can be well dispersed in ZFP3. The inset to Figure 5.8a shows a TEM image of the Yb^{3+}:$CsPbCl_3$ NCs in ZFP3. This image shows that the NC structure is similar to those reported previously for colloidal Yb^{3+}:$CsPbCl_3$ NCs.[141] Figure 5.8b plots PL spectra of zwitterionic ligand-capped Yb^{3+}:$CsPbCl_3$ NCs drop cast from solution and of oleylamine-capped NCs after incorporation into a ZFP3 composite, measured such that relative intensities can be compared quantitatively. The PLQY of the NC/ZFP3 film is slightly greater than that of drop-cast NCs, owing to effective surface passivation by zwitterions in ZFP3. Additionally, the NC/ZFP3 film retains nearly the same PLQY for over 1.8 years of dark storage, an indication that the Yb^{3+}:$CsPbCl_3$ NCs are highly stable in this polymer.

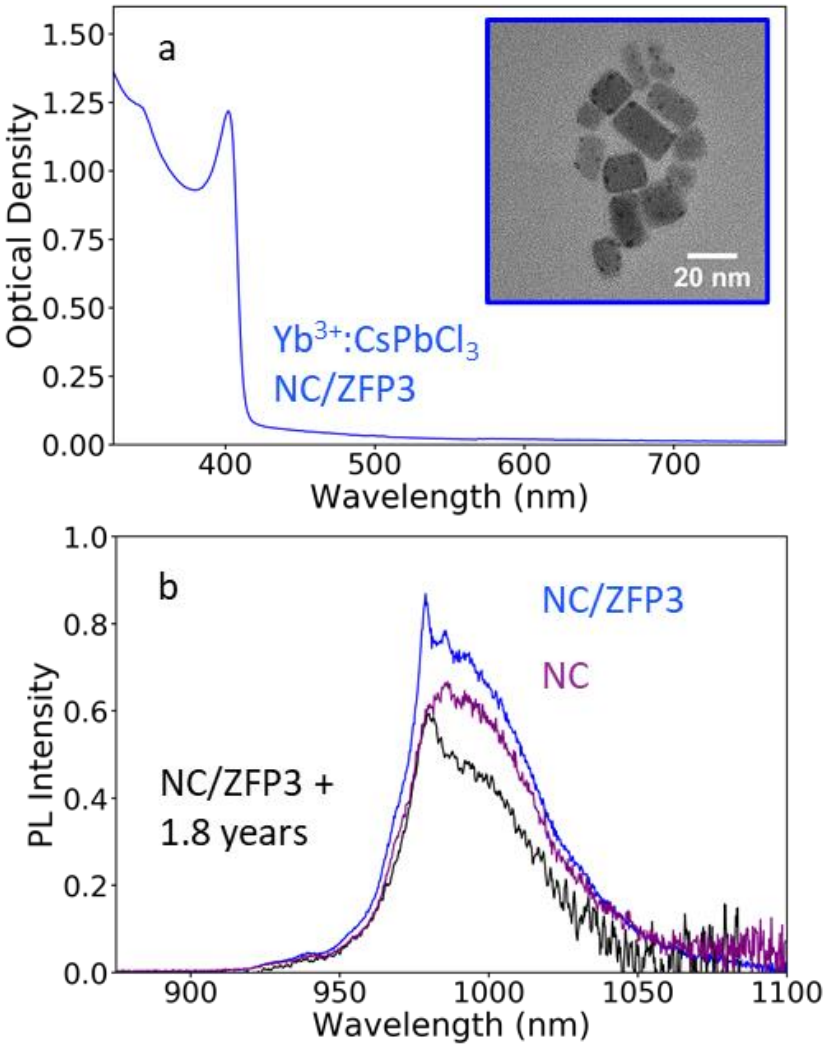

Figure 5.8 (a) Absorption spectra of a Yb^{3+}:$CsPbCl_3$ NC/ZPF3 composite film drop cast from butyl acetate. *Inset*: TEM image of these NCs in the NC/ZFP3 composite. (b) NIR PL spectra of the Yb^{3+}:$CsPbCl_3$ NC/polymer composite shown in panel (a). The PL spectra of the NC/ZFP3 composite after 1.8 years of dark, ambient storage and of the drop-cast zwitterionic-ligand capped NCs without polymer are also provided for reference. These PL spectra were measured quantitatively such that relative integrated intensities are proportional to relative PLQYs.

5.4 Conclusion

In summary, we demonstrate a straightforward method to synthesize a full series of novel, modular zwitterion-functionalized poly(isopropyl methacrylate) polymers that can be specifically tailored to host different types of luminescent perovskite NCs. These polymers use tunable

zwitterionic anchor groups to stabilize the perovskite NCs, and they use fluorinated or non-fluorinated moieties to tune other optical characteristics, making them useful for hosting a broad array of doped and undoped perovskite NCs. As-prepared perovskite NCs could be easily transferred into these polymers *via* simple ligand exchange and precipitation, and the resulting perovskite NC/polymer composites show good NC solubility in most solvents, including green solvents like ethyl and butyl acetate. These solvated composites could be easily cast into high-optical-quality solid thin films for further optical interrogation or application. The NC PLQYs and ambient stabilities in these polymers are substantially enhanced relative to those in more conventional PMMA polymer matrices. Overall, these findings establish this class of zwitterion-functionalized polymers as a flexible platform for advancing fundamental research involving perovskite NC/polymer composites and may help to advance the commercialization potential of perovskite NCs by facilitating full-scale manufacturing of luminescent NC-based composites *via* solution processing with green solvents.

Chapter 6. CONCLUSION AND OUTLOOK

(This chapter is adapted from two papers published by Yunping Huang during this Ph.D program) [27,221]

Organic semiconductors and inorganic nanomaterials have advanced at a remarkable pace over the past two decades, achieving unprecedented performance and showing a promising future for commercial applications. However, their potential has not yet been fully realized. As for organic semiconductors, most high-performance materials require long synthetic procedures, which deviates from our original vision of low-cost materials. Moreover, the intense use of toxic or dangerous reagents during the synthesis has raised concerns for future, large-scale production. Similarly, although the synthesis of inorganic nanomaterials is more straightforwards compared to organic semiconductors, the use of toxic elements such as lead and cadmium prevails in material synthesis. Regarding device fabrication, most of the devices from both organic semiconductor and inorganic nanomaterials in scientific reports are small-area devices fabricated by spin-coating or thermal evaporation, which causes much material loss, increasing the cost of the final devices. In addition, either spin-coating or thermal evaporation is not suitable for manufacturing large-area devices on an industrial scale. To address the above problems, refocusing their research on the commercial viability and environmental sustainability of organic semiconductors are crucial for future technology developments.

Both organic semiconductors and inorganic nanomaterials are rising optoelectronic materials with high structural tunability, and such common grounds lay the foundation for interdisciplinary collaborations between these two domains, not only consummating certain existing ideas but also establishing the foundation for a new research domain. Take the recent surge of chiral spintronics research as an example.[222-224] Chiral spintronics utilize the connection

between the electron spins (a quantum physics concept) and the chirality of organic compounds (a chemistry concept), which is their mirror-reflection asymmetry as shown in Figure. 6.1. Moving spins can couple to a chiral object via spin-orbit coupling. When the spin possesses the same handedness as the chiral object, it can travel a longer distance. Such hybridization with chiral structures not only removes the requirement of an external magnetic field in traditional spintronics, but also leads to significantly larger spin currents compared to other spin-orbit-coupling-based devices from the achiral counterparts. Such enhancement is crucial to achieve higher signal-to-noise ratios and reduce electricity consumption. Currently one of the topics of interest in chiral spintronics is introducing chiral ligand to QD surfaces, leveraging the quantum confinement effect to obtain robust spin states at room temperature and chiral effect to enhance spin current.[223] This case exemplifies the fact that the organic-inorganic interface is a hybrid domain that requires the fusion of knowledge from multiple scientific disciplines via familiarizing a broad range of introductory content regarding organic building blocks to researchers from non-organic-chemistry backgrounds. We hope that by sharing this anchor-functionality paradigm with interdisciplinary research, we can spark other novel collaborative ideas in these communities.

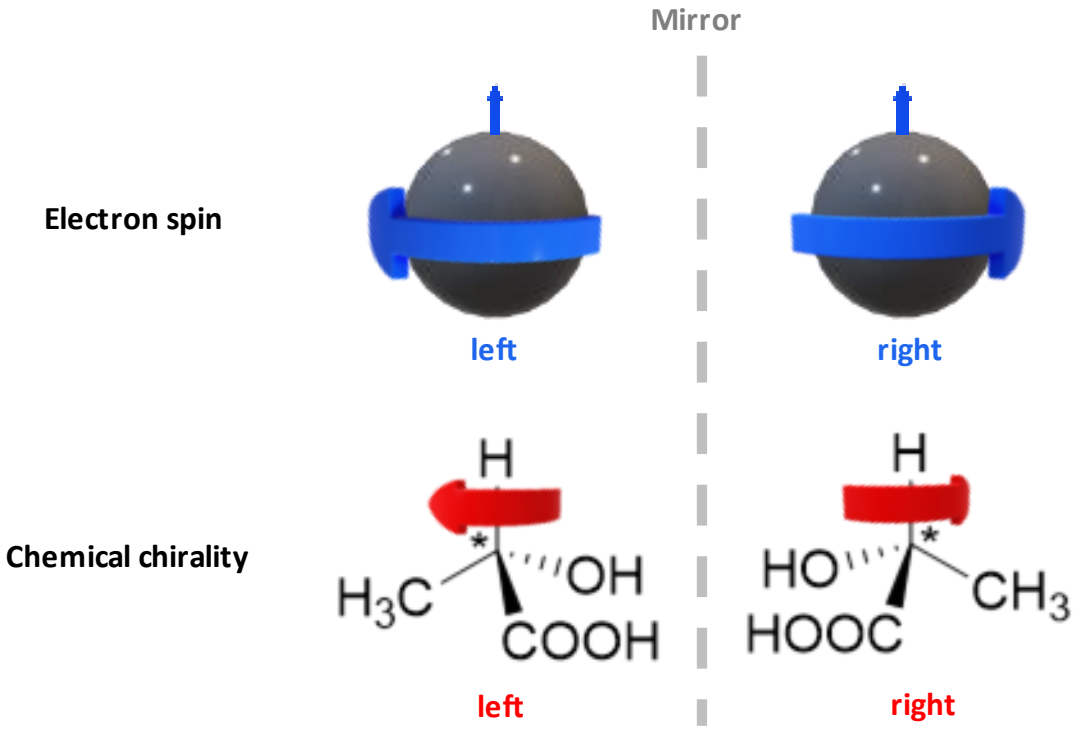

Figure 6.1. The mirror-reflection asymmetry comparison between electron spins and chirality of chemical compounds. The small blue arrows and the big blue arrows respectively represent the moving directions and spinning directions of electrons. The red arrows indicated the chirality of two lactic acid enantiomers. The direction of the red arrow is defined by the arrangement of the functional groups around the chiral centers (marked with "*"), with the order of -OH > -COOH > $-CH_3$.

BIBLIOGRAPHY

(1) Holick, M. F. In *Sunlight, Vitamin D and Skin Cancer*; Reichrath, J., Ed.; Springer New York: New York, NY, 2008, DOI:10.1007/978-0-387-77574-6_1 10.1007/978-0-387-77574-6_1.

(2) Knez, I. Effects of indoor lighting on mood and cognition. *J. Environ. Psychol.* **1995,** *15* (1), 39.

(3) Jou, J.-H.; Shen, S.-M.; Lin, C.-R.; Wang, Y.-S.; Chou, Y.-C.; Chen, S.-Z.; Jou, Y.-C. Efficient very-high color rendering index organic light-emitting diode. *Org. Electron.* **2011,** *12* (5), 865.

(4) Wang, W.; Brinker, A. C. d.; Stuijk, S.; Haan, G. d. 2017 12th IEEE International Conference on Automatic Face & Gesture Recognition (FG 2017), 2017; p 71.

(5) Hatori, M.; Gronfier, C.; Van Gelder, R. N.; Bernstein, P. S.; Carreras, J.; Panda, S.; Marks, F.; Sliney, D.; Hunt, C. E.; Hirota, T.et al. Global rise of potential health hazards caused by blue light-induced circadian disruption in modern aging societies. *npj aging mech. dis.* **2017,** *3* (1), 9.

(6) Glickman, G.; Byrne, B.; Pineda, C.; Hauck, W. W.; Brainard, G. C. Light Therapy for Seasonal Affective Disorder with Blue Narrow-Band Light-Emitting Diodes (LEDs). *Biol. Psychiatry* **2006,** *59* (6), 502.

(7) Mueller-Mach, R.; Mueller, G.; Krames, M. R.; Höppe, H. A.; Stadler, F.; Schnick, W.; Juestel, T.; Schmidt, P. Highly efficient all-nitride phosphor-converted white light emitting diode. *Phys. Status Solidi A* **2005,** *202* (9), 1727.

(8) Okamoto, K.; Yanagi, T.; Takita, S.; Tanaka, M.; Higuchi, T.; Ushida, Y.; Watanabe, H., 1996; p 111.

(9) Chen, D.; Xiang, W.; Liang, X.; Zhong, J.; Yu, H.; Ding, M.; Lu, H.; Ji, Z. Advances in transparent glass–ceramic phosphors for white light-emitting diodes—A review. *J. Eur. Ceram. Soc.* **2015,** *35* (3), 859.

(10) Song, H.; Lee, S. Red light emitting solid state hybrid quantum dot–near-UV GaN LED devices. *Nanotechnology* **2007,** *18* (25), 255202.

(11) Lee, K. M.; Cheah, K. W.; An, B. L.; Gong, M. L.; Liu, Y. L. Emission characteristics of inorganic/organic hybrid white-light phosphor. *Appl. Phys. A* **2005,** *80* (2), 337.

(12) Tan, C. M.; Singh, P.; Zhao, W.; Kuo, H.-C. Physical Limitations of Phosphor layer thickness and concentration for White LEDs. *Sci. Rep.* **2018,** *8* (1), 2452.

(13) Pan, Y.; Wu, M.; Su, Q. Tailored photoluminescence of YAG:Ce phosphor through various methods. *J. Phys. Chem. Solids* **2004,** *65* (5), 845.

(14) Yang, Y.; Zheng, Y.; Cao, W.; Titov, A.; Hyvonen, J.; Manders, J. R.; Xue, J.; Holloway, P. H.; Qian, L. High-efficiency light-emitting devices based on quantum dots with tailored nanostructures. *Nat. Photonics* **2015,** *9* (4), 259.

(15) Tian, Y. Development of phosphors with high thermal stability and efficiency for phosphor-converted LEDs. *J. Solid State Light.* **2014,** *1* (1), 11.

(16) Kim, Y. H.; Arunkumar, P.; Kim, B. Y.; Unithrattil, S.; Kim, E.; Moon, S.-H.; Hyun, J. Y.; Kim, K. H.; Lee, D.; Lee, J.-S.et al. A zero-thermal-quenching phosphor. *Nat. Mater.* **2017,** *16* (5), 543.

(17) Ahn, Y. N.; Kim, K. D.; Anoop, G.; Kim, G. S.; Yoo, J. S. Design of highly efficient phosphor-converted white light-emitting diodes with color rendering indices ($R1 - R15) \geq$ 95 for artificial lighting. *Sci. Rep.* **2019,** *9* (1), 16848.

(18) Pietryga, J. M.; Park, Y.-S.; Lim, J.; Fidler, A. F.; Bae, W. K.; Brovelli, S.; Klimov, V. I. Spectroscopic and Device Aspects of Nanocrystal Quantum Dots. *Chem. Rev.* **2016,** *116* (18), 10513.

(19) García-Rodríguez, R.; Hendricks, M. P.; Cossairt, B. M.; Liu, H.; Owen, J. S. Conversion Reactions of Cadmium Chalcogenide Nanocrystal Precursors. *Chem. Mater.* **2013,** *25* (8), 1233.

(20) Zhao, X.; Ng, J. D. A.; Friend, R. H.; Tan, Z.-K. Opportunities and Challenges in Perovskite Light-Emitting Devices. *ACS Photonics* **2018,** *5* (10), 3866.

(21) Kolny-Olesiak, J.; Weller, H. Synthesis and Application of Colloidal CuInS2 Semiconductor Nanocrystals. *ACS Appl. Mater. Interfaces* **2013,** *5* (23), 12221.

(22) Pietra, F.; van Dijk - Moes, R. J. A.; Ke, X.; Bals, S.; Van Tendeloo, G.; de Mello Donega, C.; Vanmaekelbergh, D. Synthesis of Highly Luminescent Silica-Coated CdSe/CdS Nanorods. *Chem. Mater.* **2013,** *25* (17), 3427.

(23) Sun, C.; Zhang, Y.; Ruan, C.; Yin, C.; Wang, X.; Wang, Y.; Yu, W. W. Efficient and Stable White LEDs with Silica-Coated Inorganic Perovskite Quantum Dots. *Adv. Mater.* **2016,** *28* (45), 10088.

(24) Reiss, P.; Carrière, M.; Lincheneau, C.; Vaure, L.; Tamang, S. Synthesis of Semiconductor Nanocrystals, Focusing on Nontoxic and Earth-Abundant Materials. *Chem. Rev.* **2016,** *116* (18), 10731.

(25) Martin, L.; Roderick, E.; Michael, R. The Availability of Indium: The Present, Medium Term, and Long Term. **2015**, DOI:10.2172/1327212 10.2172/1327212.

(26) Pattison, M.; Hansen, M.; Bradsley, N.; Elliott, C.; Lee, K.; Pattison, L.; Tsao, J. 2019 Lighting R&D Opportunities. **2020**.

(27) Huang, Y.; Elder, D. L.; Kwiram, A. L.; Jenekhe, S. A.; Jen, A. K. Y.; Dalton, L. R.; Luscombe, C. K. Organic Semiconductors at the University of Washington: Advancements in Materials Design and Synthesis and toward Industrial Scale Production. *Adv. Mater.* **2021,** *33* (22), 1904239.

(28) Huang, Y.; Liu, Y.; Sommerville, P. J. W.; Kaminsky, W.; Ginger, D. S.; Luscombe, C. K. Theobromine and direct arylation: a sustainable and scalable solution to minimize aggregation caused quenching. *Green. Chem.* **2019,** *21* (24), 6600.

(29) Hong, Y.; Lam, J. W. Y.; Tang, B. Z. Aggregation-induced emission. *Chem. Soc. Rev.* **2011,** *40* (11), 5361.

(30) Zhao, Z.; Gao, S.; Zheng, X.; Zhang, P.; Wu, W.; Kwok, R. T. K.; Xiong, Y.; Leung, N. L. C.; Chen, Y.; Gao, X.et al. Rational Design of Perylenediimide-Substituted Triphenylethylene to Electron Transporting Aggregation-Induced Emission Luminogens (AIEgens) with High Mobility and Near-Infrared Emission. *Adv. Funct. Mater.* **2018,** *28* (11), 1705609.

(31) Lai, W.-Y.; Zhu, R.; Fan, Q.-L.; Hou, L.-T.; Cao, Y.; Huang, W. Monodisperse Six-Armed Triazatruxenes: Microwave-Enhanced Synthesis and Highly Efficient Pure-Deep-Blue Electroluminescence. *Macromolecules* **2006,** *39* (11), 3707.

(32) Lai, W.-Y.; Xia, R.; Bradley, D. D. C.; Huang, W. 2,3,7,8,12,13-Hexaaryltruxenes: An ortho-Substituted Multiarm Design and Microwave-Accelerated Synthesis toward Starburst Macromolecular Materials with Well-Defined π Delocalization. *Eur. J. Chem.* **2010,** *16* (28), 8471.

(33) Molnár, Á. Efficient, Selective, and Recyclable Palladium Catalysts in Carbon−Carbon Coupling Reactions. *Chem. Rev.* **2011,** *111* (3), 2251.

(34) Bura, T.; Blaskovits, J. T.; Leclerc, M. Direct (Hetero)arylation Polymerization: Trends and Perspectives. *J. Am. Chem. Soc.* **2016,** *138* (32), 10056.

(35) Huang, Y.; Luscombe, C. K. Towards Green Synthesis and Processing of Organic Solar Cells. *Chem. Rec.* **2019,** *19* (6), 1039.

(36) Strotman, N. A.; Chobanian, H. R.; Guo, Y.; He, J.; Wilson, J. E. Highly Regioselective Palladium-Catalyzed Direct Arylation of Oxazole at C-2 or C-5 with Aryl Bromides, Chlorides, and Triflates. *Org. Lett.* **2010,** *12* (16), 3578.

(37) Barber, J. S.; Scales, S.; Tran-Dubé, M.; Wang, F.; Sach, N. W.; Bernier, L.; Collins, M. R.; Zhu, J.; McAlpine, I. J.; Patman, R. L. Rhodium(III)-Catalyzed C–H Activation: Ligand-Controlled Regioselective Synthesis of 4-Methyl-Substituted Dihydroisoquinolones. *Org. Lett.* **2019,** *21* (14), 5689.

(38) Vidyacharan, S.; Ramanjaneyulu, B. T.; Jang, S.; Kim, D.-P. Continuous-Flow Visible Light Organophotocatalysis for Direct Arylation of 2H-Indazoles: Fast Access to Drug Molecules. *ChemSusChem* **2019,** *12* (12), 2581.

(39) Gorelsky, S. I.; Lapointe, D.; Fagnou, K. Analysis of the Concerted Metalation-Deprotonation Mechanism in Palladium-Catalyzed Direct Arylation Across a Broad Range of Aromatic Substrates. *J. Am. Chem. Soc.* **2008,** *130* (33), 10848.

(40) Huang, Y.; Zheng, N.; Wang, Z.; Ying, L.; Huang, F.; Cao, Y. Synthesis of regioregular π-conjugated polymers consisting of a lactam moiety via direct heteroarylation polymerization. *Chem. Commun.* **2017,** *53* (12), 1997.

(41) Würthner, F.; Saha-Möller, C. R.; Fimmel, B.; Ogi, S.; Leowanawat, P.; Schmidt, D. Perylene Bisimide Dye Assemblies as Archetype Functional Supramolecular Materials. *Chem. Rev.* **2016,** *116* (3), 962.

(42) Li, W.; Liu, D.; Shen, F.; Ma, D.; Wang, Z.; Feng, T.; Xu, Y.; Yang, B.; Ma, Y. A Twisting Donor-Acceptor Molecule with an Intercrossed Excited State for Highly Efficient, Deep-Blue Electroluminescence. *Adv. Funct. Mater.* **2012,** *22* (13), 2797.

(43) Li, W.; Pan, Y.; Xiao, R.; Peng, Q.; Zhang, S.; Ma, D.; Li, F.; Shen, F.; Wang, Y.; Yang, B.et al. Employing ∼100% Excitons in OLEDs by Utilizing a Fluorescent Molecule with Hybridized Local and Charge-Transfer Excited State. *Adv. Funct. Mater.* **2014,** *24* (11), 1609.

(44) Köhn, A.; Hättig, C. On the Nature of the Low-Lying Singlet States of 4-(Dimethyl-amino)benzonitrile. *J. Am. Chem. Soc.* **2004,** *126* (23), 7399.

(45) McGehee, M. D.; Heeger, A. J. Semiconducting (Conjugated) Polymers as Materials for Solid-State Lasers. *Adv. Mater.* **2000,** *12* (22), 1655.

(46) Zhou, J.; Wan, X.; Liu, Y.; Zuo, Y.; Li, Z.; He, G.; Long, G.; Ni, W.; Li, C.; Su, X.et al. Small Molecules Based on Benzo[1,2-b:4,5-b′]dithiophene Unit for High-Performance Solution-Processed Organic Solar Cells. *J. Am. Chem. Soc.* **2012,** *134* (39), 16345.

(47) Walker, B.; Kim, C.; Nguyen, T.-Q. Small Molecule Solution-Processed Bulk Heterojunction Solar Cells. *Chem. Mater.* **2011,** *23* (3), 470.

(48) Campoy-Quiles, M.; Heliotis, G.; Xia, R.; Ariu, M.; Pintani, M.; Etchegoin, P.; Bradley, D. D. C. Ellipsometric Characterization of the Optical Constants of Polyfluorene Gain Media. *Adv. Funct. Mater.* **2005,** *15* (6), 925.

(49) Ziffer, M. E.; Jo, S. B.; Liu, Y.; Zhong, H.; Mohammed, J. C.; Harrison, J. S.; Jen, A. K. Y.; Ginger, D. S. Tuning H- and J-Aggregate Behavior in π-Conjugated Polymers via Noncovalent Interactions. *J. Phys. Chem. C* **2018,** *122* (33), 18860.

(50) Huang, Y.; Cohen, T. A.; Sommerville, P. J. W.; Luscombe, C. K. Green syntheses of stable and efficient organic dyes for organic hybrid light-emitting diodes. *J. Mater. Chem. C* **2021,** *9* (23), 7274.

(51) Morgan Pattison, P.; Hansen, M.; Tsao, J. Y. LED lighting efficacy: Status and directions. *C. R. Phys.* **2018,** *19* (3), 134.

(52) Ye, S.; Xiao, F.; Pan, Y. X.; Ma, Y. Y.; Zhang, Q. Y. Phosphors in Phosphor-Converted White Light-Emitting Diodes: Recent Advances in Materials, Techniques and Properties. *Mater. Sci. Eng., R* **2010,** *71*, 1.

(53) Park, H. K.; Oh, J. H.; Rag Do, Y. Toward scatter-free phosphors in white phosphor-converted light-emitting diodes. *Opt. Express* **2012,** *20* (9), 10218.

(54) Nyman, M.; Shea-Rohwer, L. E.; Martin, J. E.; Provencio, P. Nano-YAG:Ce Mechanisms of Growth and Epoxy-Encapsulation. *Chem. Mater.* **2009,** *21* (8), 1536.

(55) Razo, I.; Carrizales, L.; Castro, J.; Díaz-Barriga, F.; Monroy, M. Arsenic and Heavy Metal Pollution of Soil, Water and Sediments in a Semi-Arid Climate Mining Area in Mexico. *Water, Air, Soil Pollut.* **2004,** *152* (1), 129.

(56) Swenson, J. J.; Carter, C. E.; Domec, J.-C.; Delgado, C. I. Gold Mining in the Peruvian Amazon: Global Prices, Deforestation, and Mercury Imports. *PLOS ONE* **2011,** *6* (4), e18875.

(57) Sonter, L. J.; Ali, S. H.; Watson, J. E. M. Mining and biodiversity: key issues and research needs in conservation science. *Proc. Biol. Sci.* **2018,** *285* (1892), 20181926.

(58) Speller, E. M.; Clarke, A. J.; Luke, J.; Lee, H. K. H.; Durrant, J. R.; Li, N.; Wang, T.; Wong, H. C.; Kim, J.-S.; Tsoi, W. C.et al. From fullerene acceptors to non-fullerene

acceptors: prospects and challenges in the stability of organic solar cells. *J. Mater. Chem. A* **2019,** *7* (41), 23361.

(59) Jørgensen, M.; Norrman, K.; Gevorgyan, S. A.; Tromholt, T.; Andreasen, B.; Krebs, F. C. Stability of Polymer Solar Cells. *Adv. Mater.* **2012,** *24* (5), 580.

(60) Zhao, C.; Duan, L. Review on photo- and electrical aging mechanisms for neutral excitons and ions in organic light-emitting diodes. *J. Mater. Chem. C* **2020,** *8* (3), 803.

(61) Manceau, M.; Rivaton, A.; Gardette, J.-L.; Guillerez, S.; Lemaître, N. The mechanism of photo- and thermooxidation of poly(3-hexylthiophene) (P3HT) reconsidered. *Polym. Degrad. Stab.* **2009,** *94* (6), 898.

(62) Manceau, M.; Gaume, J.; Rivaton, A.; Gardette, J.-L.; Monier, G.; Bideux, L. Further insights into the photodegradation of poly(3-hexylthiophene) by means of X-ray photoelectron spectroscopy. *Thin Solid Films* **2010,** *518* (23), 7113.

(63) Rivaton, A.; Chambon, S.; Manceau, M.; Gardette, J.-L.; Lemaître, N.; Guillerez, S. Light-induced degradation of the active layer of polymer-based solar cells. *Polym. Degrad. Stab.* **2010,** *95* (3), 278.

(64) Rivaton, A.; Tournebize, A.; Gaume, J.; Bussière, P.-O.; Gardette, J.-L.; Therias, S. Photostability of organic materials used in polymer solar cells. *Polym. Int.* **2014,** *63* (8), 1335.

(65) Speller, E. M.; Clarke, A. J.; Aristidou, N.; Wyatt, M. F.; Francàs, L.; Fish, G.; Cha, H.; Lee, H. K. H.; Luke, J.; Wadsworth, A.et al. Toward Improved Environmental Stability of Polymer:Fullerene and Polymer:Nonfullerene Organic Solar Cells: A Common Energetic Origin of Light- and Oxygen-Induced Degradation. *ACS Energy Lett.* **2019,** *4* (4), 846.

(66) Manceau, M.; Rivaton, A.; Gardette, J.-L. Involvement of Singlet Oxygen in the Solid-State Photochemistry of P3HT. *Macromol. Rapid Commun.* **2008,** *29* (22), 1823.

(67) Yao, L.; Zhang, S.; Wang, R.; Li, W.; Shen, F.; Yang, B.; Ma, Y. Highly Efficient Near-Infrared Organic Light-Emitting Diode Based on a Butterfly-Shaped Donor–Acceptor Chromophore with Strong Solid-State Fluorescence and a Large Proportion of Radiative Excitons. *Angew. Chem. Int. Ed.* **2014,** *53* (8), 2119.

(68) Lee, Will W. H.; Zhao, Z.; Cai, Y.; Xu, Z.; Yu, Y.; Xiong, Y.; Kwok, R. T. K.; Chen, Y.; Leung, N. L. C.; Ma, D.et al. Facile access to deep red/near-infrared emissive AIEgens for efficient non-doped OLEDs. *Chem. Sci.* **2018,** *9* (28), 6118.

(69) Qin, W.; Li, K.; Feng, G.; Li, M.; Yang, Z.; Liu, B.; Tang, B. Z. Bright and Photostable Organic Fluorescent Dots with Aggregation-Induced Emission Characteristics for Noninvasive Long-Term Cell Imaging. *Adv. Funct. Mater.* **2014,** *24* (5), 635.

(70) Lo, Y.-C.; Yeh, T.-H.; Wang, C.-K.; Peng, B.-J.; Hsieh, J.-L.; Lee, C.-C.; Liu, S.-W.; Wong, K.-T. High-Efficiency Red and Near-Infrared Organic Light-Emitting Diodes Enabled by Pure Organic Fluorescent Emitters and an Exciplex-Forming Cohost. *ACS Appl. Mater. Interfaces* **2019,** *11* (26), 23417.

(71) Wei, P.; Duan, L.; Zhang, D.; Qiao, J.; Wang, L.; Wang, R.; Dong, G.; Qiu, Y. A new type of light-emitting naphtho[2,3-c][1,2,5]thiadiazole derivatives: synthesis, photophysical characterization and transporting properties. *J. Mater. Chem.* **2008,** *18* (7), 806.

(72) Fudickar, W.; Linker, T. Why Triple Bonds Protect Acenes from Oxidation and Decomposition. *J. Am. Chem. Soc.* **2012,** *134* (36), 15071.

(73) Li, Y.; Zhang, X.; Zhang, Y.; Dong, R.; Luscombe, C. K. Review on the Role of Polymers in Luminescent Solar Concentrators. *J. Polym. Sci., Part A: Polym. Chem.* **2019,** *57* (3), 201.

(74) Liu, T.; Zhu, L.; Zhong, C.; Xie, G.; Gong, S.; Fang, J.; Ma, D.; Yang, C. Naphthothiadiazole-Based Near-Infrared Emitter with a Photoluminescence Quantum Yield of 60% in Neat Film and External Quantum Efficiencies of up to 3.9% in Nondoped OLEDs. *Adv. Funct. Mater.* **2017,** *27* (12), 1606384.

(75) Chen, C. H.; Tang, C. W.; Shi, J.; Klubek, K. P. Improved red dopants for organic electroluminescent devices. *Macromolecular Symposia* **1998,** *125* (1), 49.

(76) Liu, T.-H.; Iou, C.-Y.; Chen, C. H. Development of highly stable organic electroluminescent devices with a doped co-host emitter system. *Curr. Appl. Phys.* **2005,** *5* (3), 218.

(77) Zhao, B.; Zhang, T.; Chu, B.; Li, W.; Su, Z.; Wu, H.; Yan, X.; Jin, F.; Gao, Y.; Liu, C. Highly efficient red OLEDs using DCJTB as the dopant and delayed fluorescent exciplex as the host. *Sci. Rep.* **2015,** *5* (1), 10697.

(78) Slooff, L. H.; Bakker, N. J.; Sommeling, P. M.; Büchtemann, A.; Wedel, A.; van Sark, W. G. J. H. M. Long-term optical stability of fluorescent solar concentrator plates. *Phys. Status Solidi A* **2014,** *211* (5), 1150.

(79) Guo, S.; Cao, B.; Wang, W.; Moulin, J.-F.; Müller-Buschbaum, P. Effect of Alcohol Treatment on the Performance of PTB7:PC71BM Bulk Heterojunction Solar Cells. *ACS Appl. Mater. Interfaces* **2015,** *7* (8), 4641.

(80) Schmidt, S. B.; Biskup, T.; Jiao, X.; McNeill, C. R.; Sommer, M. Controlling intermolecular redox-doping of naphthalene diimides. *J. Mater. Chem. C* **2019,** *7* (15), 4466.

(81) Huang, Y.; Xu, W.; Zhou, C.; Zhong, W.; Xie, R.; Gong, X.; Ying, L.; Huang, F.; Cao, Y. Synthesis of medium-bandgap π-Conjugated polymers based on isomers of 5-Alkylphenanthridin-6(5H)-one and 6-Alkoxylphenanthridine. *J. Polym. Sci., Part A: Polym. Chem.* **2016,** *54* (14), 2119.

(82) David, A.; Fini, P. T.; Houser, K. W.; Ohno, Y.; Royer, M. P.; Smet, K. A. G.; Wei, M.; Whitehead, L. Development of the IES method for evaluating the color rendition of light sources. *Opt. Express* **2015,** *23* (12), 15888.

(83) Peng, Y.; Wang, H.; Liu, J.; Sun, Q.; Mou, Y.; Guo, X. Broad-Band and Stable Phosphor-in-Glass Enabling Ultrahigh Color Rendering for All-Inorganic High-Power WLEDs. *ACS Appl. Electron. Mater.* **2020,** *2* (9), 2929.

(84) Yoon, H. C.; Oh, J. H.; Lee, S.; Park, J. B.; Do, Y. R. Circadian-tunable Perovskite Quantum Dot-based Down-Converted Multi-Package White LED with a Color Fidelity Index over 90. *Sci. Rep.* **2017,** *7* (1), 2808.

(85) Shukla, A.; Wallwork, N. R.; Li, X.; Sobus, J.; Mai, V. T. N.; McGregor, S. K. M.; Chen, K.; Lepage, R. J.; Krenske, E. H.; Moore, E. G.et al. Deep-Red Lasing and Amplified Spontaneous Emission from Nature Inspired Bay-Annulated Indigo Derivatives. *Adv. Opt. Mater.* **2020,** *8* (2), 1901350.

(86) Caspar, J. V.; Meyer, T. J. Application of the energy gap law to nonradiative, excited-state decay. *J. Phys. Chem.* **1983,** *87* (6), 952.

(87) Wiles, A. A.; Bruckbauer, J.; Mohammed, N.; Cariello, M.; Cameron, J.; Findlay, N. J.; Taylor-Shaw, E.; Wallis, D. J.; Martin, R. W.; Skabara, P. J.et al. A poly(urethane)-encapsulated benzo[2,3-d:6,7-d′]diimidazole organic down-converter for green hybrid LEDs. *Mater. Chem. Front.* **2020,** *4* (3), 1006.

(88) Findlay, N. J.; Bruckbauer, J.; Inigo, A. R.; Breig, B.; Arumugam, S.; Wallis, D. J.; Martin, R. W.; Skabara, P. J. An Organic Down-Converting Material for White-Light Emission from Hybrid LEDs. *Adv. Mater.* **2014,** *26* (43), 7290.

(89) Hide, F.; Kozodoy, P.; DenBaars, S. P.; Heeger, A. J. White light from InGaN/conjugated polymer hybrid light-emitting diodes. *Appl. Phys. Lett.* **1997,** *70* (20), 2664.

(90) Li, Z.; Kong, L.; Huang, S.; Li, L. Highly Luminescent and Ultrastable CsPbBr3 Perovskite Quantum Dots Incorporated into a Silica/Alumina Monolith. *Angew. Chem. Int. Ed.* **2017,** *56* (28), 8134.

(91) Kim, Y.; Ham, S.; Jang, H.; Min, J. H.; Chung, H.; Lee, J.; Kim, D.; Jang, E. Bright and Uniform Green Light Emitting InP/ZnSe/ZnS Quantum Dots for Wide Color Gamut Displays. *ACS Appl. Nano Mater.* **2019,** *2* (3), 1496.

(92) Guan, H.; Zhao, S.; Wang, H.; Yan, D.; Wang, M.; Zang, Z. Room temperature synthesis of stable single silica-coated CsPbBr3 quantum dots combining tunable red emission of Ag–In–Zn–S for High-CRI white light-emitting diodes. *Nano Energy* **2020,** *67*, 104279.

(93) Espasa, A.; Lang, M.; Aguiño, C. F.; Sanchez-deAlcazar, D.; Fernández-Blázquez, J. P.; Sonnewald, U.; Cortajarena, A. L.; Coto, P. B.; Costa, R. D. Long-living and highly efficient bio-hybrid light-emitting diodes with zero-thermal-quenching biophosphors. *Nat. Commun.* **2020,** *11* (1), 879.

(94) Fernández-Luna, V.; Fernández-Blázquez, J. P.; Monclús, M. A.; Rojo, F. J.; Daza, R.; Sanchez-deAlcazar, D.; Cortajarena, A. L.; Costa, R. D. Biogenic fluorescent protein–silk fibroin phosphors for high performing light-emitting diodes. *Mater. Horiz.* **2020,** *7* (7), 1790.

(95) Niklaus, L.; Tansaz, S.; Dakhil, H.; Weber, K. T.; Pröschel, M.; Lang, M.; Kostrzewa, M.; Coto, P. B.; Detsch, R.; Sonnewald, U.et al. Micropatterned Down-Converting Coating for White Bio-Hybrid Light-Emitting Diodes. *Adv. Funct. Mater.* **2017,** *27* (1), 1601792.

(96) Yu, L.; Wu, Z.; Xie, G.; Zeng, W.; Ma, D.; Yang, C. Molecular design to regulate the photophysical properties of multifunctional TADF emitters towards high-performance TADF-based OLEDs with EQEs up to 22.4% and small efficiency roll-offs. *Chem. Sci.* **2018,** *9* (5), 1385.

(97) Liu, Y.; Chen, Y.; Li, H.; Wang, S.; Wu, X.; Tong, H.; Wang, L. High-Performance Solution-Processed Red Thermally Activated Delayed Fluorescence OLEDs Employing Aggregation-Induced Emission-Active Triazatruxene-Based Emitters. *ACS Appl. Mater. Interfaces* **2020,** *12* (27), 30652.

(98) Ding, D.; Wang, Z.; Li, C.; Zhang, J.; Duan, C.; Wei, Y.; Xu, H. Highly Efficient and Color-Stable Thermally Activated Delayed Fluorescence White Light-Emitting Diodes Featured with Single-Doped Single Emissive Layers. *Adv. Mater.* **2020,** *32* (10), 1906950.

(99) Chen, J.-X.; Tao, W.-W.; Chen, W.-C.; Xiao, Y.-F.; Wang, K.; Cao, C.; Yu, J.; Li, S.; Geng, F.-X.; Adachi, C.et al. Red/Near-Infrared Thermally Activated Delayed Fluorescence OLEDs with Near 100 % Internal Quantum Efficiency. *Angew. Chem. Int. Ed.* **2019,** *58* (41), 14660.

(100) Li, J.; Nakagawa, T.; MacDonald, J.; Zhang, Q.; Nomura, H.; Miyazaki, H.; Adachi, C. Highly Efficient Organic Light-Emitting Diode Based on a Hidden Thermally Activated Delayed Fluorescence Channel in a Heptazine Derivative. *Adv. Mater.* **2013,** *25* (24), 3319.

(101) Sadeghi, S.; Melikov, R.; Conkar, D.; Firat-Karalar, E. N.; Nizamoglu, S. White LEDs: Ultra-Efficient and High-Quality White Light-Emitting Devices using Fluorescent Proteins in Aqueous Medium (Adv. Mater. Technol. 6/2020). *Adv. Mater. Technol.* **2020,** *5* (6), 2070035.

(102) Liao, H.; Zhao, M.; Zhou, Y.; Molokeev, M. S.; Liu, Q.; Zhang, Q.; Xia, Z. Polyhedron Transformation toward Stable Narrow-Band Green Phosphors for Wide-Color-Gamut Liquid Crystal Display. *Adv. Funct. Mater.* **2019,** *29* (30), 1901988.

(103) Wei, Y.; Xing, G.; Liu, K.; Li, G.; Dang, P.; Liang, S.; Liu, M.; Cheng, Z.; Jin, D.; Lin, J. New strategy for designing orangish-red-emitting phosphor via oxygen-vacancy-induced electronic localization. *Light Sci. Appl* **2019,** *8* (1), 15.

(104) Song, E.; Zhou, Y.; Yang, X.-B.; Liao, Z.; Zhao, W.; Deng, T.; Wang, L.; Ma, Y.; Ye, S.; Zhang, Q. Highly Efficient and Stable Narrow-Band Red Phosphor Cs2SiF6:Mn4+ for High-Power Warm White LED Applications. *ACS Photonics* **2017,** *4* (10), 2556.

(105) Pust, P.; Weiler, V.; Hecht, C.; Tücks, A.; Wochnik, A. S.; Henß, A.-K.; Wiechert, D.; Scheu, C.; Schmidt, P. J.; Schnick, W. Narrow-band red-emitting Sr[LiAl3N4]:Eu2+ as a next-generation LED-phosphor material. *Nat. Mater.* **2014,** *13* (9), 891.

(106) Liu, H.; Tan, Y.; Cao, M.; Hu, H.; Wu, L.; Yu, X.; Wang, L.; Sun, B.; Zhang, Q. Fabricating CsPbX3-Based Type I and Type II Heterostructures by Tuning the Halide Composition of Janus CsPbX3/ZrO2 Nanocrystals. *ACS Nano* **2019,** *13* (5), 5366.

(107) Cohen, T. A.; Huang, Y.; Bricker, N. A.; Juhl, C. S.; Milstein, T. J.; MacKenzie, J. D.; Luscombe, C. K.; Gamelin, D. R. Modular Zwitterion-Functionalized Poly(isopropyl methacrylate) Polymers for Hosting Luminescent Lead Halide Perovskite Nanocrystals. *Chem. Mater*. **2021,** *33* (10), 3779.

(108) Makarov, N. S.; Ramasamy, K.; Jackson, A.; Velarde, A.; Castaneda, C.; Archuleta, N.; Hebert, D.; Bergren, M. R.; McDaniel, H. Fiber-Coupled Luminescent Concentrators for Medical Diagnostics, Agriculture, and Telecommunications. *ACS Nano* **2019,** *13* (8), 9112.

(109) Kim, W. H.; Jang, Y. J.; Kim, J.-Y.; Han, M.; Kang, M.; Yang, K.; Ryou, J.-H.; Kwon, M.-K. *Appl. Sci.*, 2020.

(110) Xi, M.; Jean Paul, F.; Nadarajah, N.; John, D. B. Preliminary evaluation of discomfort glare from organic light-emitting diode and edge-lit light-emitting diode lighting panels. *J. Biomed. Opt.* **2017,** *22* (5), 1.

(111) Cheng, Y.-J.; Yang, S.-H.; Hsu, C.-S. Synthesis of Conjugated Polymers for Organic Solar Cell Applications. *Chem. Rev.* **2009,** *109* (11), 5868.

(112) Huang, Y.; Cohen, T. A.; Luscombe, C. K. Naturally Derived Organic Dyes for LED Lightings of High Color Rendering and Fidelity Index. *Advanced Sustainable Systems* **2021,** *n/a* (n/a), 2000300.

(113) Nassar, N. T.; Du, X.; Graedel, T. E. Criticality of the Rare Earth Elements. *J. Ind. Ecol.* **2015,** *19* (6), 1044.

(114) Smith Stegen, K. Heavy rare earths, permanent magnets, and renewable energies: An imminent crisis. *Energy Policy* **2015,** *79*, 1.

(115) Zhu, H. M.; Lin, C. C.; Luo, W. Q.; Shu, S. T.; Liu, Z. G.; Liu, Y.; Kong, J. T.; Ma, E.; Cao, Y. G.; Liu, R. S.et al. Highly Efficient Non-Rare-Earth Red Emitting Phosphor for Warm White Light-Emitting Diodes. *Nat. Commun.* **2014,** *5*, 4312.

(116) Li, C.; Ronnier Luo, M.; Li, C.; Cui, G. The CRI-CAM02UCS colour rendering index. *Color Res. Appl.* **2012,** *37* (3), 160.

(117) Yoto, A.; Katsuura, T.; Iwanaga, K.; Shimomura, Y. Effects of Object Color Stimuli on Human Brain Activities in Perception and Attention Referred to EEG Alpha Band Response. *J. Physiol. Anthropol.* **2007,** *26* (3), 373.

(118) Wendy, D.; Yoshi, O. Proc.SPIE, 2005.

(119) Yang, J.; Jiang, C.; Zhang, Y.; Yang, R.; Yang, W.; Hou, Q.; Cao, Y. High-Efficiency Saturated Red Emitting Polymers Derived from Fluorene and Naphthoselenadiazole. *Macromolecules* **2004,** *37* (4), 1211.

(120) Piccinno, F.; Hischier, R.; Seeger, S.; Som, C. From laboratory to industrial scale: a scale-up framework for chemical processes in life cycle assessment studies. *J. Clean. Prod.* **2016,** *135*, 1085.

(121) Hartmann, S.; Weidlich, D.; Klostermeier, D. In *Methods Enzymol.*; Spies, M.;Chemla, Y. R., Eds.; Academic Press, 2016; Vol. 581.

(122) Shimizu, Y.; Azumi, T. Mechanism of external heavy atom effect on intersystem crossing in fluid solutions. Analysis based on fluorescence decay data. *J. Phys. Chem.* **1982,** *86* (1), 22.

(123) Wang, Z.; Yuan, F.; Li, X.; Li, Y.; Zhong, H.; Fan, L.; Yang, S. 53% Efficient Red Emissive Carbon Quantum Dots for High Color Rendering and Stable Warm White-Light-Emitting Diodes. *Adv. Mater.* **2017,** *29* (37), 1702910.

(124) Wang, L.; Li, W.; Yin, L.; Liu, Y.; Guo, H.; Lai, J.; Han, Y.; Li, G.; Li, M.; Zhang, J.et al. Full-color fluorescent carbon quantum dots. *Sci. Adv.* **2020,** *6* (40), eabb6772.

(125) Wang, Z.; Liu, Y.; Zhen, S.; Li, X.; Zhang, W.; Sun, X.; Xu, B.; Wang, X.; Gao, Z.; Meng, X. Gram-Scale Synthesis of 41% Efficient Single-Component White-Light-Emissive Carbonized Polymer Dots with Hybrid Fluorescence/Phosphorescence for White Light-Emitting Diodes. *Adv. Sci.* **2020,** *7* (4), 1902688.

(126) The Electronic Structure of Organic Semiconductors. *Electronic Processes in Organic Semiconductors* **2015**, DOI:https://doi.org/10.1002/9783527685172.ch1 https://doi.org/10.1002/9783527685172.ch1, 1.

(127) Bains, G. K.; Kim, S. H.; Sorin, E. J.; Narayanaswami, V. The Extent of Pyrene Excimer Fluorescence Emission Is a Reflector of Distance and Flexibility: Analysis of the Segment Linking the LDL Receptor-Binding and Tetramerization Domains of Apolipoprotein E3. *Biochemistry* **2012,** *51* (31), 6207.

(128) Hoover, G. C.; Seferos, D. S. Photoactivity and optical applications of organic materials containing selenium and tellurium. *Chem. Sci.* **2019,** *10* (40), 9182.

(129) Marchioro, A.; Whitham, P. J.; Knowles, K. E.; Kilburn, T. B.; Reid, P. J.; Gamelin, D. R. Tunneling in the Delayed Luminescence of Colloidal CdSe, Cu+-Doped CdSe, and CuInS2 Semiconductor Nanocrystals and Relationship to Blinking. *J. Phys. Chem. C* **2016,** *120* (47), 27040.

(130) Gould, I. R.; Boiani, J. A.; Gaillard, E. B.; Goodman, J. L.; Farid, S. Intersystem Crossing in Charge-Transfer Excited States. *J. Phys. Chem. A* **2003,** *107* (18), 3515.

(131) McGlynn, S. P.; Azumi, T.; Kasha, M. External Heavy-Atom Spin—Orbital Coupling Effect. V. Absorption Studies of Triplet States. *J. Chem. Phys.* **1964,** *40* (2), 507.

(132) Havlas, Z.; Michl, J. Prediction of an Inverse Heavy-Atom Effect in H−C−CH2Br: Bromine Substituent as a π Acceptor. *J. Am. Chem. Soc.* **2002,** *124* (20), 5606.

(133) Protesescu, L.; Yakunin, S.; Bodnarchuk, M. I.; Krieg, F.; Caputo, R.; Hendon, C. H.; Yang, R. X.; Walsh, A.; Kovalenko, M. V. Nanocrystals of Cesium Lead Halide Perovskites ($CsPbX_3$, X = Cl, Br, and I): Novel Optoelectronic Materials Showing Bright Emission with Wide Color Gamut. *Nano Lett.* **2015,** *15* (6), 3692.

(134) Koscher, B. A.; Swabeck, J. K.; Bronstein, N. D.; Alivisatos, A. P. Essentially Trap-Free $CsPbBr_3$ Colloidal Nanocrystals by Postsynthetic Thiocyanate Surface Treatment. *J. Am. Chem. Soc.* **2017,** *139* (19), 6566.

(135) Zhang, Y.; Siegler, T. D.; Thomas, C. J.; Abney, M. K.; Shah, T.; De Gorostiza, A.; Greene, R. M.; Korgel, B. A. A "Tips and Tricks" Practical Guide to the Synthesis of Metal Halide Perovskite Nanocrystals. *Chem. Mater.* **2020,** *32* (13), 5410.

(136) Pradhan, N. Tips and Twists in Making High Photoluminescence Quantum Yield Perovskite Nanocrystals. *ACS Energy Lett.* **2019,** *4* (7), 1634.

(137) Utzat, H.; Shulenberger, K. E.; Achorn, O. B.; Nasilowski, M.; Sinclair, T. S.; Bawendi, M. G. Probing Linewidths and Biexciton Quantum Yields of Single Cesium Lead Halide Nanocrystals in Solution. *Nano Lett.* **2017,** *17* (11), 6838.

(138) Creutz, S. E.; Crites, E. N.; De Siena, M. C.; Gamelin, D. R. Anion Exchange in Cesium Lead Halide Perovskite Nanocrystals and Thin Films Using Trimethylsilyl Halide Reagents. *Chem. Mater.* **2018,** *30* (15), 4887.

(139) Nedelcu, G.; Protesescu, L.; Yakunin, S.; Bodnarchuk, M. I.; Grotevent, M. J.; Kovalenko, M. V. Fast Anion-Exchange in Highly Luminescent Nanocrystals of Cesium Lead Halide Perovskites ($CsPbX_3$, X = Cl, Br, I). *Nano Lett.* **2015,** *15* (8), 5635.

(140) Imran, M.; Caligiuri, V.; Wang, M.; Goldoni, L.; Prato, M.; Krahne, R.; De Trizio, L.; Manna, L. Benzoyl Halides as Alternative Precursors for the Colloidal Synthesis of Lead-Based Halide Perovskite Nanocrystals. *J. Am. Chem. Soc.* **2018,** *140* (7), 2656.

(141) Milstein, T. J.; Kroupa, D. M.; Gamelin, D. R. Picosecond Quantum Cutting Generates Photoluminescence Quantum Yields Over 100% in Ytterbium-Doped $CsPbCl_3$ Nanocrystals. *Nano Lett.* **2018,** *18* (6), 3792.

(142) Liu, W.; Lin, Q.; Li, H.; Wu, K.; Robel, I.; Pietryga, J. M.; Klimov, V. I. Mn^{2+}-Doped Lead Halide Perovskite Nanocrystals with Dual-Color Emission Controlled by Halide Content. *J. Am. Chem. Soc.* **2016,** *138* (45), 14954.

(143) Pan, G.; Bai, X.; Yang, D.; Chen, X.; Jing, P.; Qu, S.; Zhang, L.; Zhou, D.; Zhu, J.; Xu, W.et al. Doping Lanthanide into Perovskite Nanocrystals: Highly Improved and Expanded Optical Properties. *Nano Lett.* **2017,** *17* (12), 8005.

(144) Zhou, D.; Liu, D.; Pan, G.; Chen, X.; Li, D.; Xu, W.; Bai, X.; Song, H. Cerium and Ytterbium Codoped Halide Perovskite Quantum Dots: A Novel and Efficient Downconverter for Improving the Performance of Silicon Solar Cells. *Adv. Mater.* **2017,** *29* (42), 1704149.

(145) De Siena, M. C.; Sommer, D. E.; Creutz, S. E.; Dunham, S. T.; Gamelin, D. R. Spinodal Decomposition During Anion Exchange in Colloidal Mn^{2+}-Doped $CsPbX_3$ (X = Cl, Br) Perovskite Nanocrystals. *Chem. Mater.* **2019,** *31* (18), 7711.

(146) Becker, M. A.; Vaxenburg, R.; Nedelcu, G.; Sercel, P. C.; Shabaev, A.; Mehl, M. J.; Michopoulos, J. G.; Lambrakos, S. G.; Bernstein, N.; Lyons, J. L.et al. Bright Triplet Excitons in Caesium Lead Halide Perovskites. *Nature* **2018,** *553* (7687), 189.

(147) Isarov, M.; Tan, L. Z.; Bodnarchuk, M. I.; Kovalenko, M. V.; Rappe, A. M.; Lifshitz, E. Rashba Effect in a Single Colloidal $CsPbBr_3$ Perovskite Nanocrystal Detected by Magneto-Optical Measurements. *Nano Lett.* **2017,** *17* (8), 5020.

(148) Liu, Z.; Vaswani, C.; Yang, X.; Zhao, X.; Yao, Y.; Song, Z.; Cheng, D.; Shi, Y.; Luo, L.; Mudiyanselage, D. H.et al. Ultrafast Control of Excitonic Rashba Fine Structure by Phonon Coherence in the Metal Halide Perovskite $CH_3NH_3PbI_3$. *Phys. Rev. Lett.* **2020,** *124* (15), 157401.

(149) Akkerman, Q. A.; Rainò, G.; Kovalenko, M. V.; Manna, L. Genesis, Challenges and Opportunities for Colloidal Lead Halide Perovskite Nanocrystals. *Nat. Mater.* **2018,** *17* (5), 394.

(150) Nenon, D. P.; Pressler, K.; Kang, J.; Koscher, B. A.; Olshansky, J. H.; Osowiecki, W. T.; Koc, M. A.; Wang, L.-W.; Alivisatos, A. P. Design Principles for Trap-Free $CsPbX_3$ Nanocrystals: Enumerating and Eliminating Surface Halide Vacancies with Softer Lewis Bases. *J. Am. Chem. Soc.* **2018,** *140* (50), 17760.

(151) Kang, J.; Wang, L.-W. High Defect Tolerance in Lead Halide Perovskite $CsPbBr_3$. *J. Phys. Chem. Lett.* **2017,** *8* (2), 489.

(152) ten Brinck, S.; Zaccaria, F.; Infante, I. Defects in Lead Halide Perovskite Nanocrystals: Analogies and (Many) Differences with the Bulk. *ACS Energy Lett.* **2019,** *4* (11), 2739.

(153) Zhou, Q.; Bai, Z.; Lu, W.-g.; Wang, Y.; Zou, B.; Zhong, H. *In situ* Fabrication of Halide Perovskite Nanocrystal-Embedded Polymer Composite Films with Enhanced Photoluminescence for Display Backlights. *Adv. Mater.* **2016,** *28* (41), 9163.

(154) Yakunin, S.; Protesescu, L.; Krieg, F.; Bodnarchuk, M. I.; Nedelcu, G.; Humer, M.; Luca, G. D.; Fiebig, M.; Heiss, W.; Kovalenko, M. V. Low-Threshold Amplified Spontaneous

Emission and Lasing from Colloidal Nanocrystals of Caesium Lead Halide Perovskites. *Nat. Commun.* **2015,** *6,* 8056.

(155) Makarov, N. S.; Guo, S.; Isaienko, O.; Liu, W.; Robel, I.; Klimov, V. I. Spectral and Dynamical Properties of Single Excitons, Biexcitons, and Trions in Cesium–Lead-Halide Perovskite Quantum Dots. *Nano Lett.* **2016,** *16* (4), 2349.

(156) Huang, C.-Y.; Zou, C.; Mao, C.; Corp, K. L.; Yao, Y.-C.; Lee, Y.-J.; Schlenker, C. W.; Jen, A. K. Y.; Lin, L. Y. $CsPbBr_3$ Perovskite Quantum Dot Vertical Cavity Lasers with Low Threshold and High Stability. *ACS Photonics* **2017,** *4* (9), 2281.

(157) Wang, Y.; Zhi, M.; Chang, Y.-Q.; Zhang, J.-P.; Chan, Y. Stable, Ultralow Threshold Amplified Spontaneous Emission from $CsPbBr_3$ Nanoparticles Exhibiting Trion Gain. *Nano Lett.* **2018,** *18* (8), 4976.

(158) Park, Y.-S.; Guo, S.; Makarov, N. S.; Klimov, V. I. Room Temperature Single-Photon Emission from Individual Perovskite Quantum Dots. *ACS Nano* **2015,** *9* (10), 10386.

(159) Rainò, G.; Nedelcu, G.; Protesescu, L.; Bodnarchuk, M. I.; Kovalenko, M. V.; Mahrt, R. F.; Stöferle, T. Single Cesium Lead Halide Perovskite Nanocrystals at Low Temperature: Fast Single-Photon Emission, Reduced Blinking, and Exciton Fine Structure. *ACS Nano* **2016,** *10* (2), 2485.

(160) Utzat, H.; Sun, W.; Kaplan, A. E. K.; Krieg, F.; Ginterseder, M.; Spokoyny, B.; Klein, N. D.; Shulenberger, K. E.; Perkinson, C. F.; Kovalenko, M. V.et al. Coherent Single-Photon Emission from Colloidal Lead Halide Perovskite Quantum Dots. *Science* **2019,** *363* (6431), 1068.

(161) Meinardi, F.; Akkerman, Q. A.; Bruni, F.; Park, S.; Mauri, M.; Dang, Z.; Manna, L.; Brovelli, S. Doped Halide Perovskite Nanocrystals for Reabsorption-Free Luminescent Solar Concentrators. *ACS Energy Lett.* **2017,** *2* (10), 2368.

(162) Zhao, H.; Benetti, D.; Tong, X.; Zhang, H.; Zhou, Y.; Liu, G.; Ma, D.; Sun, S.; Wang, Z. M.; Wang, Y.et al. Efficient and Stable Tandem Luminescent Solar Concentrators based on Carbon Dots and Perovskite Quantum Dots. *Nano Energy* **2018,** *50*, 756.

(163) Cohen, T. A.; Milstein, T. J.; Kroupa, D. M.; MacKenzie, J. D.; Luscombe, C. K.; Gamelin, D. R. Quantum-Cutting Yb^{3+}-Doped Perovskite Nanocrystals for Monolithic Bilayer Luminescent Solar Concentrators. *J. Mater. Chem. A* **2019,** *7* (15), 9279.

(164) Wei, M.; Arquer, F. P. G. d.; Walters, G.; Yang, Z.; Quan, L. N.; Kim, Y.; Sabatini, R.; Quintero-Bermudez, R.; Gao, L.; Fan, J. Z.et al. Ultrafast Narrowband Exciton Routing within Layered Perovskite Nanoplatelets Enables Low-Loss Luminescent Solar Concentrators. *Nat. Energy* **2019,** *4*, 197.

(165) Yuan, G.; Ritchie, C.; Ritter, M.; Murphy, S.; Gómez, D. E.; Mulvaney, P. The Degradation and Blinking of Single $CsPbI_3$ Perovskite Quantum Dots. *J. Phys. Chem. C* **2018,** *122* (25), 13407.

(166) Vicente, J. R.; Rafiei Miandashti, A.; Sy Piecco, K. W. E.; Pyle, J. R.; Kordesch, M. E.; Chen, J. Single-Particle Organolead Halide Perovskite Photoluminescence as a Probe for Surface Reaction Kinetics. *ACS Appl. Mater. Interfaces* **2019,** *11* (19), 18034.

(167) Meyns, M.; Perálvarez, M.; Heuer-Jungemann, A.; Hertog, W.; Ibáñez, M.; Nafria, R.; Genç, A.; Arbiol, J.; Kovalenko, M. V.; Carreras, J.et al. Polymer-Enhanced Stability of Inorganic Perovskite Nanocrystals and Their Application in Color Conversion LEDs. *ACS Appl. Mater. Interfaces* **2016,** *8* (30), 19579.

(168) Raja, S. N.; Bekenstein, Y.; Koc, M. A.; Fischer, S.; Zhang, D.; Lin, L.; Ritchie, R. O.; Yang, P.; Alivisatos, A. P. Encapsulation of Perovskite Nanocrystals into Macroscale Polymer Matrices: Enhanced Stability and Polarization. *ACS Appl. Mater. Interfaces* **2016,** *8* (51), 35523.

(169) Wu, H.; Wang, S.; Cao, F.; Zhou, J.; Wu, Q.; Wang, H.; Li, X.; Yin, L.; Yang, X. Ultrastable Inorganic Perovskite Nanocrystals Coated with a Thick Long-Chain Polymer for Efficient White Light-Emitting Diodes. *Chem. Mater.* **2019,** *31* (6), 1936.

(170) Wei, S.; Zhu, H.; Zhang, J.; Wang, L.; An, M.; Wang, Y.; Zhang, X.; Liu, Y. Luminescent Perovskite Nanocrystal-Epoxy Resin Composite with High Stability Against Water and Air. *J. Alloys Compd.* **2019,** *789*, 209.

(171) Tong, J.; Wu, J.; Shen, W.; Zhang, Y.; Liu, Y.; Zhang, T.; Nie, S.; Deng, Z. Direct Hot-Injection Synthesis of Lead Halide Perovskite Nanocubes in Acrylic Monomers for Ultrastable and Bright Nanocrystal–Polymer Composite Films. *ACS Appl. Mater. Interfaces* **2019,** *11* (9), 9317.

(172) Wang, H.-C.; Lin, S.-Y.; Tang, A.-C.; Singh, B. P.; Tong, H.-C.; Chen, C.-Y.; Lee, Y.-C.; Tsai, T.-L.; Liu, R.-S. Mesoporous Silica Particles Integrated with All-Inorganic $CsPbBr_3$ Perovskite Quantum-Dot Nanocomposites (MP-PQDs) with High Stability and Wide Color Gamut Used for Backlight Display. *Angew. Chem. Int. Ed.* **2016,** *55* (28), 7924.

(173) Chen, D.; Fang, G.; Chen, X. Silica-Coated Mn-Doped $CsPb(Cl/Br)_3$ Inorganic Perovskite Quantum Dots: Exciton-to-Mn Energy Transfer and Blue-Excitable Solid-State Lighting. *ACS Appl. Mater. Interfaces* **2017,** *9* (46), 40477.

(174) Li, Z.; Kong, L.; Huang, S.; Li, L. Highly Luminescent and Ultrastable $CsPbBr_3$ Perovskite Quantum Dots Incorporated into a Silica/Alumina Monolith. *Angew. Chem.* **2017,** *129* (28), 8246.

(175) Pramanik, A.; Gates, K.; Patibandla, S.; Davis, D.; Begum, S.; Iftekhar, R.; Alamgir, S.; Paige, S.; Porter, M. M.; Ray, P. C. Water-Soluble and Bright Luminescent Cesium–Lead–Bromide Perovskite Quantum Dot–Polymer Composites for Tumor-Derived Exosome Imaging. *ACS Applied Bio Materials* **2019,** *2* (12), 5872.

(176) Lu, Z.; Li, Y.; Qiu, W.; Rogach, A. L.; Nagl, S. Composite Films of $CsPbBr_3$ Perovskite Nanocrystals in a Hydrophobic Fluoropolymer for Temperature Imaging in Digital Microfluidics. *ACS Appl. Mater. Interfaces* **2020,** *12* (17), 19805.

(177) Ahmed, T.; Seth, S.; Samanta, A. Boosting the Photoluminescence of $CsPbX_3$ (X = Cl, Br, I) Perovskite Nanocrystals Covering a Wide Wavelength Range by Postsynthetic Treatment with Tetrafluoroborate Salts. *Chem. Mater.* **2018,** *30* (11), 3633.

(178) Zhang, Q.; Li, Z.; Liu, M.; Kong, L.; Zheng, W.; Wang, B.; Li, L. Bifunctional Passivation Strategy to Achieve Stable $CsPbBr_3$ Nanocrystals with Drastically Reduced Thermal-Quenching. *J. Phys. Chem. Lett.* **2020,** *11* (3), 993.

(179) Sun, H.; Yang, Z.; Wei, M.; Sun, W.; Li, X.; Ye, S.; Zhao, Y.; Tan, H.; Kynaston, E. L.; Schon, T. B.et al. Chemically Addressable Perovskite Nanocrystals for Light-Emitting Applications. *Adv. Mater.* **2017,** *29* (34), 1701153.

(180) Kim, H.; So, S.; Ribbe, A.; Liu, Y.; Hu, W.; Duzhko, V. V.; Hayward, R. C.; Emrick, T. Functional Polymers for Growth and Stabilization of $CsPbBr_3$ Perovskite Nanoparticles. *Chem. Commun.* **2019,** *55* (12), 1833.

(181) Suh, Y.-H.; Kim, T.; Choi, J. W.; Lee, C.-L.; Park, J. High-Performance $CsPbX_3$ Perovskite Quantum-Dot Light-Emitting Devices *via* Solid-State Ligand Exchange. *ACS Appl. Nano Mater.* **2018,** *1* (2), 488.

(182) He, Y.; Yoon, Y. J.; Harn, Y. W.; Biesold-McGee, G. V.; Liang, S.; Lin, C. H.; Tsukruk, V. V.; Thadhani, N.; Kang, Z.; Lin, Z. Unconventional Route to Dual-Shelled Organolead Halide Perovskite Nanocrystals with Controlled Dimensions, Surface Chemistry, and Stabilities. *Sci. Adv.* **2019,** *5* (11), eaax4424.

(183) Hou, S.; Guo, Y.; Tang, Y.; Quan, Q. Synthesis and Stabilization of Colloidal Perovskite Nanocrystals by Multidentate Polymer Micelles. *ACS Appl. Mater. Interfaces* **2017,** *9* (22), 18417.

(184) Hui, L. S.; Beswick, C.; Getachew, A.; Heilbrunner, H.; Liang, K.; Hanta, G.; Arbi, R.; Munir, M.; Dawood, H.; Isik Goktas, N.et al. Reverse Micelle Templating Route to Ordered Monodispersed Spherical Organo-Lead Halide Perovskite Nanoparticles for Light Emission. *ACS Appl. Nano Mater.* **2019,** *2* (7), 4121.

(185) Liu, Y.; Wang, Z.; Liang, S.; Li, Z.; Zhang, M.; Li, H.; Lin, Z. Polar Organic Solvent-Tolerant Perovskite Nanocrystals Permanently Ligated with Polymer Hairs *via* Star-Like Molecular Bottlebrush Trilobe Nanoreactors. *Nano Lett.* **2019,** *19* (12), 9019.

(186) Xin, Y.; Shen, W.; Deng, Z.; Zhang, J. Highly Emissive and Color-Tunable Perovskite Cross-Linkers for Luminescent Polymer Networks. *ACS Appl. Mater. Interfaces* **2018,** *10* (34), 28971.

(187) Jancik Prochazkova, A.; Demchyshyn, S.; Yumusak, C.; Másilko, J.; Brüggemann, O.; Weiter, M.; Kaltenbrunner, M.; Sariciftci, N. S.; Krajcovic, J.; Salinas, Y.et al.

Proteinogenic Amino Acid Assisted Preparation of Highly Luminescent Hybrid Perovskite Nanoparticles. *ACS Appl. Nano Mater.* **2019,** *2* (7), 4267.

(188) Pan, A.; Wang, J.; Jurow, M. J.; Jia, M.; Liu, Y.; Wu, Y.; Zhang, Y.; He, L.; Liu, Y. General Strategy for the Preparation of Stable Luminous Nanocomposite Inks Using Chemically Addressable $CsPbX_3$ Peroskite Nanocrystals. *Chem. Mater.* **2018,** *30* (8), 2771.

(189) Liang, P.; Zhang, P.; Pan, A.; Yan, K.; Zhu, Y.; Yang, M.; He, L. Unusual Stability and Temperature-Dependent Properties of Highly Emissive $CsPbBr_3$ Perovskite Nanocrystals Obtained from *in situ* Crystallization in Poly(vinylidene difluoride). *ACS Appl. Mater. Interfaces* **2019,** *11* (25), 22786.

(190) De Roo, J.; Ibáñez, M.; Geiregat, P.; Nedelcu, G.; Walravens, W.; Maes, J.; Martins, J. C.; Van Driessche, I.; Kovalenko, M. V.; Hens, Z. Highly Dynamic Ligand Binding and Light Absorption Coefficient of Cesium Lead Bromide Perovskite Nanocrystals. *ACS Nano* **2016,** *10* (2), 2071.

(191) Çetinkaya, O.; Demirci, G.; Mergo, P. Effect of the different chain transfer agents on molecular weight and optical properties of poly(methyl methacrylate). *Opt. Mater.* **2017,** *70*, 25.

(192) Liu, F.; Zhang, Y.; Ding, C.; Kobayashi, S.; Izuishi, T.; Nakazawa, N.; Toyoda, T.; Ohta, T.; Hayase, S.; Minemoto, T.et al. Highly Luminescent Phase-Stable $CsPbI_3$ Perovskite Quantum Dots Achieving Near 100% Absolute Photoluminescence Quantum Yield. *ACS Nano* **2017,** *11* (10), 10373.

(193) Wu, L.; Zhong, Q.; Yang, D.; Chen, M.; Hu, H.; Pan, Q.; Liu, H.; Cao, M.; Xu, Y.; Sun, B.et al. Improving the Stability and Size Tunability of Cesium Lead Halide Perovskite

Nanocrystals Using Trioctylphosphine Oxide as the Capping Ligand. *Langmuir* **2017,** *33* (44), 12689.

(194) Tan, Y.; Zou, Y.; Wu, L.; Huang, Q.; Yang, D.; Chen, M.; Ban, M.; Wu, C.; Wu, T.; Bai, S.et al. Highly Luminescent and Stable Perovskite Nanocrystals with Octylphosphonic Acid as a Ligand for Efficient Light-Emitting Diodes. *ACS Appl. Mater. Interfaces* **2018,** *10* (4), 3784.

(195) Zhang, B.; Goldoni, L.; Zito, J.; Dang, Z.; Almeida, G.; Zaccaria, F.; de Wit, J.; Infante, I.; De Trizio, L.; Manna, L. Alkyl Phosphonic Acids Deliver $CsPbBr_3$ Nanocrystals with High Photoluminescence Quantum Yield and Truncated Octahedron Shape. *Chem. Mater.* **2019,** *31* (21), 9140.

(196) Wu, J.; Tong, J.; Gao, Y.; Wang, A.; Zhang, T.; Tan, H.; Nie, S.; Deng, Z. Efficient and Stable Thin-Film Luminescent Solar Concentrators Enabled by Near-Infrared Emission Perovskite Nanocrystals. *Angew. Chem. Int. Ed.* **2020,** *59* (20), 7738.

(197) Krieg, F.; Ong, Q. K.; Burian, M.; Rainò, G.; Naumenko, D.; Amenitsch, H.; Süess, A.; Grotevent, M. J.; Krumeich, F.; Bodnarchuk, M. I.et al. Stable Ultraconcentrated and Ultradilute Colloids of $CsPbX_3$ (X = Cl, Br) Nanocrystals Using Natural Lecithin as a Capping Ligand. *J. Am. Chem. Soc.* **2019,** *141* (50), 19839.

(198) Krieg, F.; Ochsenbein, S. T.; Yakunin, S.; ten Brinck, S.; Aellen, P.; Süess, A.; Clerc, B.; Guggisberg, D.; Nazarenko, O.; Shynkarenko, Y.et al. Colloidal $CsPbX_3$ (X = Cl, Br, I) Nanocrystals 2.0: Zwitterionic Capping Ligands for Improved Durability and Stability. *ACS Energy Lett.* **2018,** *3* (3), 641.

(199) Chen, Q.; Yuan, L.; Duan, R.; Huang, P.; Fu, J.; Ma, H.; Wang, X.; Zhou, Y.; Song, B. Zwitterionic Polymer: A Facile Interfacial Material Works at Both Anode and Cathode in p-i-n Perovskite Solar Cells. *Solar RRL* **2019,** *3* (9), 1900118.

(200) Zhou, S.; Zhu, T.; Zheng, L.; Zhang, D.; Xu, W.; Liu, L.; Cheng, G.; Zheng, J.; Gong, X. A Zwitterionic Polymer as an Interfacial Layer for Efficient and Stable Perovskite Solar Cells. *RSC Adv.* **2019,** *9* (52), 30317.

(201) Kim, H.; Hight-Huf, N.; Kang, J.-H.; Bisnoff, P.; Sundararajan, S.; Thompson, T.; Barnes, M.; Hayward, R. C.; Emrick, T. Polymer Zwitterions for Stabilization of $CsPbBr_3$ Perovskite Nanoparticles and Nanocomposite Films. *Angew. Chem. Int. Ed.* **2020,** *59* (27), 10802.

(202) Wang, S.; Du, L.; Jin, Z.; Xin, Y.; Mattoussi, H. Enhanced Stabilization and Easy Phase Transfer of $CsPbBr_3$ Perovskite Quantum Dots Promoted by High Affinity Polyzwitterionic Ligands. *J. Am. Chem. Soc.* **2020,** *142* (29), 12669.

(203) Cabanetos, C.; El Labban, A.; Bartelt, J. A.; Douglas, J. D.; Mateker, W. R.; Fréchet, J. M. J.; McGehee, M. D.; Beaujuge, P. M. Linear Side Chains in Benzo[1,2-b:4,5-b′]dithiophene–Thieno[3,4-c]pyrrole-4,6-dione Polymers Direct Self-Assembly and Solar Cell Performance. *J. Am. Chem. Soc.* **2013,** *135* (12), 4656.

(204) Gadisa, A.; Oosterbaan, W. D.; Vandewal, K.; Bolsée, J.-C.; Bertho, S.; D'Haen, J.; Lutsen, L.; Vanderzande, D.; Manca, J. V. Effect of Alkyl Side-Chain Length on Photovoltaic Properties of Poly(3-alkylthiophene)/PCBM Bulk Heterojunctions. *Adv. Funct. Mater.* **2009,** *19* (20), 3300.

(205) Xie, R.; Chen, Z.; Zhong, W.; Zhang, G.; Huang, Y.; Ying, L.; Huang, F.; Cao, Y. Synthesis and characterization of π-conjugated copolymers based on alkyltriazolyl substituted benzodithiophene. *New J. Chem.* **2016,** *40* (5), 4727.

(206) Meager, I.; Ashraf, R. S.; Mollinger, S.; Schroeder, B. C.; Bronstein, H.; Beatrup, D.; Vezie, M. S.; Kirchartz, T.; Salleo, A.; Nelson, J.et al. Photocurrent Enhancement from Diketopyrrolopyrrole Polymer Solar Cells through Alkyl-Chain Branching Point Manipulation. *J. Am. Chem. Soc.* **2013,** *135* (31), 11537.

(207) Shivhare, R.; Erdmann, T.; Hörmann, U.; Collado-Fregoso, E.; Zeiske, S.; Benduhn, J.; Ullbrich, S.; Hübner, R.; Hambsch, M.; Kiriy, A.et al. Alkyl Branching Position in Diketopyrrolopyrrole Polymers: Interplay between Fibrillar Morphology and Crystallinity and Their Effect on Photogeneration and Recombination in Bulk-Heterojunction Solar Cells. *Chem. Mater.* **2018,** *30* (19), 6801.

(208) Lei, T.; Dou, J.-H.; Pei, J. Influence of Alkyl Chain Branching Positions on the Hole Mobilities of Polymer Thin-Film Transistors. *Adv. Mater.* **2012,** *24* (48), 6457.

(209) Groh, W. Overtone Absorption in Macromolecules for Polymer Optical Fibers. *Die Makromol. Chemie* **1988,** *189* (12), 2861.

(210) Prat, D.; Wells, A.; Hayler, J.; Sneddon, H.; McElroy, C. R.; Abou-Shehada, S.; Dunn, P. J. CHEM21 Selection Guide of Classical- and Less Classical-Solvents. *Green. Chem.* **2015,** *18* (1), 288.

(211) Obrezkova, M. A.; Kalinina, A. A.; Pavlichenko, I. V.; Vasilenko, N. G.; Mironova, M. V.; Semakov, A. V.; Kulichikhin, V. G.; Buzin, M. I.; Muzafarov, A. M. Comb-Like Polymethylsiloxanes. Synthesis, Structure and Properties. *Silicon* **2015,** *7* (2), 177.

(212) Knauf, R. R.; Lennox, J. C.; Dempsey, J. L. Quantifying Ligand Exchange Reactions at CdSe Nanocrystal Surfaces. *Chem. Mater.* **2016,** *28* (13), 4762.

(213) Dierick, R.; Van den Broeck, F.; De Nolf, K.; Zhao, Q.; Vantomme, A.; Martins, J. C.; Hens, Z. Surface Chemistry of $CuInS_2$ Colloidal Nanocrystals, Tight Binding of L-Type Ligands. *Chem. Mater.* **2014,** *26* (20), 5950.

(214) Hens, Z.; Martins, J. C. A Solution NMR Toolbox for Characterizing the Surface Chemistry of Colloidal Nanocrystals. *Chem. Mater.* **2013,** *25* (8), 1211.

(215) Imran, M.; Ijaz, P.; Goldoni, L.; Maggioni, D.; Petralanda, U.; Prato, M.; Almeida, G.; Infante, I.; Manna, L. Simultaneous Cationic and Anionic Ligand Exchange For Colloidally Stable CsPbBr3 Nanocrystals. *ACS Energy Lett.* **2019,** *4* (4), 819.

(216) Quarta, D.; Imran, M.; Capodilupo, A.-L.; Petralanda, U.; van Beek, B.; De Angelis, F.; Manna, L.; Infante, I.; De Trizio, L.; Giansante, C. Stable Ligand Coordination at the Surface of Colloidal $CsPbBr_3$ Nanocrystals. *J. Phys. Chem. Lett.* **2019,** *10* (13), 3715.

(217) Shimizu, K. T.; Böhmer, M.; Estrada, D.; Gangwal, S.; Grabowski, S.; Bechtel, H.; Kang, E.; Vampola, K. J.; Chamberlin, D.; Shchekin, O. B.et al. Toward Commercial Realization of Quantum Dot Based White Light-Emitting Diodes for General Illumination. *Photonics Research* **2017,** *5* (2), A1.

(218) Sorensen, C. M. Light Scattering by Fractal Aggregates: A Review. *Aerosol Sci. Technol.* **2001,** *35* (2), 648.

(219) Rainò, G.; Landuyt, A.; Krieg, F.; Bernasconi, C.; Ochsenbein, S. T.; Dirin, D. N.; Bodnarchuk, M. I.; Kovalenko, M. V. Underestimated Effect of a Polymer Matrix on the Light Emission of Single $CsPbBr_3$ Nanocrystals. *Nano Lett.* **2019,** *19* (6), 3648.

(220) Di Stasio, F.; Christodoulou, S.; Huo, N.; Konstantatos, G. Near-Unity Photoluminescence Quantum Yield in $CsPbBr_3$ Nanocrystal Solid-State Films *via* Postsynthesis Treatment with Lead Bromide. *Chem. Mater.* **2017,** *29* (18), 7663.

(221) Huang, Y.; Cohen, T. A.; Sperry, B. M.; Larson, H.; Nguyen, H. A.; Homer, M. K.; Dou, F. Y.; Jacoby, L. M.; Cossairt, B. M.; Gamelin, D. R.et al. Organic building blocks at inorganic nanomaterial interfaces. *Mater. Horiz.* **2022,** *9* (1), 61.

(222) Yang, S.-H. Spintronics on chiral objects. *Appl. Phys. Lett.* **2020,** *116* (12), 120502.

(223) Kim, Y.-H.; Zhai, Y.; Lu, H.; Pan, X.; Xiao, C.; Gaulding, E. A.; Harvey, S. P.; Berry, J. J.; Vardeny, Z. V.; Luther, J. M.et al. Chiral-induced spin selectivity enables a room-temperature spin light-emitting diode. *Science* **2021,** *371* (6534), 1129.

(224) Naaman, R.; Paltiel, Y.; Waldeck, D. H. Chiral molecules and the electron spin. *Nature Reviews Chemistry* **2019,** *3* (4), 250.